Characterisation of Elastic Behaviours of Sandstone Reservoirs for the Aramis CCS Project in the North Sea

Stress history and reservoir pressure project for CO_2 storage (SHARP storage project)
MSc Thesis

Lujain Ali Alghannam 5258898
Thesis Committee:
Auke Barnhoorn (Thesis Supervisor - TU Delft)
Kees Weemstra (TU Delft)
Guillaume Rongier (TU Delft)

Department of Civil Engineering and Geosciences
TUDelft

Thursday 31st August, 2023

Contents

Abstract

Depleted-gas sandstone reservoirs in the Dutch North Sea are being evaluated for offshore carbon storage under the ARAMIS project. The variability in geomechanical properties urges an investigation of the elastic parameters. This study involved cored samples and logs from five Slochteren and Solling formations wells. It aims to characterize seventeen cored samples' static and dynamic elastic behaviour experimentally via triaxial compression tests with active acoustics. Substantial variability was shown in wave velocities, moduli, Poisson and velocity ratios highly correlated to porosity, density and confining pressure variations. Therefore, empirical correlations were established between elastic moduli, confining pressure and porosity from the lab measurements. Another empirical correlation was established between the dynamic and the static Young's modulus with a high correlation coefficient of 0.8. To enable elastic moduli log predictions with the absence of S-wave velocity log measurements, a workflow was developed to predict S-wave velocities using empirical correlations from lab measurements, nearby wells, and literature to evaluate the estimation quality. Comparisons between measured and predicted dynamic moduli showed agreement, validating the physics of the different datasets. However, it is important to mention that discrepancies existed for parameters like Poisson Ratio, indicating that factors like porosity affect predictions. Although there is limited data from logs and experiments, this study provides important geomechanical insights and predictive capabilities for this initial stage of geomechanical reservoir characterization for the ARAMIS CCS project.

Acknowledgements

I would like to express my deepest gratitude to my thesis advisor, Auke Barnhoorn, for his invaluable guidance and support throughout this research project. I am also thankful to my committee members, Guillaume Rongier and Kees Weemstra, for their feedback and insights.
I am incredibly grateful to my dear friend Barbara, whose endless encouragement and assistance enabled me to gain knowledge and perspective that greatly benefited this thesis. Sincere thanks to Dr. Debanjan Chandra for his constant involvement and expert input at various stages of this work.
I am forever thankful to my loved ones for their unwavering emotional support, patience and practical help during this thesis journey. I sincerely appreciate SHELL's core lab for providing the critical core samples and preparing them for our experiments. I am also thankful to the nicest and most cooperative lab technicians, Marc and Jens, who facilitated the experimental work. This research would not have been possible without everyone's contributions.

1 Introduction

1.1 Carbon Capture and Storage for Climate Change Mitigation

The world's population is exponentially growing, and as a consequence, the amount of energy and resources consumed has exponentially increased as well during the last century. A significant byproduct of population growth is the increase in development, hence an increase in environmental risks, specifically climate change. Despite the fact that climate change has multiple causes, one of the leading agents for climate change is the increment in CO2 emissions due to the utilization of fossil fuels. For example, in the energy and industrial sector in 2020, 93% of the total CO2 emissions came from fossil fuels (Ritchie & Roser, 2020). To avoid catastrophic events for humanity due to climate change, it is essential to reduce CO2 emissions and diversify the world's energy matrix, including greener energy sources.
To reduce CO2 emissions, the world is transitioning from fossil fuels to green energies, and one way to expedite the process and meet the Paris Agreement is to capture the CO2 emitted from fossil fuels or industrial areas and store it in the subsurface. Multiple carbon capture and storage projects are maturing in Europe and around the world. Carbon capture and storage (CCS) technologies aim to reduce greenhouse gas emissions from fixed sources like industrial sites and power facilities. A Key global climate report from the IPCC Fifth Assessment states that CCS could contribute 13-14% of the total emissions cut needed by 2100 to restrict global warming to 2°C (IPCC, 2014). The CCS process entails trapping the CO2 from its sources; transporting it via pipes if the storage is onshore or via marine vessels if the storage location is offshore, and then pumping it deep underground for secure long-term storage. Trapping the CO2 in the geological formations includes depleted oil and gas reservoirs, deep saline aquifers, and unmineable coal seams (Global CCS Institute, 2019). Implementing such large-scale projects requires a substantial infrastructure in terms of building and cost; however, these are expected to decrease as the technology matures. Even though the intention of the CCS projects is noble for a better, cleaner earth, it faces public acceptance challenges due to perceived risks such as gas leakage. It is understandable that the public fears such geomechanical risks that are associated with the CO2 underground injection, and it requires a thorough assessment that institutions and the industry are implementing.

1.2 Geomechanical Characterization

Proper geomechanical site characterization and modelling are essential prior to and during CO2 injection to assess potential risks and ensure safe, efficient storage (Zoback, 2007). Key risks that must be mitigated through geomechanical analysis include caprock fracturing, CO2 leakage, fault activation, induced seismicity, and well injectivity issues, which are essential for reservoir geomechanics assessment. The analysis are done for maintaining caprock integrity as it acts as the barrier preventing CO2 from escaping the reservoir. Also, identifying susceptible faults and mitigating leakage as the analysis evaluates if the faults are critically stressed and determine the safe limits to prevent slips due to pressure changes during the injection. Additionally, to optimize the injectivity, characterizing the fractures, the rock properties from porosity and permeability, for example, play a big role in selecting the ideal storage zones. Overall, analyses are important to establish a safe operating threshold for pressure and injection rate limits to optimally avoid induced seismicity, fault slip, fracturing of the caprock and associated containment issues (Verdon et al., 2013). Each of these risks requires various geomechanical and petrophysical parameters to be characterised to assess the CO2 storage site. Inputs include minimum horizontal stress when combined with pore pressure determines the likelihood of tensile fracturing (Morris et al., 2011). Porosity and permeability are important to understand the impact of fluid pressure communication for caprock analysis, while they are also important to understand the injectivity capacity (Rutqvist et al., 2010). Elastic moduli are important to understand the impacts of fracture opening/closure for injectivity analysis where, for example, higher Young's modulus values indicate fracture opening resistance. Monitoring elastic moduli can be very helpful for the induced seismicity risk as well, where, for example, lower moduli can dampen and attenuate seismic energy, reducing the vibration at the surface that could indicate deformations (low values of Young's and shear modulus) (Zoback & Gorelick, 2012).
By characterizing the key parameters through geomechanical analysis and modelling, the major risks associated with CO2 injection can be evaluated, mitigated and evaluated to ensure safe practices.

1.3 Research Topic: SHARP/ARAMIS CCS Project

The Dutch offshore sector is considered a prospective area for CCS to reduce the Dutch carbon footprint. A significant number of depleted gas fields and potential aquifers are identified as prospective areas covering multiple geological intervals.

Zooming into the Dutch ARAMIS project, it is a consortium between multiple companies like Shell, EBN, and TNO to enable large-scale offshore CO2 storage for Dutch emissions sources. ARAMIS aims to develop an integrated CCS chain for transporting CO2 from Rotterdam to offshore depleted gas reservoirs. ARAMIS project falls within SHARP Project's objectives, especially the storage site assessment. SHARP project has multiple work packages and WP3 work package focuses specifically on rock mechanics, well integrity and ensuring caprock stability during CO2 injection. WP3 studies will focus on the characterization of reservoir and caprock's geomechanical properties and behaviours via lab testing of cores and modelling in relation to the stress history and operational stress changes and analyze its sensetivities to a selection of observable attributes for monitoring (Skurtveit et al. 2022). Translating the direct quantification of the experiments of the deformation behaviour to field scale in situ conditions is an essential objective of this package to properly feed into geomechanical models simulating reservoir compaction, stress changes, and caprock integrity impacts from CO2 injection which is essential for monitoring campaigns (Skurtveit et al. 2022).
SHARP project includes collaborations with TU Delft to leverage academic expertise in making CCS deployment a reality. TU Delft is contributing to this project in multiple phases. The relevant collaboration to the thesis is the TU Delft collaboration with Shell on the experimental characterization of rock mechanical behaviour, non-linear constitutive models of reservoir, with a focus on lithologies from the depleted reservoirs included in the ARAMIS project (SHARP Storage, 2022).

1.3.1 Research Scope

A crucial aspect of ARAMIS project is the selection of appropriate storage sites. Geological formations exhibit wide variations in their physical and mechanical properties, which subsequently impact their carbon storage capacity. Sandstone reservoirs have been identified as suitable candidates due to their high porosity and permeability, making them an area of keen interest in carbon storage studies. The scope of this research is centred on two geological groups in the Dutch North Sea: Upper Rotliegend and Upper German Groups, specifically the sandstone reservoirs of the Slochteren Formation and the middle Solling Formation, where the Slochteren Formation is Europe's largest gas field and a potential hub for carbon storage. This investigation into its geomechanical attributes is part of the broader ARAMIS Project, an extensive initiative exploring potential carbon storage locations within the North Sea region.
The investigation aims to utilize core samples and log data to characterize the geomechanical properties of different North Sea storage sites identified by the ARAMIS project by performing lab experiments and log analyses.

1.3.2 Study Objective

Here are key points of the objective of this thesis:

1. It focuses specifically on the elastic properties characterized by lab testing, as this is the main data that are acquired, which include these key objectives:
    - Build database of the Dutch NorthSea mechanics
    - Quantify mechanical properties of the reservoir rock
    - Assess the effect of e.g. porosity, and depositional environment on mechanical & acoustic properties.
    - Quantify acoustic properties variation with varying reservoir rock stress conditions and varying rock parameters.
2. By examining the variability among logged wells, it becomes possible to compare various samples that cover different aspects of the rock properties of the reservoir. This includes factors such as porosity, clay content, and depositional environment.
3. It presents results for geomechanical modelling and carbon storage suitability, which connects to the wider applied purpose.

From the objective above, we can summarize its focus in these thesis questions where this thesis will be focusing on answering:

1.3.3 Thesis Questions

"How can the variability in rock properties affect the elastic behaviour in a reservoir? And how can acoustic attributes be used to predict the elastic behaviour of a reservoir?"

1.4 Thesis Workflow

To fulfil the questions, an experimental workflow is designed to quantify key elastic properties like Young's modulus and Poisson's ratio for each sample. The analysis will then compare these properties between samples from different wells to identify and discuss any variability or trends. Relating this to well-log data and interpreting the implications for geomechanical models will help address the second part of the question. Here is the workflow that was established and followed in this thesis:

1. Organize and select the samples received for the study to cover a various range of rock parameters like porosity and lithology.
2. Assess the elastic behaviour of the sandstone samples from the different reservoirs in the North Sea using Triaxial Compression tests with active acoustics measurements. Which includes:
    - Quantifying the mechanical & acoustic properties of the reservoir rocks.
    - Assessing the effect of e.g. porosity, density, and depositional environment on mechanical & acoustic properties.
    - Quantifying of variation of acoustic properties with varying stress conditions of the reservoir rock.
    - Correlate static to dynamic elastic parameters in the experiment.
3. Asses log data and analyze the variability of the rock parameters in the logged wells asses their correlation to the cored samples measured rock parameters.
4. Evaluate the correlation between the dynamic elastic parameters from the experiment to the logs.
5. Compare the data obtained to a larger scale data to evaluate their representation of the geomechanical parameters of the target reservoirs.

2 Geological Setting

To make a structured and comprehensible reading, firstly, a broad introduction to the North Sea's geological history is given to understand the tectonics and stratigraphy involved in the formation of the present subsurface. To follow, different subsections are focused on the North Sea and the target reservoirs of each location.

2.1 North Sea Geological Background

The North Sea is located between the United Kingdom and Scandinavia, covering over 750,000 km2. Geographically, it stretches from Norway south to the Netherlands, east to Germany and Denmark, and west to the United Kingdom (Glennie & Underhill, 2009).
The North Sea has undergone a complex geological history shaped by multiple tectonic events that structured and buried key stratigraphic intervals like the Upper Germanic Trias and Rotliegend groups.
In general, the structural evolution of the North Sea began in the Permian with continental rifting and crustal extension associated with the breakup of Pangaea and the opening of the Neo-Tethys Ocean (Ziegler, 1992). This produced a series of grabens and half-grabens, including the Central Graben where the Dutch offshore sector is located. Extension and rifting continued into the Triassic along with major intrusions of volcanics. The resulting accommodation space allowed the deposition of thick Triassic-Jurassic sequences like the Upper Germanic Trias Group across the Central Graben (Færseth, 1996).
The Permian Rotliegend Group sandstones were deposited after the main rifting phase when the North Sea was largely an inland desert basin. During the Permo-Triassic time, given the position of this region in the Equator and the warm climate, it promoted thick aeolian and fluvial sandstone formation interbedded with evaporites (Geluk 2007). Due to that, the group forms important gas reservoirs hosted in fault blocks and tilted horst structures.
The Upper Germanic Trias Group consists of sandstones, shales and evaporites deposited in fluvial, lacustrine and desert environments. Thick salt layers like the Zechstein Group were deposited as the North Sea area became restricted during the Triassic (Geluk, 2007). Structurally, continued crustal stretching formed major fault blocks that controlled sediment dispersal patterns and thicknesses.
After a period of tectonic quiescence in the Early Cretaceous, inversion tectonics commenced in the Late Cretaceous due to the Alpine Orogeny far to the south (Nielsen et al., 2005). This compressional event caused the reactivation of many existing faults and folds in the North Sea grabens, modifying trap geometries. Significant uplift and erosion also occurred, removing substantial overburden. This complex history of multiple rifting and inversion events controlled the architecture of North Sea reservoirs and seals relevant to subsurface activities.

2.2 Target Formations & Study Locations Geology

After covering the general geological history of the North Sea and then diving into the target stratigraphic groups, it is time to focus on the study area within the Dutch North Sea, the wells that will be studied in this thesis project. This thesis focuses on the Aramis Project part of the multi-country SHARP project, where several Dutch depleted gas reservoirs are involved in this case study. As seen in Figure 2.1 below, the Dutch north sea is divided into several sections where only parts of sections K and L are involved in this geomechanical study. The K & L blocks are situated offshore in the Dutch sector of the Southern North Sea. Structurally, the area of interest, highlighted in the black box in Figure 2.1 (a), covers the northern margin of the Broad Fourteens Basin, the central part of the Vlieland Basin, the Off Holland Low, and the northern extremity of the Texel-IJsselmeer High.

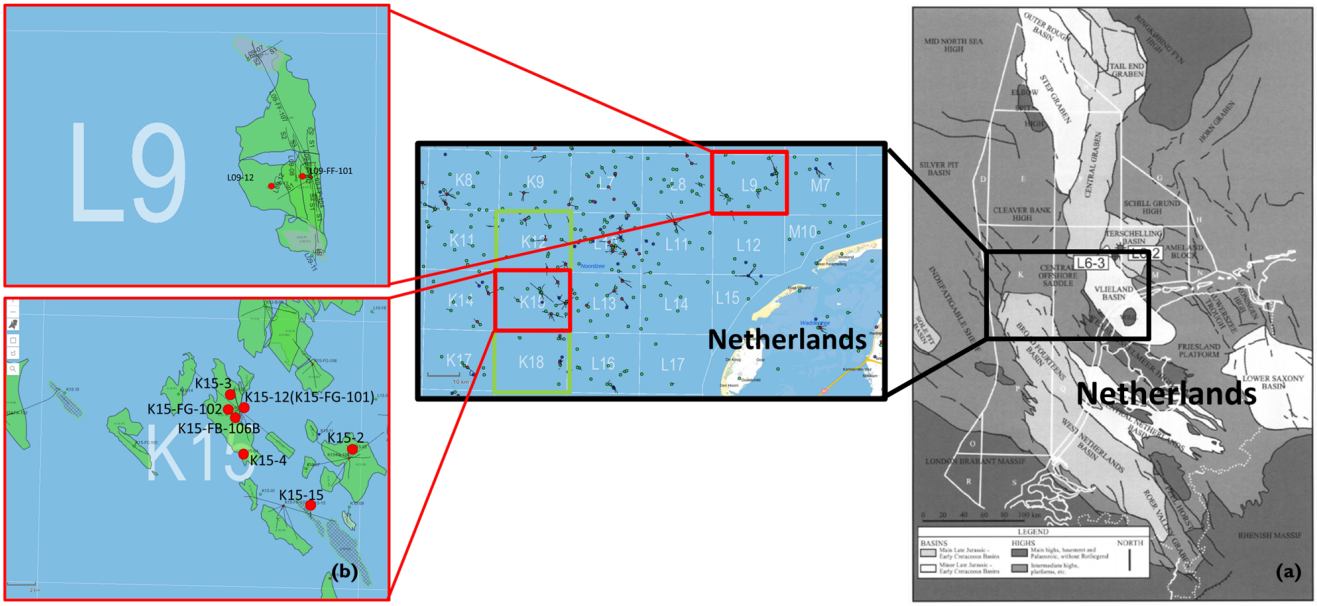

Figure 2.1: (a) Structure map of the Dutch North Sea (Abbink et al. (2001)). (b) Study location wells from sections K and L that are involved in the project (modified from nlog.nl).

An overall of 5 wells are included that are: K15-15A, K15-12, K15-FG-102, K15-2 and L09-10. These wells penetrate multiple target reservoirs; Upper and Lower Slochteren sandstone members of the Slochteren formation and the middle sandstone Solling member of the Solling formation.
The wells within the K section are focused on the Slochteren sandstone reservoirs within the Slochteren formation. The Slochteren Formation is an important gas-bearing sandstone unit within the offshore sector of the Upper Rotliegend Group of the Netherlands. The main members the study will be focused on are the lower and upper Slochteren.
The Lower and Upper Slochteren members have a wide variety of colours, grain sizes and grain sortness. They were deposited during the Permian rifting phase as the depositional environments were interpreted to be alluvial and aeolian with dune, sand flats and playa lakes under arid and semi-arid climate conditions (Gaupp & Okkerman, 2012).
The Upper Slochteren sandstone member is sealed by intra-Rotliegend Ten Boer member shales but is also by overlying Zechstein evaporites (Lauwerier, 2021). In comparison, the Lower Slochteren member is sealed by the intra-Rotliegend Silverpit formation shales, especially the Ameland member. Also sealed by the overlying Zechstein evaporites.
In the second block, the L section, the wells are targeting another reservoir within the Solling Formation. To be more specific, the focus is on the middle Solling sandstone member. The sedimentological observations indicate that most of the interval is made up of aeolian sand. The sandstone is present in a wedge-like depression near a salt dome, indicating Early Triassic salt movement (van der Kooij, 2016). The sandstone member is bounded by clay members that potentially act like seals for the sandstone.

3 Material

Samples are collected from the North Sea's three different reservoirs: the upper Slochteren, the lower Slochteren and the middle Solling sandstone. A total of 5 wells from the target area were involved in the study. Due to the absence of S-wave velocity measurements, three wells from the nearby blocks were added. From the five wells, 19 rock samples were carefully selected for this study to cover as much variability as time allows. Those samples were chosen to cover the variability in terms of the depositional environment, the facies and the porosity distribution. The main objective is to obtain as much mechanical and acoustic behavioural information as possible from all these samples. In order to achieve this, several preparations were carried out on the samples received: porosity measurements, shear testing with confining pressure (P_c), and acoustic measurements.

This section describes the steps to prepare the different datasets from the samples for the tests and then the log data for the data analysis.

3.1 Samples Data

3.1.1 Sample Selection & Preparation

The team analyzed the log data of several wells for the ARAMIS project and selected several depth intervals per well to cover as much variability as possible. Then the team visited the core lab at SHELL Amsterdam Research Center in order to select the exact locations on the cores of these wells while avoiding cracks, and other defects, as seen in Figure 3.1 below. After the selection step, the cores are drilled by SHELL Core Lab and prepared with a length-to-diameter ratio of 2-2.5, where most samples were either 50-25mm or 40-20mm length to diameter. Once the selected samples are delivered to TU Delft labs, the team ensures that the samples are cut and ground to the desired dimensions, with ends smoothed parallel. The dimensions of the samples are measured using calipers that are accurate to 0.01 mm. Additionally, to minimize the uncertainty, the diameter is measured in several spots per sample and the length is measured in all orientations. Finally, all the samples had their density measured by the helium gas pycnometer. It uses the physical process of gas displacement under pressure to accurately measure sample volume and density. The helium gas can penetrate pores better than liquid for enhanced precision. Then, the samples' porosity is calculated by entering the measured parameters into a ready-to-use Matlab code prepared by the team.

Figure 3.1: Cores from the selected wells

Prior to testing, the samples are saturated by immersing them under a vacuum in a brine solution with a concen-

tration of 80 g/L NaCl as seen in Figure 3.2 below, which allows air to escape and ensures full saturation.

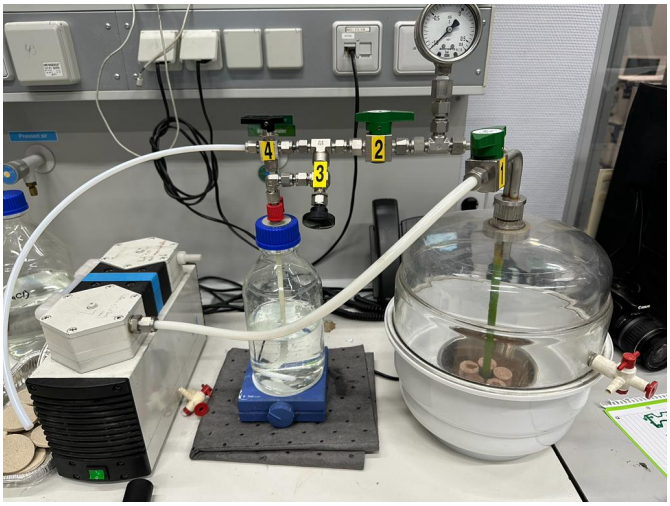

Figure 3.2: Machine used to saturate the sample with the brine solution in vacuum

3.1.2 Samples Description

This section will showcase the information gathered about the selected samples with regard to the well name and location, sample numbers, depth, porosity, bulk density, lithology description and photos of the samples.
The total number of samples that were tested is 19, where 16 of them are from the Slochteren formation (nine from the Lower Slochteren member and seven from the Upper Slochteren member), and the remaining three are from the Solling formation (the middle Solling sandstone member). The map in Figure 3.3 below displays samples from different wells from multiple reservoirs included in the ARAMIS case study. Besides the difference in lithology description between the samples, the variations in depth were also considered. The samples selected covered the ranges from 3172m down to 4236m measured depth, as seen in table 3.1 below. These differences in composition play an important role in their geomechanical behaviour since they can affect, for example, the P-wave velocity or the Young's modulus of the sample.

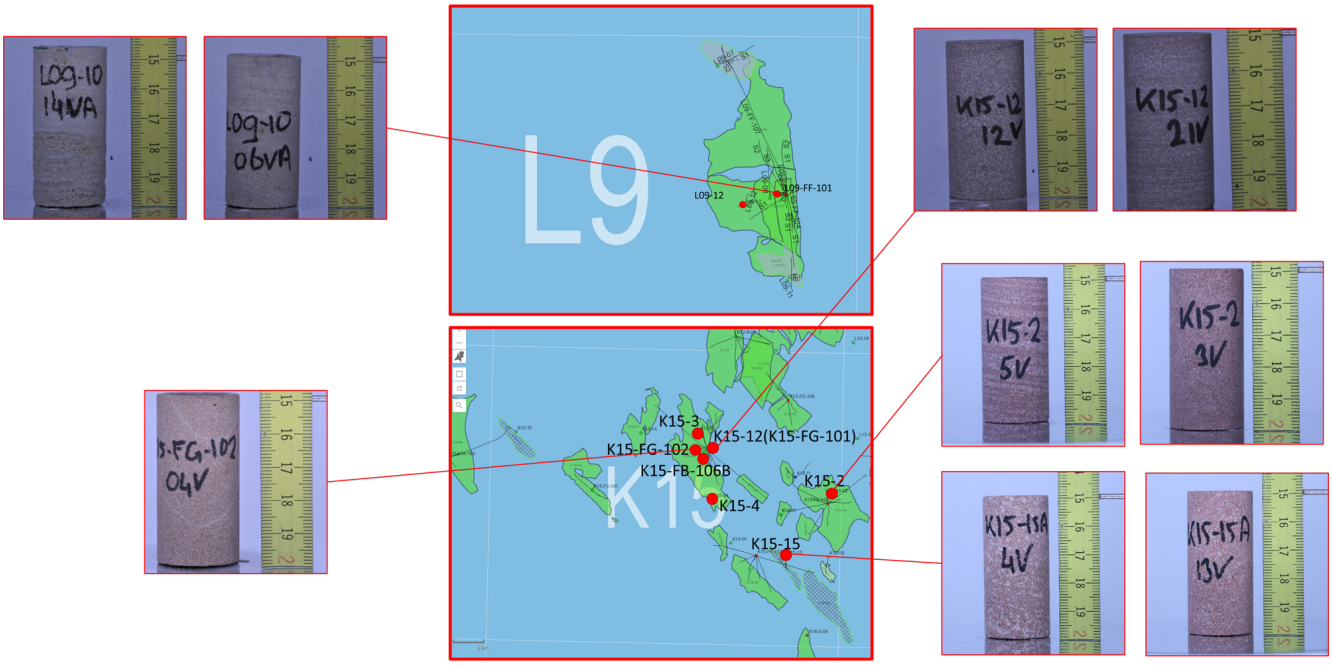

Figure 3.3: Core samples from various wells in the AOI, maps modified from nlog.nl

Table 3.1: Geological information and rock description of all samples obtained for the study

Well Name	Sample Name	Group/ Formation	Member	Lithology Description	Measured Depth [m]
K15-2	K15_2_3V	Rotliegend /Slochteren	Lower Slochteren Member	Medium grain, consolidated sandstone with no Bandings	3458.55
K15-2	K15_2_4V	Rotliegend /Slochteren	Lower Slochteren Member	Coarse grain, consolidated sandstone with no Bandings	3458.72
K15-2	K15_2_5V	Rotliegend /Slochteren	Lower Slochteren Member	Coarse grain, consolidated sandstone with Bandings	3461.45
K15-2	K15_2_7V	Rotliegend /Slochteren	Lower Slochteren Member	Medium grain, consolidated sandstone with no Bandings	3462.35
K15-2	K15-2_8V	Rotliegend /Slochteren	Lower Slochteren Member	NA	3462.6
K15-12	K15_12_1V	Rotliegend /Slochteren	Upper Slochteren Member	Medium grain, consolidated sandstone with Bandings	3930.05
K15-12	K15_12_12V	Rotliegend /Slochteren	Upper Slochteren Member	Coarse grain, consolidated sandstone with no Bandings	3945.1
K15-12	K15_12_14V	Rotliegend /Slochteren	Upper Slochteren Member	Coarse grain, consolidated sandstone with no Bandings	3946.9
K15-12	K15_12_21V	Rotliegend /Slochteren	Upper Slochteren Member	Medium grain, consolidated sandstone with Bandings	3955.8
K15-FG-102	K15-FG-102_02V	Rotliegend /Slochteren	Upper Slochteren Member	Medium grain, consolidated sandstone with no Bandings	4177.55
K15-FG-102	K15-FG-102_04V	Rotliegend / Slochteren	Upper Slochteren Member	Medium grain, consolidated sandstone with Bandings	4176.8
K15-15A	K15_15A_04V	Rotliegend /Slochteren	Lower Slochteren Member	Coarse grain, consolidated sandstone with no Bandings	4236.18
K15-15A	K15_15A_05V	Rotliegend /Slochteren	Lower Slochteren Member	Coarse grain, consolidated sandstone with no Bandings	4236.45
K15-15A	K15_15A_06V	Rotliegend /Slochteren	Lower Slochteren Member	Coarse grain, consolidated sandstone with Bandings	4236.81
K15-15A	K15_15A_13V	Rotliegend /Slochteren	Lower Slochteren Member	Coarse grain, consolidated sandstone with no Bandings	4249.3
K8-08	K8_08_16V	Rotliegend /Slochteren	Upper Slochteren Member	NA	3440.14
L09-10	L09_10_05VB	The Upper Germanic Trias / Solling	middle Solling Sandstone member	Coarse grain, non-consolidated sandstone with Bandings	3171.98
L09-10	L09_10_06VA	The Upper Germanic Trias / Solling	middle Solling Sandstone member	Coarse grain, non-consolidated sandstone with Bandings	3172.2
L09-10	L09_10_14VB	The Upper Germanic Trias / Solling	middle Solling Sandstone member	Coarse grain,very non-consolidated sandstone with Bandings	3204.35

In the selection processes, I ensured the selection of the largest range of porosities, as seen in table 3.2 below, where the porosity values range from 8% to 25%. As previously mentioned, the goal was to analyze how variability affects the elastic properties.

Table 3.2: Samples'rock parameters and dimension measurements of all samples obtained for the study

Well Name	Sample Name	Diameter [mm]	Length [mm]	Weight [g]	Density [g/cm3]-Pycnometer	Porosity - Pycnometer [%]
K15-2	K15_2_3V	25.72	51.43	63.27	2.648	10.6%
K15-2	K15_2_4V	25.74	51.42	62.952	2.655	11.3%
K15-2	K15_2_5V	25.7	51.44	63.828	2.704	11.5%
K15-2	K15_2_7V	25.72	51.54	61.534	2.6879	14.4%
K15-2	K15-2_8V	25.75	51.52	64.374	2.6932	10.9%
K15-12	K15_12_1V	25.45	50.8	64.182	2.7133	8.5%
K15-12	K15_12_12V	25.5	50.85	60.232	2.7046	14.2%
K15-12	K15_12_14V	25.52	50.72	60.834	2.7097	13.5%
K15-12	K15_12_21V	25.51	50.82	63.87	2.704	9.1%
K15-FG-102	K15-FG-102_02V	25.45	51.57	59.484	2.7094	16.2%
K15-FG-102	K15-FG-102_04V	25.47	51.5	58.567	2.7029	17.3%
K15-15A	K15_15A_04V	25.6	51.3	55.715	2.7434	23.1%
K15-15A	K15_15A_05V	25.58	51.24	56.064	2.7463	22.5%
K15-15A	K15_15A_06V	25.65	51.37	58.962	2.7418	19.0%
K15-15A	K15_15A_13V	25.6	51.35	56.115	2.7336	22.5%
K8-08	K8_08_16V	22.33	45.07	47.042	2.7408	2.7%
L09-10	L09_10_05VB	25.69	51.83	57.787	2.6662	19.3%
L09-10	L09_10_06VA	25.65	52.07	56.03	2.6596	21.7%
L09-10	L09_10_14VB	25.38	53.33	51.8340	2.6498	25%

Calculating the most representative density is important since the density measured in the Pycnometer was the grain density, so it did not consider the fluid saturating the porosity within the samples. In the case of these tests, brine was used. Therefore, to calculate the bulk density, we need to calculate the density of the fluid in order to incorporate that into the overall density of the sample. The density of the sample is represented in the simple equation below (equation 3.1). For simplification purposes, the calculation used the generic salt composition with a density of 0.001198 g/cm^3 and added that to the water that has a density of 1 g/cm^3 then used it as the density of the salt water for equation 3.1 below.

$$\rho_{\text{bulk}} = \rho_{\text{grain}} * (1 - \phi) + \rho_{\text{saltwater}} * \phi \tag{3.1}$$

3.2 Well-log Data

A total of 8 wells were involved in the analysis, 5 of them from the study area and 3 are nearby wells. Four of the five cover the Slochteren formation, and one well covers the Solling formation. The remaining three nearby wells only have the Slochteren formation, as seen in Figure 3.4.

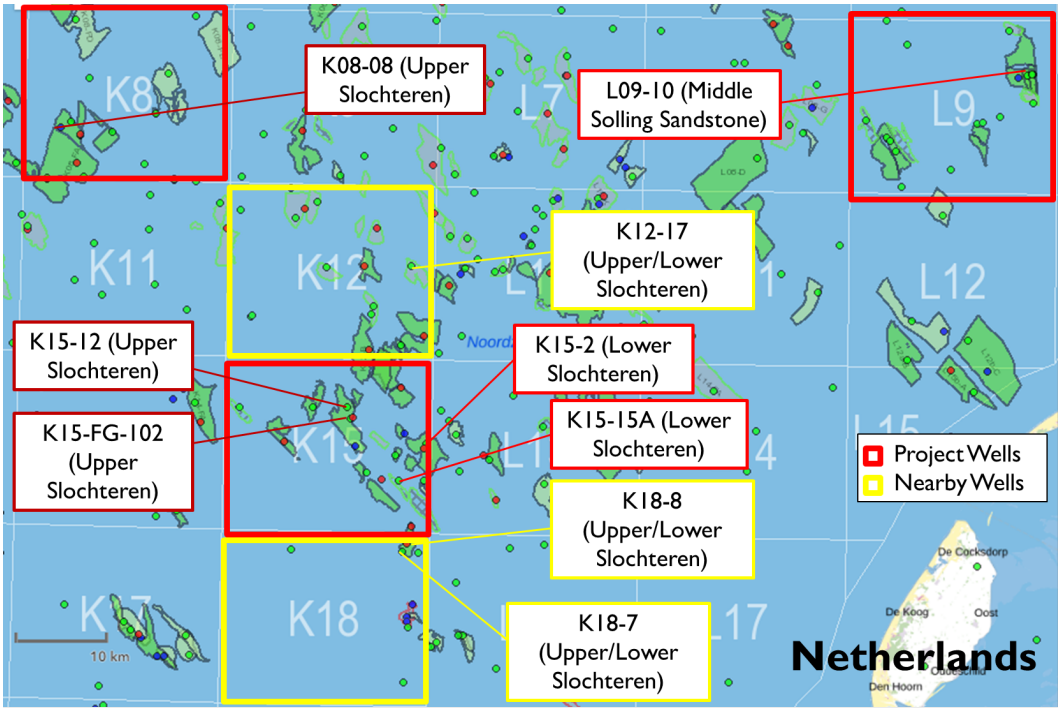

Figure 3.4: Well locations with the target formation/member, map modified from nlog.nl

For log analysis, log data have been retrieved from NLOG, and the data types are displayed in table 3.3 below.

Table 3.3: Collected log data for each well involved in the study

Well Name	Group/ Formation	Member	Gamma	Resistivity	Density	Neutron Porosity	P-Sonic	S-Sonic
K15-2	Rotliegend/ Slochteren	Lower Slochteren	Yes	Yes	Yes	Yes	Yes	No
K15-12	Rotliegend/ Slochteren	Upper Slochteren	Yes	No	Yes	Yes	Yes	No
K15-FG-102	Rotliegend/ Slochteren	Upper Slochteren	Yes	Yes	Yes	Yes	Yes	No
K15-15A	Rotliegend/ Slochteren	Lower Slochteren	Yes	Yes	Yes	Yes	Yes	No
K8-08	Rotliegend/ Slochteren	Upper Slochteren	NA	NA	NA	NA	NA	NA
L09-10	The Upper Germanic/ Solling	middle Solling Sandstone	Yes	No	Yes	Yes	Yes	No
K12-17	Rotliegend/ Slochteren	Upper/Lower Slochteren	Yes	Yes	Yes	Yes	Yes	Yes
K18-7	Rotliegend/ Slochteren	Upper/Lower Slochteren	Yes	No	No	No	Yes	Yes
K18-8	Rotliegend/ Slochteren	Upper/Lower Slochteren	Yes	No	No	No	Yes	Yes

Petrel software is used to gather, clean and view the data initially. Afterwards, I personally created Python codes for most of the data analysis in my thesis. Several logging tools were used in order to improve the accuracy of the correlation, i.e. Gamma rays (GR), Density, and Neutron Porosity, among others as seen in table 3.3.
Obtaining log data from my wells covers key petrophysical properties useful for geomechanical analysis. Gamma-

ray logs measure natural radioactivity and indicate lithology and clay content; thus, the lower the GR, the cleaner the sandstone (Asquith and Krygowski, 2004). Resistivity logs measure a formation's resistance to electric current which can be used as an indication of hydrocarbon accumulation intervals (high resistivity). P-sonic logs record the interval transit time of compressional acoustic waves where P-wave velocity can be calculated directly from its inverse. Density logs measuring bulk density (RHOB) indicate lithology and porosity. Neutron logs measure the hydrogen index and provide porosity in clean formations (Asquith and Krygowski, 2004).
Additionally, I obtained additional sonic and other logs from three nearby wells to supplement my limited log data, especially with regard to the absence of S-sonic measurements in my project wells. One of the wells provided a complete set of logs. The other nearby wells only provided gamma ray and sonic logs. Sonic logs recording shear wave velocity (S-sonic) are essential for geomechanical analysis. Having S-wave velocity measurements in addition to other logs like density and P-wave velocity relates to mechanical properties like Young's modulus, shear modulus and Poisson's ratio (Zoback, 2007), where the additional measured sonic data improves the calculations accuracy of these key parameters.

On top of the full logs that are involved in the study, a set of geomechanical data of several wells across the offshore and onshore parts of the Netherlands were included and gathered from TNO data and retrieved from NLOG to analyze trends on a broader scale. Figure 3.5 below shows the locations of these wells where the majority are gathered in the South West of the Netherlands, which also corresponds to the West Netherlands Basin.

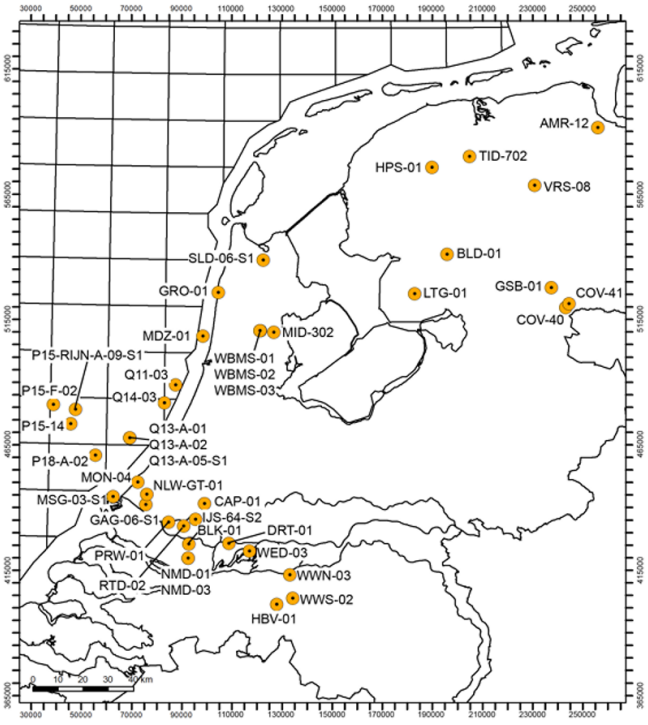

Figure 3.5: Location of wells in the Netherlands from which acoustic data were obtained from the public geomechanical data on nlog.nl.

4 Laboratory experiments

After preparing all the samples, the laboratory experiment setup was specifically prepared with mainly two machines, as seen in Figure 4.1 below. The main test done is the triaxial compression with acoustics measurements, and each will be discussed in this section.

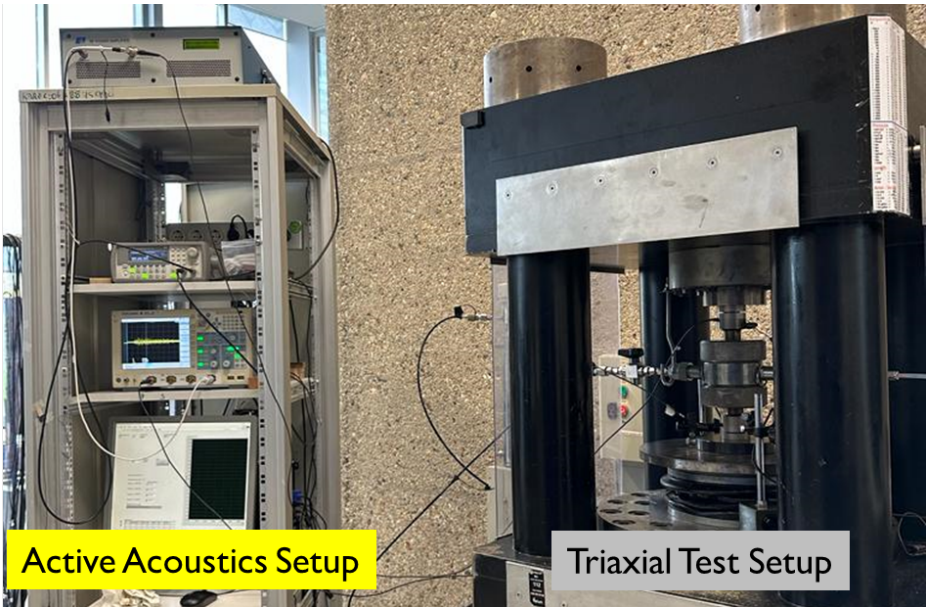

Figure 4.1: Setups of the Triaxial Compression test and the active acoustic measurement

4.1 Triaxial Compression tests

In a triaxial compression test, a cylindrical rock sample is subjected to an axial (vertical) compressive stress and a confining (lateral) stress applied by a fluid in a pressure chamber (Farahmand, 2014). These tests measure rock strength under confining pressure, which is a good representation of deep underground conditions. In these tests, the axial stress (σ_1) is applied vertically through a piston. The confining stress ($\sigma_2 = \sigma_3$) is applied laterally by pressurized fluid in the chamber surrounding the sample, where this creates a stress state where $\sigma_1 > \sigma_2 = \sigma_3$ (Jaeger, 2007).

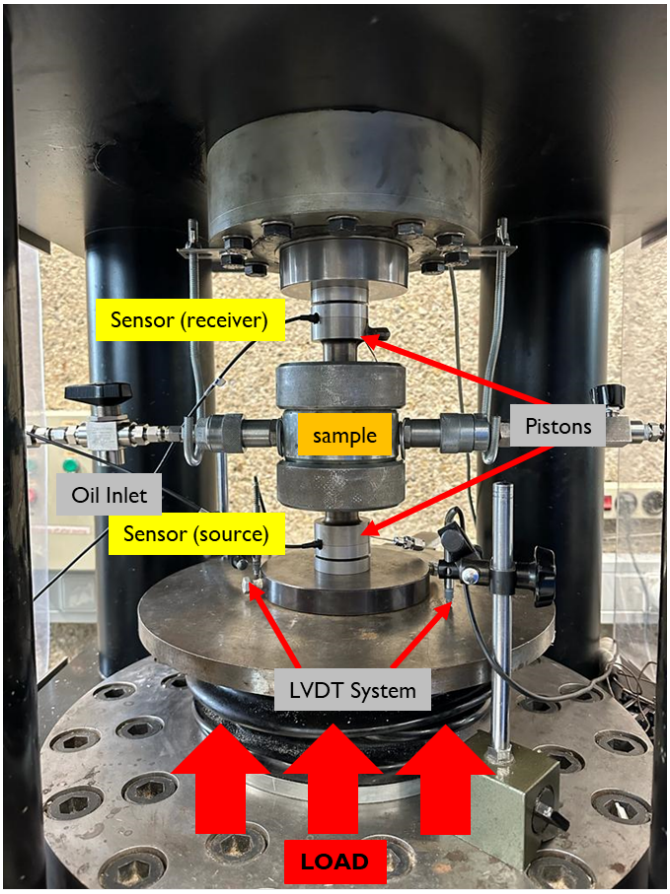

Figure 4.2: Experimental setup of the triaxial compression test. Indicated are the LVDTs at opposite sides of the plate to measure an averaged axial deformation, the hoek cell with the sample inside, and the pistons where the active-source acoustic sensors are located.

Rock samples used for the test setup shown in Figure 4.2 are cylindrical in shape, with a length-to-diameter ratio of 2-2.5. The size of the sample dictated how it was prepared in the Hoek cell. Some samples had diameters of around 25 mm and lengths of 50 mm, while others were approximately 22.5 mm by 45 mm, and some even went down in size to 19 mm by 38 mm. This variation in size necessitated different pistons and an additional layer of rubber between the oil-protective sleeve and the sample to fill any space. Looking at Figure 4.2, the main components of a triaxial test setup are a load frame with positions placed vertically to the sample to apply axial load on the top and the base of the sample. Sealed pressure chamber (Hoek cell) surrounding sample. Also, a pressure system to pressurize the chamber and apply confining pressure. LVDTs to measure sample deformation and data acquisition system (Farahmand, 2014).

For the test procedure, the sleeve of the Hoek cell has a minimum internal diameter of 30 mm. Therefore, the samples are placed in a rubber jacket inside the Hoek cell. Once the sample is inserted inside the Hoek cell and centred, the pistons are also inserted, ensuring the centralisation of the sample inside the cell while fully touching the sample. In this stage, it is essential for the pistons to push completely against the flat surface of the sample to ensure an equal distribution of the axial stress on the top and bottom surface area of the samples, as well as to ensure good-quality recordings of the acoustic data that will be discussed later in this section. Once the previous step was done, a small amount of oil was pumped with the 'Isco Pomp' to increase the Pc inside (0.5 MPa) to hold the pistons in place. Then the cell was positioned in the center of the bottom and top plates (important for equal distribution of the stress to the sample) and locked by applying some force by elevating the bottom plate.
The triaxial testing experiment consisted of five loading cycles with gradual increasing and decreasing stress application at equal rates. In each cycle, a different confining pressure (Pc) ranging from 10 to 50 MPa in 10 MPa increments was used. Between these cycles, the unloading goes down to an axial stress approximately 5 MPa above the Pc for each subsequent cycle. Importantly, the tests stayed within the elastic deformation range in each cycle by restricting the axial stress to 2 to 3 times Pc, in order to simulate safe CO2 injection procedures for these types

of reservoirs. It is important to note that in this test confining pressure is applied by pressurizing the cell, axial pressure is applied by advancing the vertical piston, and measurements of load, deformation, and acoustic emissions are monitored (Jaeger, 2007).
As axial load is applied, the sample shortens and bulges out radially. The LVDTs precisely measure these deformations along the length of the sample. From the deformation data, axial strain values are calculated as a function of the applied stresses. These strain measurements allow the determination of the elastic moduli (Mechanical Young's modulus).
In this mechanical part of the test, the main parameter calculated from the stress and strain measurements is the mechanical (static) young's modulus which is calculated from the slope of the line in the stress vs. strain crossplot that will be discussed in more detail in later sections. The Static Young's modulus equations is stated as seen in equation 4.1 where σ is the axial stress and the ε is the axial strain:

$$E_{static} = \frac{\sigma}{\varepsilon} \tag{4.1}$$

Overall, strain measurements provide critical information about the rock sample's elastic deformation behaviour under simulated subsurface stress conditions. Elastic moduli values are key inputs for numerical modeling and simulation of subsurface rock mass response to natural or induced stresses (Jaeger et al., 2007).

Machine Strain Correction
The strain in the triaxial tests need to be corrected because the measurements are based on the LVDTs positioned on the plate which which are not only reflecting the strain in the sample but also reflecting the deformations of the metal parts of the machine that are under stress. This correction procedure is essential to isolate the true strain in the sample material. To do so, we are repeating the same testing procedure with an aluminium sample for which the elastic properties are known (E_{al} = 70 GPa).
The strain of the aluminium was determined from the collected data using Equation 4.2, where E is the Young's modulus (MPa), σ the axial stress (MPa) and ε the strain. During the test, the measured total deformation includes both machine strain and aluminium strain as expressed in Equation 4.3. From this simple equation we can calculate the machine strain; as by now both, measured total strain and aluminium strain are known.

$$\varepsilon_{aluminium} = \frac{\sigma}{E_{aluminium}} \tag{4.2}$$

$$\varepsilon_{total} = \varepsilon_{mach} + \varepsilon_{aluminium} \tag{4.3}$$

By calculating the machine strain, it was subtracted from the total strain for each tested sample using a code developed by myself to ensure that the the strains subtracted from each other are corresponding to the same pressure values. This analysis provided the Young's modulus by fitting a linear regression line of the stress-corrected sample strain curve for each cycle.
It is important to mention that the results shown in Sections 5.1 and 6 are after implementing this correction.

4.2 Active-source Acoustics

Active acoustic measurements during triaxial compression testing involve propagating waves through a sample to record its mechanical properties as it is compressed. A wave generator and amplifier are necessary to transmit the wave through a transducer in the bottom piston, as shown in Figure 4.3. The acoustic signal travels through the bottom piston, sample, until it reaches the receiver transducer in the top piston. The receiving transducer is chosen to be on top in an attempt to decrease the potential of picking up any noise coming from the loading frame at the bottom of the setup. The information collected by this sensor is then sent to an oscilloscope, which is connected to a computer that records the waveforms. Using P wave transducers alone would make the S wave difficult to distinguish. Therefore, a shear wave sensor is used, and the wave is transmitted every 15 seconds to obtain both P and S waves. In Figure 4.2, the transducers' locations are indicated, and Figure 4.3 shows the equipment used for the active acoustic measurements.

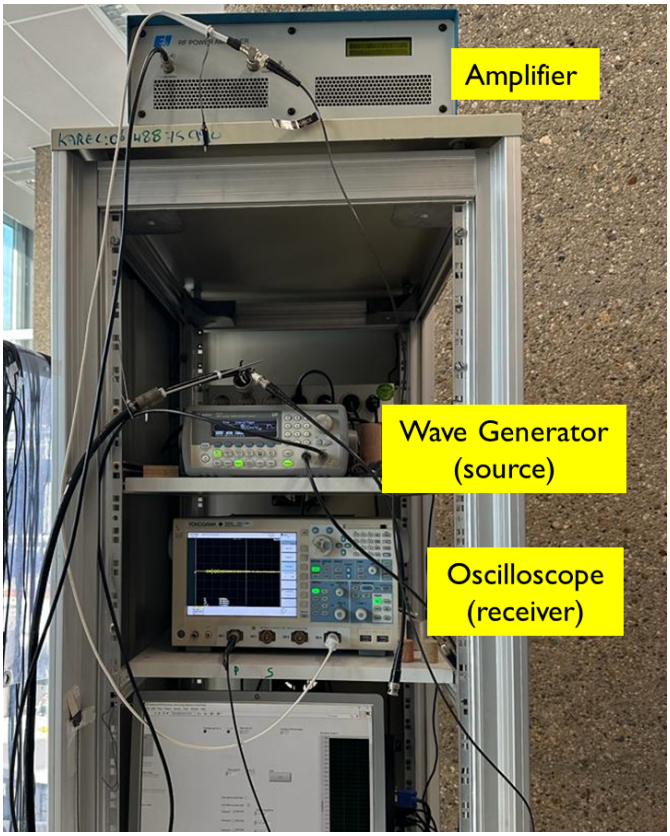

Figure 4.3: The experiment setup for the acoustic measurement equipment

The parameters set for the wave are the same for all experiments in table 4.1 below.

Table 4.1: Setup parameters for the active-acoustic recordings

Wave generator					**Oscilloscope**			**Computer**
Frequency [MHz]	**Amplitude [mV]**	**Cycle set**	**Cycle**	**Burst time [μs]**	**Sampling [kW]**	**ACQ (acquisition) Average**	**Time division [μs/div]**	**Timestep [s]**
1	800	N	1	5	125	256	100	15

Measuring the acoustic waves characterizes mechanical properties. As the sample is compressed, changes in the velocity of the acoustic wave indicate changes in the sample's elastic moduli, stiffness and internal structure. Therefore, tracking these acoustic wave variations allows the characterization of how the material's mechanical properties evolve during testing due to the sample's internal structure changes under triaxial compression.
To calculate the P-wave and S-wave velocities, the recorded acoustic traces were displayed in high resolution in self-developed Python codes in order to be able to pick the arrival times for P-wave and the S-wave, as seen in Figure 4.4 below. It shows the peaks and troughs with a certain amplitude for each trace throughout the experiment. It is important to consider that the picking times of the P and S waves contain uncertainties related to the image's low resolution; however, maintaining consistency in the picked signatures across the cycles and the samples decreases the misalignments in the results. These errors also affect other results calculated using the velocities such as Dynamic Young's modulus and the Dynamic Poisson's ratio (Siggins (1993)).

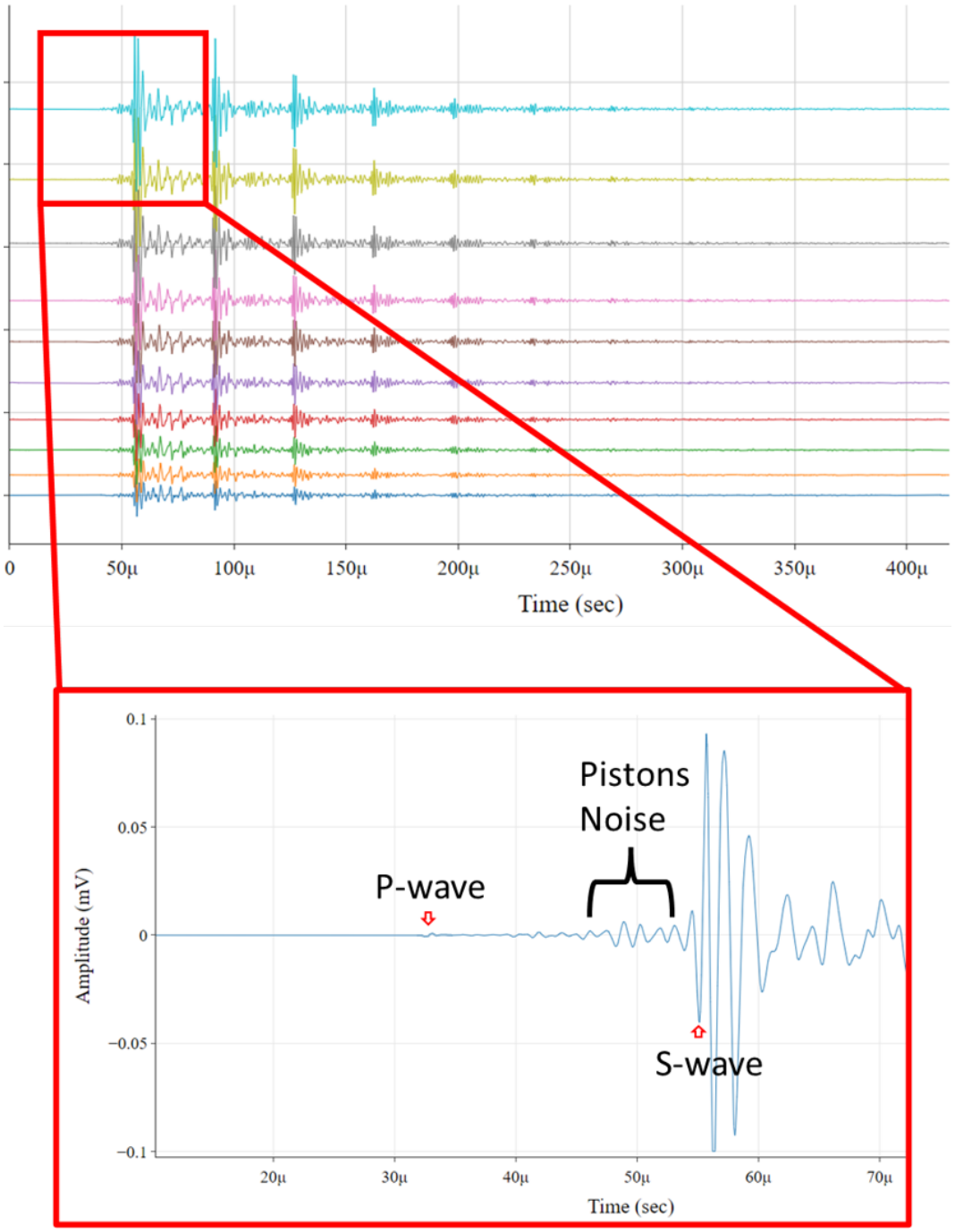

Figure 4.4: Example of a single trace where P and S arrival times are indicated in blue circles. The S selection corresponds to the start of the largest amplitude since the transducers measure a shear wave.

In order to expedite the data processing, the traces are only displayed in Python in order to determine the signature of the signal to be picked for arrival times. After that, the P and S arrival times were picked for all traces and were then calculated with the use of RadEx Pro software which allows us to visualize all of the Acoustic Traces of each loading cycle next to each other, as shown in Figure 4.5. This view shows the peaks and troughs of the recorded amplitude, which were used to pick the arrival times of both waves.

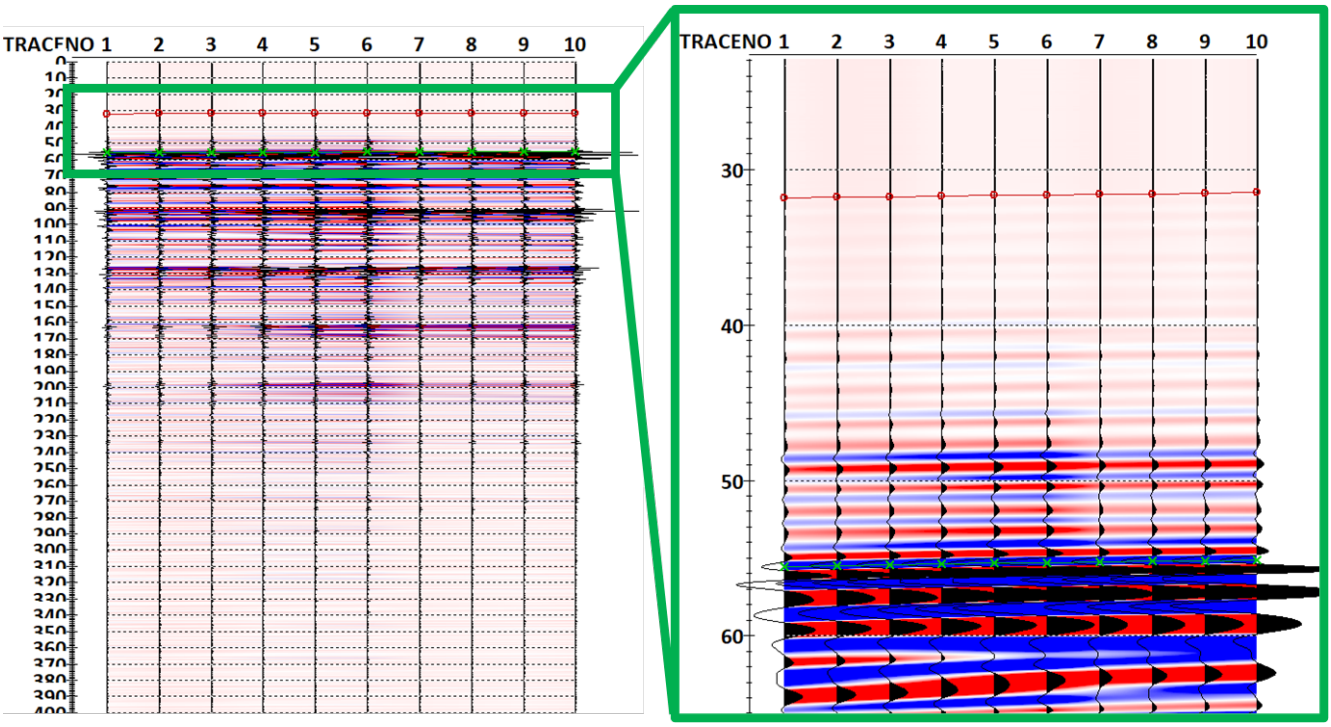

Figure 4.5: Example of a RadEx view of each trace amplitude recorded during a cycle versus time. Each trace is differentiated with an identification number (numbers on x-axis). This display of traces allows to pick the arrival time of the compressional (red) and shear (green) waves more easily, differentiating the change of amplitudes faster.

Acoustic Data Correction

In order to calculate the most representative dynamic properties from a triaxial compression test with acoustic measurements, care must be taken to correct the raw data prior to analysis, mainly the acoustic arrival times and the corrected strain values (deformation). Accordingly, the sample length is calculated at each measurement point based on the corrected strain rather than assuming a constant sample length.
For the arrival times correction, we need to account that the transducers are inside the pistons and not in direct contact with the sample. The wave first travels from the bottom transducer through one piston, then the sample, and again through the second piston until it arrives at the top transducer. Therefore, the measurement received is not just from the sample and needs to be corrected. To do this, we take a measurement with just the pistons and no sample in between. By subtracting the arrival times of the P and S waves, we can correct for these discrepancies and obtain an accurate acoustic wave measurement from the sample.

Once we have all three factors corrected, sample length and arrival times, we can proceed with calculating the wave velocities and elastic parameters.

Obtained Elastic Parameters from Acoustic Recordings

After performing all three necessary corrections, multiple parameters can be calculated in order to have a broader understanding of the samples. The elastic parameters provide critical inputs for geomechanical models to assess reservoir integrity, injectivity, and containment assurance in carbon storage projects.

The key parameter calculated is the dynamic elastic modulus (E_d) which characterizes the elastic stiffness of the material under dynamic loading via wave velocities recordings. This parameter It depends on the density of the sample (ρ) in kg/m^3 and the measured velocities (V_p and V_s in m/s) as shown in Equation 4.4 obtained from (Mavko, 1998).

$$E_d = \frac{\rho V_S^2 \left(3V_P^2 - 4V_S^2\right)}{V_P^2 - V_S^2} \tag{4.4}$$

Through the velocities, it was possible to calculate the Poisson's ratio (ν) using Equation 4.5 (Mavko, 1998). It is the ratio of transverse to axial strain under dynamic loading. Relates compression and extension. Understanding Poisson's ratio can help predict how the injection of CO2 will affect the stress state of the reservoir rock. It helps determine reservoir compressibility and pressure buildup. It is specifically important for predicting borehole wall stability. Higher ν leads to more fracturing and breakouts (Zoback, 2006).

$$\nu_d = \frac{V_P^2 - 2V_S^2}{2\,(V_P^2 - V_S^2)} \tag{4.5}$$

Another important elastic modulus is Bulk Modulus (K). It measures the uniform incompressibility of a material under dynamic loading. This modulus is critical for estimating subsurface volume changes and surface subsidence during CO2 injection (Rutqvist, 2012). It indicates potential pore collapse, whereas low K indicates high compressibility, which is undesirable for a CO2 injection project. Dynamic bulk modulus can be computed from velocity and density data using the relationship proposed by (Jizba 1992; Brinson and Brinson 2008; Archer andRasouli 2012) given in Equation 4.6 below:

$$K = \rho(V_P^2 - \frac{4}{3}V_S^2) \tag{4.6}$$

Shear modulus is the degree to which a material can resist shearing stress and withstand shearing. Dynamic shear modulus can be estimated from density measurements and sonic-derived P-wave using the relation of Mavko et. al. (1998), as seen in Equation 4.7 below:

$$G = \rho(V_P^2) \tag{4.7}$$

The velocity Ratio plays an important part in the analysis as it indicates relative compressional and shear stiffness where higher Vp/Vs corresponds to more fractured and porous rocks.

4.3 Geomechanical Tests Summary

After explaining how the tests were performed, here is a summary of the tests of each sample and the quality of their data. In table 4.2 below, all the tests were triaxial compression tests. However, various tests with different parameters, from strain rate and the number of cycles, were done over multiple samples. For example, K15-2-8V and K08-08-16V tests were run with different strain rates where we observed either fractures or abnormal behaviour in their stress-strain curve readings and could not go up to the highest confining pressure cycle. Therefore, after these tests, we decided to choose one workflow for consistency, as seen in all the good tests in table 4.2.
In terms of the test style column in table 4.2 below, C1-C5 is referred to as the Confining Pressure cycle number and P_{ax} and P_c are referred to as the axial pressure and the confining pressure consecutively. This column means, in general, in the first cycle, the axial pressure goes up to 3 times the confining pressure in the loading phase while in the remaining four cycles, the axial pressure goes up to only two times the confining pressure. During the testing phase, prior to choosing the final workflow, we observed that for the first cycle going up to only two times, the confining pressure was not optimal where the relationship between stress and strain does not stabilize yet. The stress-strain relationship did not stabilize, likely because the sample grains were still adjusting to the pressure and reorganizing. However, in multiple cases for the remaining four cycles, if the axial pressure consistently went up to 3 times the confining pressure, multiple samples yielded plastically, where this exceeded the desired elastic behaviour for this stage of the tests. Based on these initial trials, we determined the optimal workflow is that in the first cycle, we apply an axial pressure three times the confining pressure, allowing the sample to equilibrate. Then, in the remaining cycles, maintain axial pressures safely below the yield point, typically around two times confining pressure.

Table 4.2: Triaxial Compression tests summary for all samples

Sample Name	Test Type	Test Style	Strain Rate [1/s]	Cp Cycles [Mpa]	Mechanical Test Results	Acoustic Data
K15-2-3V	Triaxial	C1:P_ax=3X P_c, C2-C5:P_ax=2X P_c	0.001	10-20-30-40-50	Good	Good
K15-2-4V	Triaxial	C1:P_ax=3X P_c, C2-C5:P_ax=2X P_c	0.001	10-20-30-40-50	Good	Good
K15-2-5V	Triaxial	C1:P_ax=3X P_c, C2-C5:P_ax=2X P_c	0.001	10-20-30-40-50	Good	Good
k15-2-7V	Triaxial	C1:P_ax=3X P_c, C2-C5:P_ax=2X P_c	0.001	10-20-30-40-50	Good	Good
K15-2-8V	Triaxial	C1-C5:P_ax=3X P_c	0.0005	10-20-30-40	Bad	Bad
k15-12-1V	Triaxial	C1:P_ax=3X P_c, C2-C5:P_ax=2X P_c	0.001	10-20-30-40-50	Good	Good
K15-12-12V	Triaxial	C1:P_ax=3X P_c, C2-C5:P_ax=2X P_c	0.001	10-20-30-40-50	Good	Good
K15-12-14V	Triaxial	C1:P_ax=3X P_c, C2-C5:P_ax=2X P_c	0.001	10-20-30-40-50	Good	Good
k15-12-21V	Triaxial	C1:P_ax=3X P_c, C2-C5:P_ax=2X P_c	0.001	10-20-30-40-50	Good	Good
K15-15A-4V	Triaxial	C1:P_ax=3X P_c, C2-C5:P_ax=2X P_c	0.001	10-20-30-40-50	Good	Good
K15-15A-5V	Triaxial	C1-C5:P_ax=3X P_c	0.001	10-20-30-40-50	Bad	Bad
K15-15A-6V	Triaxial	C1:P_ax=3X P_c, C2-C5:P_ax=2X P_c	0.001	10-20-30-40-50	Good	Good
K15-15A-13V	Triaxial	C1:P_ax=3X P_c, C2-C5:P_ax=2X P_c	0.001	10-20-30-40-50	Good	Good
K15-FG-102-2V	Triaxial	Each Cycle: Upto Plastic Zone	0.001	10-20-30-40-50	Good	Good
K15-FG-102-2V	Triaxial	C1:P_ax=3X P_c, C2-C5:P_ax=2X P_c	0.001	10-20-30-40-50	Good	Bad
K15-FG-102-04V	Triaxial	C1:P_ax=3X P_c, C2-C5:P_ax=2X P_c	0.001	10-20-30-40-50	Good	Good
K08-08	Triaxial	C1:P_ax=3X P_c, C2-C5:P_ax=2X P_c	0.0005	10-20-30	Bad	Bad
L09-10-5VB	Triaxial	C1:P_ax=3X P_c, C2-C5:P_ax=2X P_c	0.001	10-20-30-40-50	Good	Good
L09-10-6VA	Triaxial	C1:P_ax=3X P_c, C2-C5:P_ax=2X P_c	0.001	10-20-30-40-50	Good	Good
L09-10-14VA	Triaxial	C1:P_ax=3X P_c	0.001	10	Bad	Bad

5 Results & Data Analysis

This section presents results from both lab experiments on core samples and well log data from the field.
The samples data results section displays mechanical and acoustic data obtained from the UCS machine (500 kN) while being hooked to the active acoustic source equipment, as discussed in the experiments section. Well log data are from the reservoir intervals of interest, and some offset wells, are also shown in this section.
The goal is to analyse each dataset separately and then integrate the lab sample measurements with the log data to leverage both datasets in characterizing the reservoir. Comparisons and correlations between the two provide broader geomechanical insights. It is important to note that all the data here are displayed and analyzed using Python codes I developed for this thesis project.

5.1 Samples Data

This section will first present the mechanical data to determine the static Young's modulus eventually. Next, the acoustic measurement results will be reviewed to analyze the dynamic Young's modulus and other elastic parameters derived from the acoustic wave velocities and sample densities. Finally, the results of the two data sets will be correlated.
Throughout the analysis, it is important to note that Young's modulus obtained from mechanical data is called static, while Young's modulus from acoustic data is referred to as dynamic. The static Young's modulus is measured from the static points on the stress-strain curve, represented in the curve's linear part. While the dynamic Young's modulus measurements involve using acoustic waves propagating through the material as it is loading, representing a "dynamic" analysis of the full wave data.

5.1.1 Mechanical Data

5.1.1.1 Stress-strain Cycles

The first plot in this section is the most direct one to obtain, which is the Stress-strain plot for all the cycles and all the samples, as seen in Figure 5.1. The stress applied to each sample was determined by measuring the force exerted by the testing machine and dividing it by the sample's cross-sectional area. The strain is obtained and then corrected from the LVDTs that measured the displacement of the plate. Figure 5.1 below shows variations in the results of the stress-strain curves between the samples that could be related to their heterogeneity. This difference in stiffness is strongly correlated to their disparity in porosity and lithology. Table 3.2 indicates how variable the measurements were in these samples in terms of porosity, density and lithology.

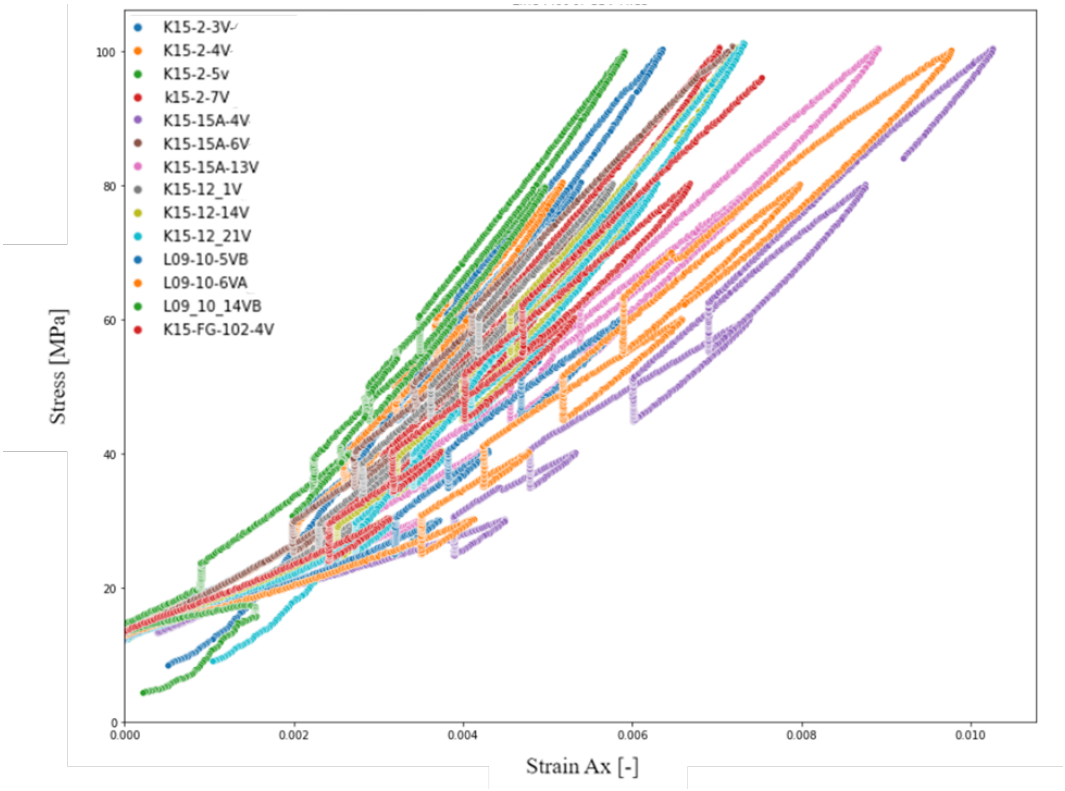

Figure 5.1: Stress-strain plots for all the samples included in the study

All these samples have been tested the same way; all experiments were performed with a triaxial compression test with five confining pressure cycles at 10 MPa, 20 MPa, 30 MPa, 40 MPa and finally, 50 MPa confining pressure cycle. Figure 5.2 below displays the entire test of one sample, as an example, to look into more detail how each test was run with each cycle. Figure 5.2 (a) shows the stress-strain cross plot in which each cycle is assigned a colour while we can also observe the loading and the unloading part of each cycle as indicated by the green and red arrows. Cross plot (b) in the same figure shows how stress and stress change per cycle with time, and the loading and unloading parts are also indicated as green and red arrows.

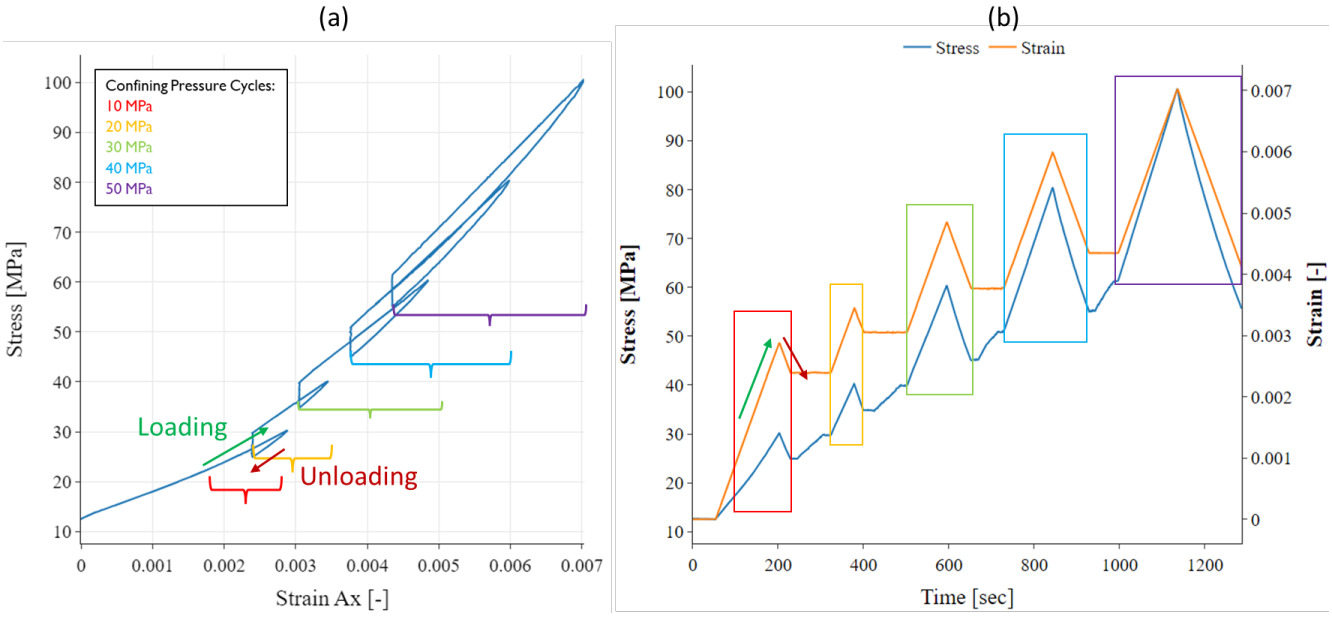

Figure 5.2: (a) Stress-strain plot for one sample displaying all the confining pressure cycles. (b) stress & strain vs time plot

To analyze the cycles, primarily to understand and quantify the elastic regime, we need to look at the linear part of each confining pressure cycle that indicates the static Young's modulus. Looking at Figure 5.3, the full test is shown on the left, while the right shows a zoomed-in view of each confining pressure cycle. Each linear portion of each cycle was identified then a linear regression was calculated to determine the slope of each line, which is the changes in stress over the strain. Overall, from the analysis of the slope values, we can see that the slope increases with the increase of the confining pressure cycle; hence the static Young's modulus increases with the increase of confining pressure.

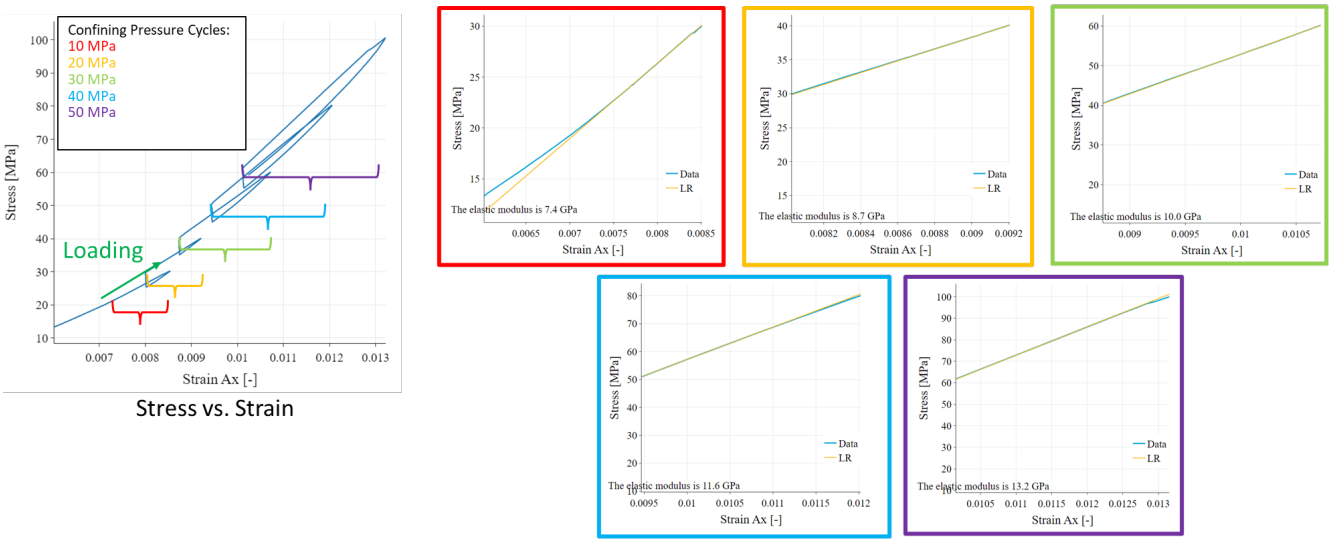

Figure 5.3: Stress-strain plots per cycle.

5.1.1.2 Static Young's Modulus Vs Confining Pressure Cycles

Figure 5.4 shows the static Young's modulus results against each confining pressure cycle for all the tested samples. The figure has five different sub-figures, each coloured with a different parameter. As in the initial observation, we can see that the static Young's modulus increases with the increase of the confining pressure. This could be due to different reasons like the confining pressure closing cracks and pores, strengthening interparticle bonding, and reducing deformability, all of which contribute to a higher static Young's modulus.

The sub-figures in 5.4 are coloured by pycnometer porosity, lab-measured density, measured depth, Gamma-ray values and deep resistivity values extracted from the log at the exact depth. Crossplot (c) is coloured by measured depth, where there was not a clear correlation between depth and the static Young's modulus. It is important to note that all these wells were vertical wells with a minor inclination, so the difference between Measured Depth and True Vertical Depth is insignificant. This could be explained by the fact that the depth range of the samples is around only 1000 meters. There was also no clear correlation between either gamma ray or resistivity with the static Young's modulus as this could be because all these samples were taken from a hydrocarbon reservoir where it was targeting sandstones and gas was found there. Hence, the resistivity is automatically high due to hydrocarbons. Also, a general reason for the low correlation between the Static Young's modulus with depth, gamma ray and resistivity could be due to the small number of samples, which could have limited seeing a larger spectrum of data ranges.

On the other hand, from crossplot (a) and (b) in Figure 5.4 there is a strong correlation between Young's modulus and density and porosity; Young's modulus increases with the increase in density but decreases with the increase in porosity.

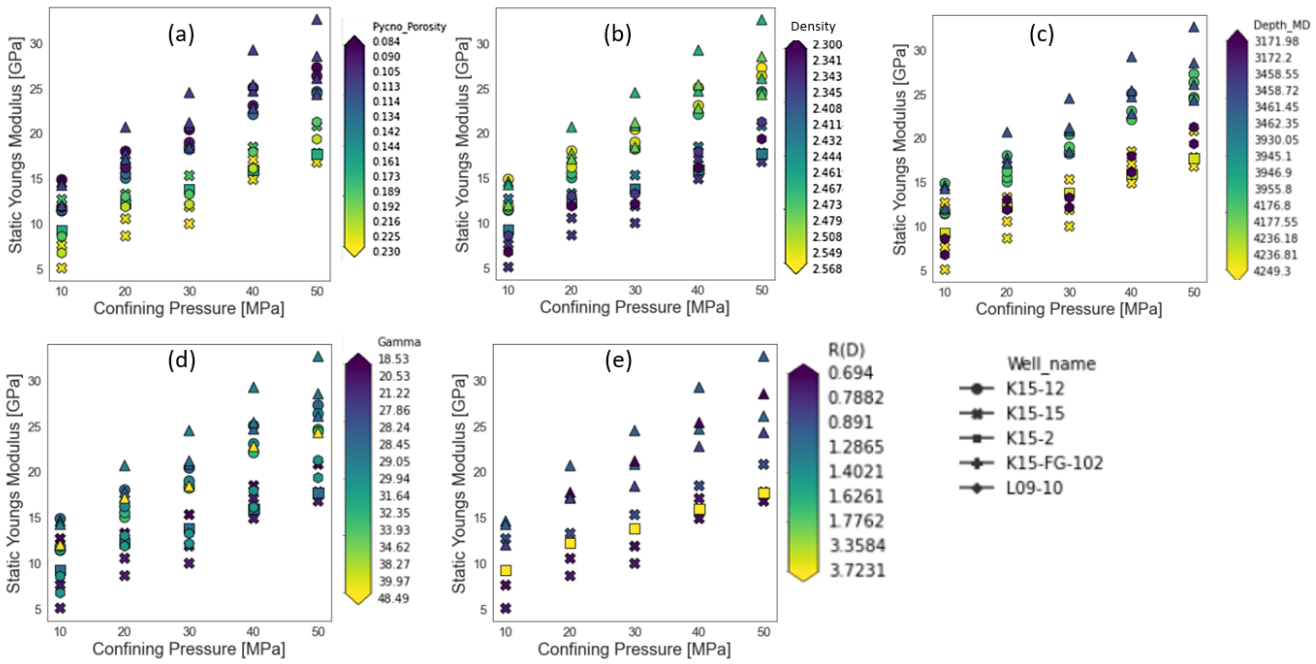

Figure 5.4: Static Young's Modulus vs confining pressure cycle plot. (a) coloured by porosity, (b) coloured by density [g/cm3], (c) coloured by measured depth [m], (d) coloured by gamma ray [gAPI], (e) coloured by deep resistivity [ohmm]

5.1.1.3 Static Young's Modulus vs Porosity & Density

Porosity and density were the parameters with the most significant correlation with the static Young's modulus from the previous figure (Figure 5.4). Therefore, I created Figure 5.5 below to display the correlation in more detail. In Figure 5.5 below, both vertical axes are static Young's modulus versus bulk density in (a) and (b) porosity. These figures visualize the correlations more and display them per confining pressure cycle, as seen in the legend. Please note that in these tests, there was no capacity to calculate the change in porosity and density during the test; these values are measured per sample before the tests.

These two plots help in clearly observing that the variations of rock parameters are directly resulting in the variations in the static Young's modulus values, where we see that in high porosity samples, we have lower Young's modulus because more pore spaces could be filled by weaker materials like water, air or hydrocarbons, which do not contribute to the stiffness of the sample. More space means less solid matrix to resist deformation. High porosity may also imply loose packing and fewer particle contacts. This reduces interparticle bonding and friction, decreasing stiffness. The opposite is the effect of density, where the higher Young's modulus values correspond to higher densities, as observed in the gathered data in Figure 5.5 (a). In both parameters, higher values of the static Young's modulus are associated with higher confining pressure, which also can be explained by the effect of pressure on closing the fractures and pore spaces, hence increasing the stiffness of the sample.

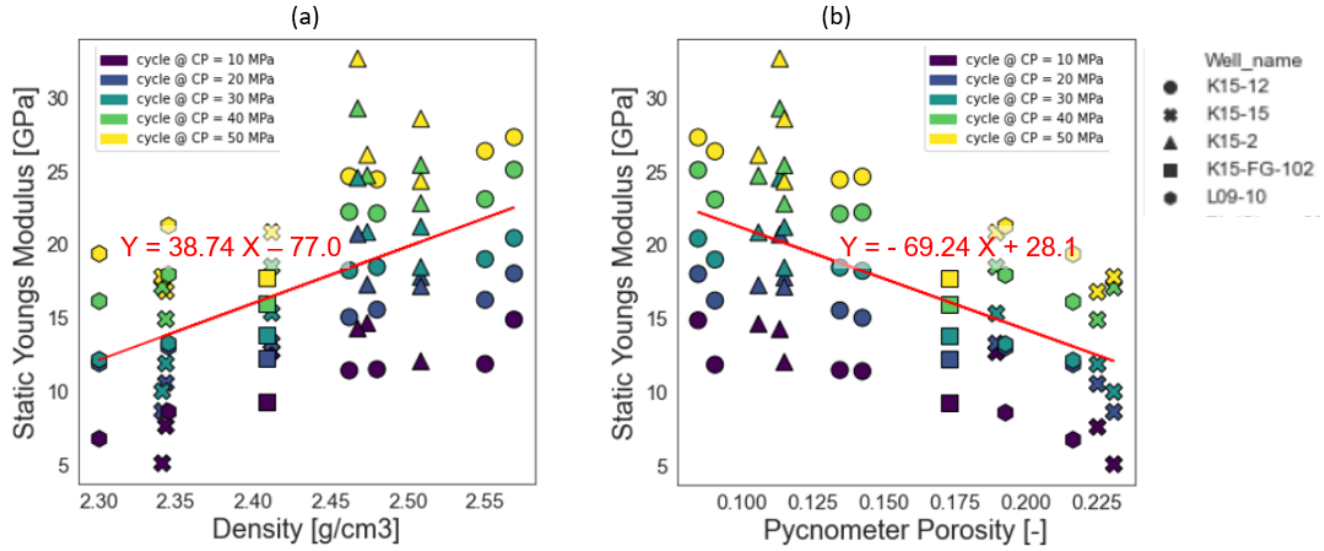

Figure 5.5: (a) Static Young's modulus vs sample density [g/cm3], (b) Static Young's modulus vs sample porosity [-], a trend line is shown in red for both rock parameters

5.1.1.4 Depth vs Static Young's Modulus

Figure 5.6 below displays Static Young's modulus and porosity with respect to depth for all the samples. It is important to note that in this plot, I displayed the results for the 30 and 50 MPa confining pressure cycles because a range between these two is the subsurface's most representative pressure at the target zone's depths. The confining pressure range (30 to 50 MPa) has been selected to represent the target reservoirs using a simple and rough estimation method that connects the confining pressure in the triaxial tests to the formation depth and in-situ stress. Due to the limitation in the data about the in-situ stress and the pore pressure in the reservoir, this simple method has been used to roughly estimate the confining pressure that simulates the in-situ stress experienced by our target reservoirs at their depth range. So, the confining pressure can be estimated from the horizontal stress equation as shown in equation 5.1 below:

$$P_c = S_{horizontal} = \frac{\nu}{1-\nu} * S_{vertical} = \frac{\nu}{1-\nu}\rho g h \tag{5.1}$$

, $S_{horizontal}$ and $S_{vertical}$ are horizontal and vertical (overburden) stresses, respectively, ν is Poisson Ratio which is roughly between 0.25 and 0.3 for sandstones, ρ is the average density in [kg/m3] of the overburden formation (2400-2500 kg/m3), g is 9.8 [m/s2], and h is formation depth in [m]. These rough calculations showed that the confining pressure that simulates the in-situ stress in our target formations and depth ranges are from around 30 MPa to 50 MPa.

Usually, porosity decreases with the increase of depth, but this correlation is not the case in our data. As we look at plots (b) and (c) in Figure 5.6, we can observe that well samples from deeper depths have higher porosity values. This could be due to multiple reasons. The fact is that porosity is measured in the lab in room conditions, so the effect of overburden is not reflected in the values. Another reason could be related to the insufficient number of samples to represent a clear trend with depth due to the heterogeneous nature of the formation. In this case, the heterogeneity of the reservoirs plays a bigger role in the porosity values than depth. As a result, when looking at plot (a), we can see the porosity variation of the samples played a larger factor in the resulting static Young's modulus values; hence the static Young's modulus is not clearly increasing with depth.

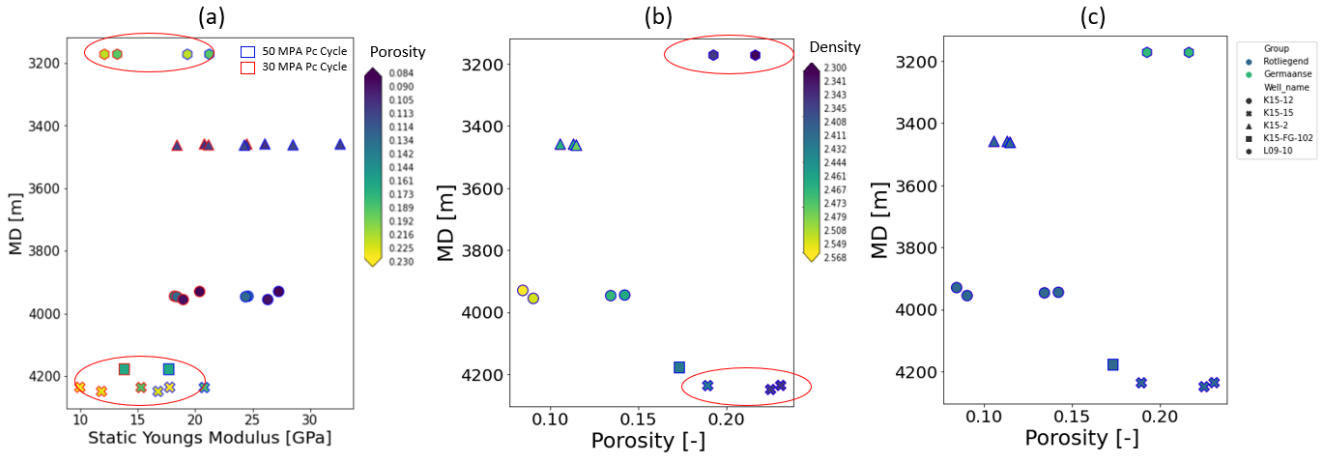

Figure 5.6: Depth vs Young's modulus and Porosity plots showing results from 30 MPa and 50 MPa Confining pressure cycles. (a) Measured depth vs Static Young's modulus coloured by porosity, (b) Measured depth vs porosity, coloured by density, (c) Measured depth vs Porosity, coloured by Stratigraphic groups

5.1.2 Acoustic Data

The acoustic data were measured actively throughout the test and saved immediately as binary data. The team developed a Python code, and modified it by myself. It displays the traces in high resolution to properly view each trace to determine the wave signature of the arrival times for both P-wave and S-wave. As discussed earlier in the dataset section, the code is basic, so it does not handle the complexity of picking the arrival times for all the traces and performing the calculations necessary to determine the elastic parameters. Therefore, after determining the arrival times signatures, RadEx Pro software is used to pick those arrival times for all traces and perform the calculations necessary to obtain all desired elastic moduli, where the results will be shown in this section.
It is important to note that in this section, the acoustic data that were analyzed were from the traces recorded during the loading part of the cycles and, more specifically, the linear part for a more precise view of the elastic regime analysis.

5.1.2.1 P-wave Velocity Cross Plots

P-wave & S-wave Velocities vs Confining Pressure & Axial Pressure

Figure 5.7 below illustrates two plots representing the calculated P-wave and S-wave velocities per trace for each confining pressure cycle. Sub-figure (a) shows the results from one sample where we can observe an increase in velocity value per trace where the trace represents the recorded values every 15 seconds. Also, as the confining pressure increases, we can see a noticeable rise in velocity values. This is depicted through the varying colours of the cycles. The same observation was found when displaying all the samples' results in subfigure (b).

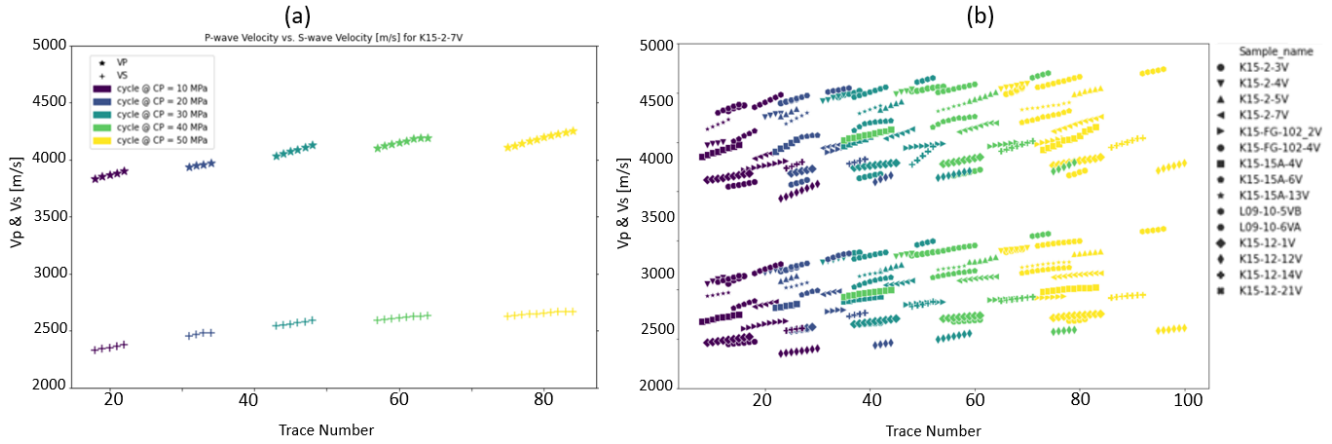

Figure 5.7: Wave velocities per trace for all cycles. (a) one sample, (b) all samples

To look at the velocities from another angle, they were plotted against the axial pressure while the data points were colour-coded based on the confining pressure cycles as seen in Figure 5.8 below. Sub-figure (a) displays the data points from all the samples revealing a positive correlation between velocity and axial pressure. Sub-figure (b) focuses on the average velocity values from the traces per cycle per sample and depicts a difference in the slope of the relationship between velocities and axial pressure. The low confining pressure cycles have a steeper slope than the higher confining pressure cycles. This indicates that this relationship becomes less sensitive at higher confining pressures, potentially as the material deformation mechanism becomes suppressed due to closing fractures and pores and an increase in the density of the material, which restricts the deformation.

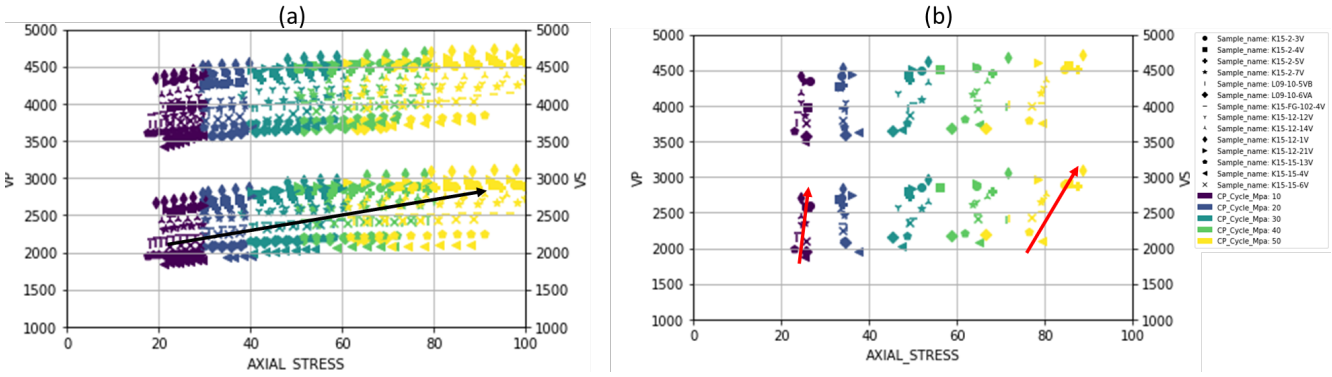

Figure 5.8: Velocities vs. Axial pressure. (a) velocity calculations for all traces for all samples, (b) average velocity per cycle and per sample

It is important now to see how the velocities correlate with the confining pressure in a clearer view while analyzing its relationship to other parameters. Figure 5.9 below depicts the Velocities on the y-axis against the confining pressure cycles; each of the plots is coloured with a different parameter. The velocities increase with the increase of confining pressure. We can observe that the velocity ranges, for example, in the 10 MPa confining pressure cycle are 3500-4400 m/s for the P-wave and 1900-2700 m/s while the 50 MPa confining pressure cycles have velocity ranges of 3700-4700 m/s for the P-wave velocity and 2100-3100 m/s for the S-wave velocities for all the samples. This phenomenon is also related to what is causing the porosity values to decrease, density to increase as well as axial pressure to increase; the closure of cracks and pore spaces and the displacement of the fluids (squeezed out) as more pressure is applied so that the velocities are travelled faster in such medium.
The same observation that was discussed in figure 5.4 is observed here. The only two parameters that we can find a clear correlation with velocities are the porosity and the density. Other parameters like gamma ray and resistivity did not have a clear correlation from the sample data.

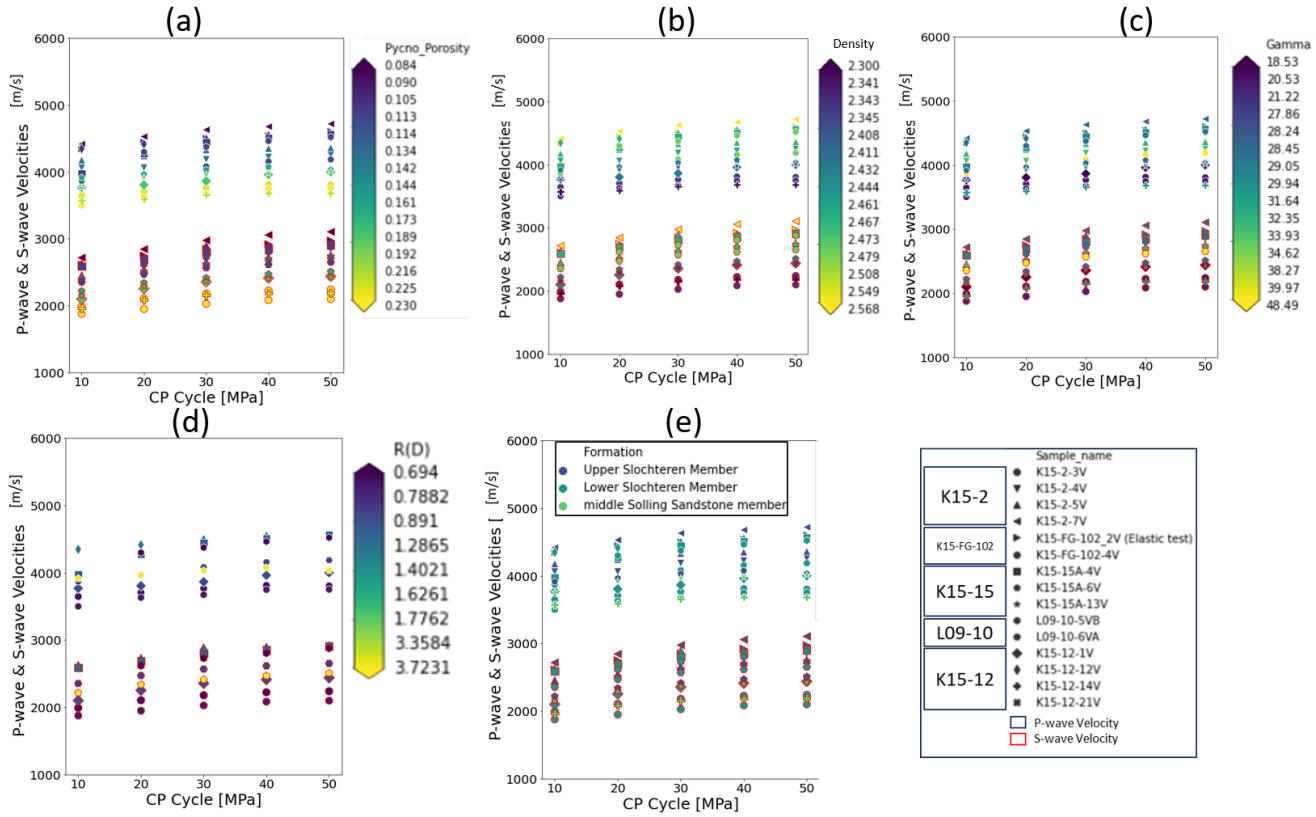

Figure 5.9: Wave velocities vs confining pressure cycles [MPa]. (a) coloured by porosity [-], (b) coloured by density [g/cm3], (c) coloured by gamma-ray [gAPI], (d) coloured by deep resistivity [ohmm], (e) coloured by formation

Figure 5.10 below looks into the trend of change in velocity with the increase of confining pressure in more detail. We can observe that the general trend shows that velocities have positive correlations with the confining pressure, but when we zoom into the curve further, we observe that the increase is steeper in the lower confining pressure cycles and gradually becomes less steep, especially after the 30 MPa cycle. This could be related to the closure of pores, where this initial nonlinear increase has been observed in many sedimentary rocks and is attributed to the closure of pre-existing microcracks under pressure (Sharma & Tutuncu, 2016). The non-linear part is not clearly observed here, but we can clearly see the difference in the slope between the low and the higher confining pressure cycles; as confining pressure increases further, the velocity increase gradually becomes less steep, exhibiting more linear behaviour as porosity reduction dominates over microcrack closure (Mavko et al., 1998). At higher confining pressure, I expect the curve to reach a plateau as porosity approaches zero and the material fully compacts.
Asef el.at, (2013) obtained similar trends of wave velocity versus confining pressure through laboratory experiments carried out in limestones. The results in this paper show that the initial exponential increase of the velocity at lower P_c than 15 MPa and a following linear trend.

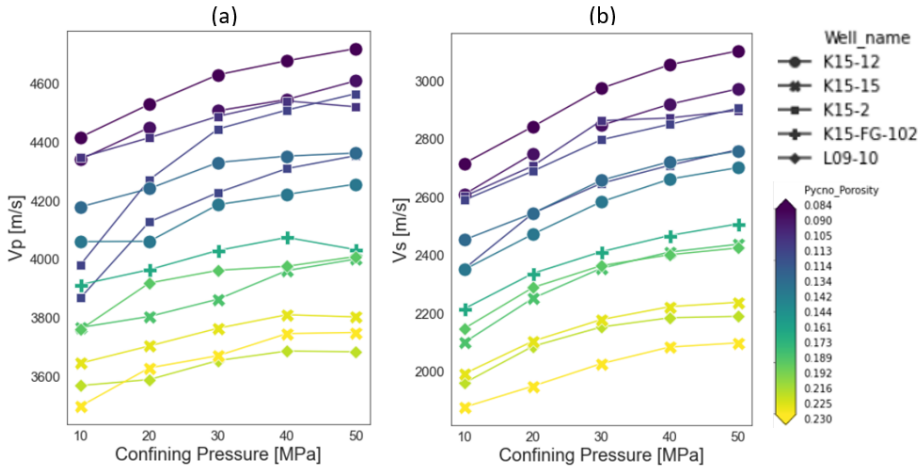

Figure 5.10: Wave velocities vs confining pressure cycles displaying velocity changes with Pc. (a) Vp Curve, coloured by porosity, (b) Vs, coloured by porosity

P-wave & S-wave Velocities vs Density & Porosity

As the previous figure (5.9) shows a positive correlation between wave velocities and densities and a negative correlation between wave velocities and porosity. This is highlighted more in Figure 5.11 below. Higher porosity corresponds to lower stiffness and greater discontinuities, allowing seismic waves to travel slower through the material.
We discussed earlier that the correlation between Static Young's modulus and depth was not clear. We have observed a similar lack of dependency between velocities and depth in sub-figure (a). It mainly could be due to the insufficient number of samples and inherent variability in properties where the formations are heavily heterogeneous with abrupt lithology changes or the existence of fractures (Christensen & Mooney, 1995).

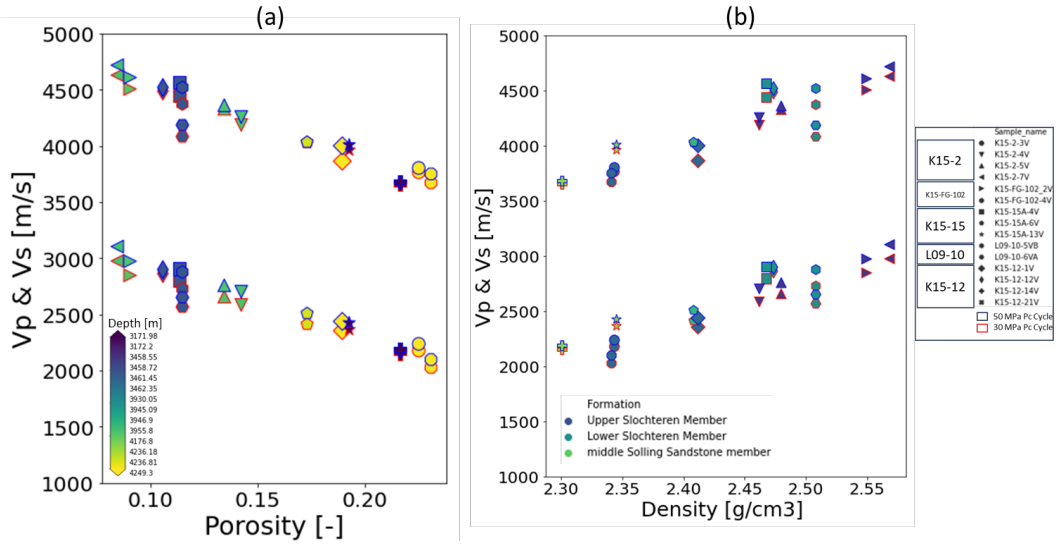

Figure 5.11: (a) Wave velocities vs porosity, coloured by depth. (b) Wave velocities vs density, coloured by formation

P-wave vs S-wave Velocities

Figure 5.12 below displays the relationship obtained from the lab experiments between the wave velocities, where the relationship can be defined as seen in equations 5.2, 5.3, 5.4 below for both the 30 & 50 MPa confining pressure

cycles and the average as well. The relationships overall have a high correlation coefficient of above 0.9.

$$V_s = 0.8891V_p - 1146.15 \tag{5.2}$$

$$V_s = 0.9135V_p - 1224.75 \tag{5.3}$$

$$V_s = 0.9059V_p - 1204.23 \tag{5.4}$$

In Figure 5.12 below, we can observe that overall the variability of the velocities is heavily dependent on the porosity and density variability as shown in sub-figure (a) and (b). In terms of other parameters, we can observe in sub-figure (e) that the sample with unconsolidated sand, mostly the L09-10 samples, has the lowest porosity and density and, therefore, the lowest wave velocities. With more samples, I believe this lithology description has the potential to be correlatable with velocities. Other parameters like the resistivity, gamma ray and the observations of bands in the lithology, as seen in the samples pictures in figure 3.3 in samples K15-2-5V and K15-12-21V, do not affect the velocities, which we will need further investigation of the cause of these bands whether it is structural, mineralogy or it is just a colour difference of the same particles.

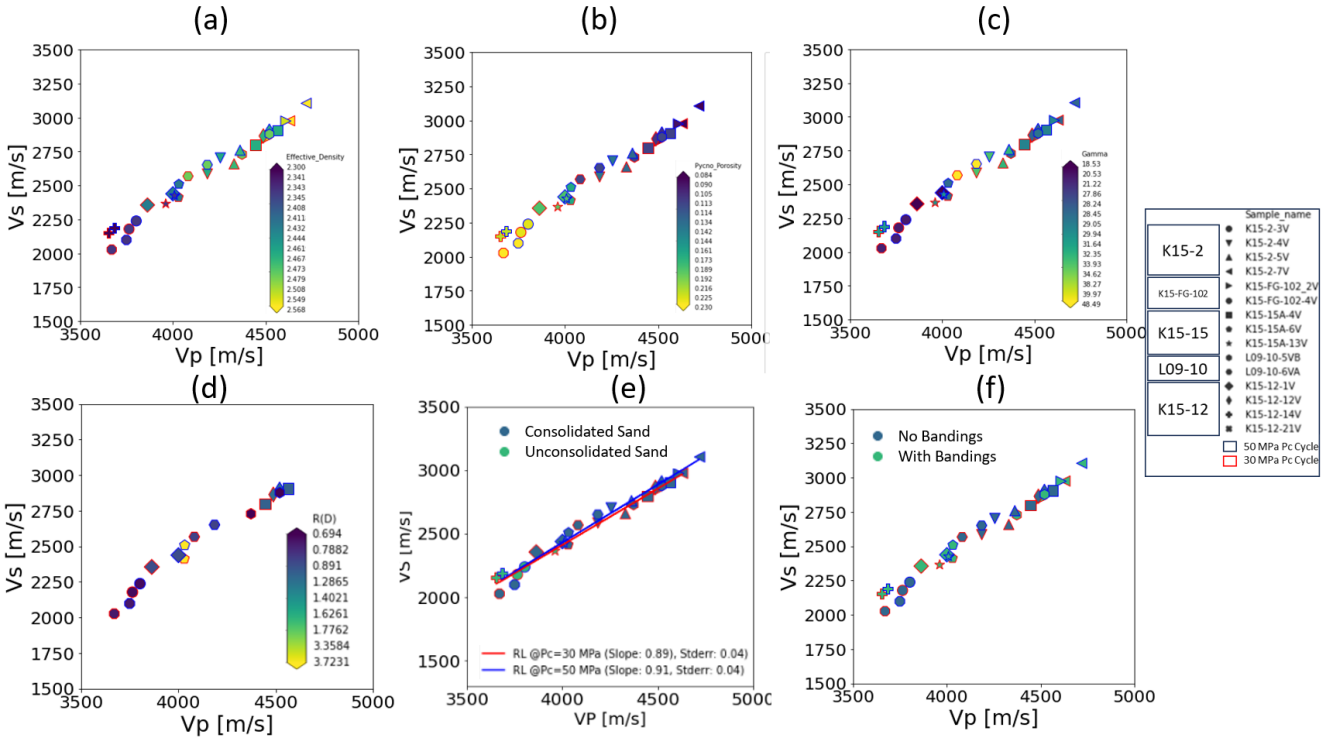

Figure 5.12: Vs-Vp plot. (a) coloured by density, (b) coloured by porosity [-], (c) coloured by gamma ray [gAPI], (d) coloured by Deep resistivity [ohmm], (e) and (f) coloured by lithology description

5.1.2.2 Elastic Moduli Cross Plots

Here I would like to show the results of mainly the dynamic Young's modulus and some other elastic moduli from bulk modulus, shear modulus, Poisson ratio, and Velocity Ratio (Vp/Vs).

Elastic Moduli vs Confining Pressure Cycles

Figure 5.13 displays five different plots of elastic moduli, and all of them are coloured with porosity since this parameter is one of the two most correlated parameters to data variations, as discussed previously. In subfigure (a), we can see a positive trend of the dynamic Young's modulus with the confining pressure; we observe a very similar trend to the one we saw in the wave velocities in figure 5.9. The dynamic Young's modulus increases with confining pressure as microcracks and fractures are progressively closed. In terms of the rate of increase, it declines in higher confining pressure as a lot of the voids are closing, which is the same as observed earlier in the correlation between the velocities and confining pressure in Figure 5.10. A similar trend is observed in the Shear modulus, as

seen in subfigure (c). However, when looking at the bulk modulus curve, the trends do not match the expectation of having a clear positive correlation with confining pressure. It could be due to local variations in composition, cementation, microcracks etc., which could lead to scattered bulk modulus values.
In subfigures (d) and (e), we consecutively observe the negative trends of the Poisson and velocity ratios with confining pressure. Both parameters increase with the increase of porosity and decrease with the increase of confining pressure. For Poisson Ratio, the trend generally shows a gradual decline as the shear modulus strengthens faster than the bulk modulus under confinement. In other words, the rock becomes stiffer and more resistant to lateral strain. When it comes to the velocity ratio, it decreases with the increase of pressure as the closure of microcracks and pores affects shear wave velocity (Vs) more than compressional velocity (Vp), bringing Vp and Vs closer together. It increases with porosity because, in porous media, Vp travels faster than Vs due to the effect of pore fluids (water, air and hydrocarbons), but when the fluids are squeezed out, it reduces the velocity contrasts.

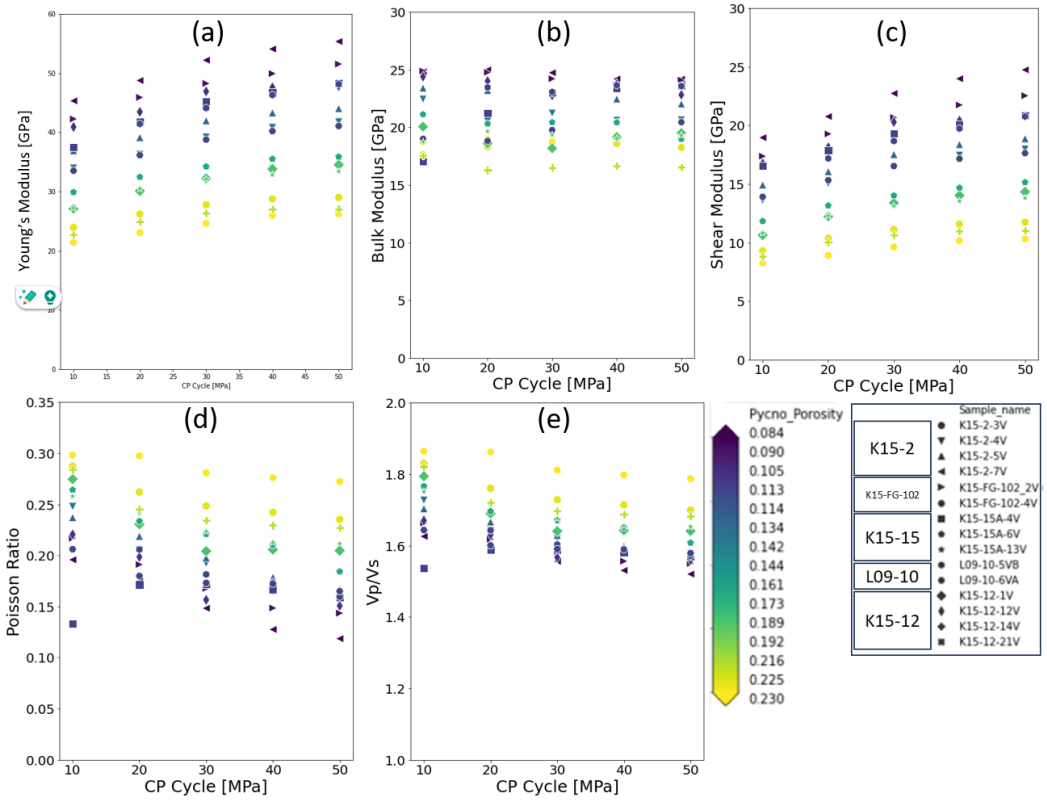

Figure 5.13: Elastic Moduli vs. confining pressure [MPa], coloured by porosity. (a) Dynamic Young's modulus [GPa], (b) Bulk Modulus [GPa], (c) Shear Modulus [GPa], (d) Poisson Ratio [-], (e) Velocity Ratio (Vp/Vs) [-]

Looking at the data points that correspond to the confining pressure cycles (30-50 MPa) while keeping in mind the porosity variability as seen in the colours bar ranging from 8% to 23%, we can determine the ranges of the elastic moduli values from the experiment. We can observe that the dynamic Young's modulus increases with the decrease of porosity from around 23 up to 56 GPa. However, the bulk modulus did not have a clear trend, but based on the literature, the values are similar to the results of geomechanial tests of rocks with a similar range of porosity. For example, at that depth, with an expected pressure of 35 MPa, bulk moduli are around 19-30 GPa (Wang et al. 2021), where our data range from 16 to around 25 GPa. The range of values for the shear modulus is around 9 to 24 GPa in my tests. The Poisson Ratio values in our sandstones range from 0.13 to 0.29, while the velocity ratios range from 1.5 up to 1.8. From Han 1986, the paper conducted compressional tests on several sandstone samples where the results of the moduli at 40 MPa confining pressure have a similar range to my results- within the same range of porosities the bulk modulus values ranged from 14 to 25 GPa, the Shear modulus was around 10 to 23 GPa, the Poisson Ratio was ranging from 0.33 down to 0.15, and lastly, the velocity ration in the paper had a range of 1.55 to 1.9.

Elastic Moduli Empirical Relations from Confining Pressure and Porosity Data

In the previous section, in Figure 5.13, we qualitatively observed how the elastic moduli change under different confining pressures and different lithologies. Generally, confining pressure simulates the subsurface's stress condition, and by increasing it in the lab, we can investigate how elastic moduli evolve with depth in the subsurface. Therefore, the quantification of the relation between the change of confining pressure and the elastic moduli can be used to predict what is happening in the subsurface.
Since the observations in 5.13 were clear in terms of elastic moduli variability dependency on confining pressure and porosity, we would like to quantitatively analyze the coupled dependency of the elastic moduli on both confining pressure and porosity. Figure 5.14 below depicts the main elastic moduli cross plots with confining pressure and porosity while displaying a linear relation extracted from both confining pressure and porosity as shown in black. Also the red and blue lines also show the predicted lines when the porosity values are at 5% and 30%, respectively.

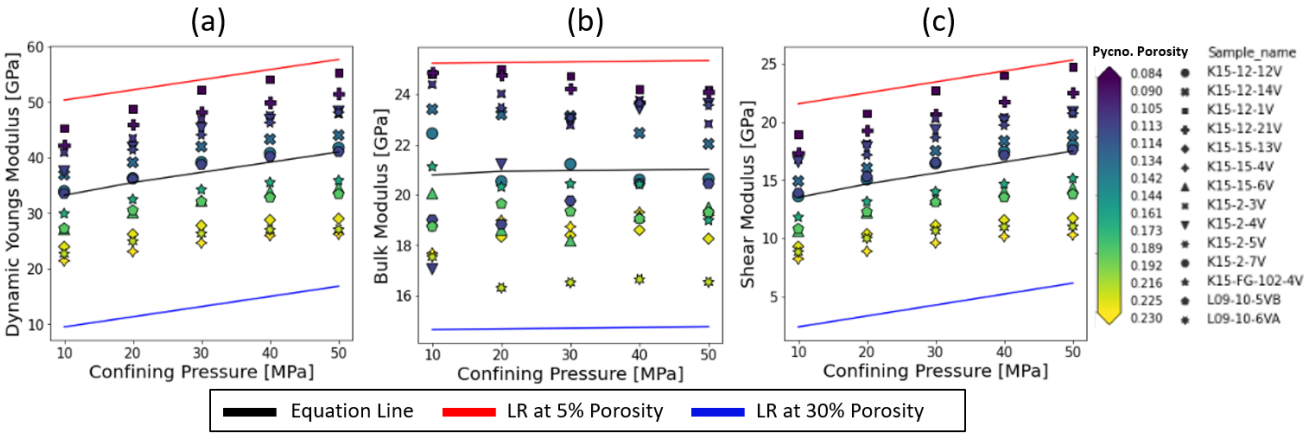

Figure 5.14: Elastic Moduli vs confining pressure [MPa], coloured by porosity. (a) Dynamic Young's modulus [GPa], (b) Bulk Modulus [GPa], (c) Shear Modulus [GPa].

The equations extracted from all the elastic moduli in 5.14 are as follows in 5.5 for the dynamic Young's modulus, 5.6 for the Bulk modulus, and 5.7 for the Shear modulus.

$$E_D = 0.1955P_c - 100.858\phi + 43.9951 \tag{5.5}$$

$$K = 0.0027P_c - 42.4166\phi + 27.3372 \tag{5.6}$$

$$G = 0.0940P_c - 76.6204\phi + 24.4542 \tag{5.7}$$

, where the moduli are in GPa and P_c is the confining pressure in MPa, and ϕ is the lab-measured porosity.

In order to QC the empirical equations calculated, crossplots between the predicted values and the measured data are created in Figure 5.15. We can see that the equations are predicting well, especially for Young's modulus in (a) and shear modulus in (c), where the values are around the best-fit line in red, which indicates a high correlation value. The correlation coefficients for the crossplots are 0.95 for both Dynamic Young's modulus and shear modulus and 0.82 for the bulk modulus in subfigure 5.15-(c). It is important to note that there are uncertainties associated with the type of model I fitted with the data, which in this case is linear, where there are two main points to be aware of. First, we can observe that the line equations do not honour the change in slope with the increase of the confining pressure. Second, the line equations have slope values biased toward the slope of the most common porosity values, where most samples have medium to high porosities. However, these linear equations can act as a first-pass prediction for geomechanical parameters behaviour understanding and modelling, especially when the data show high correlation coefficients between the predicted and the measured values.

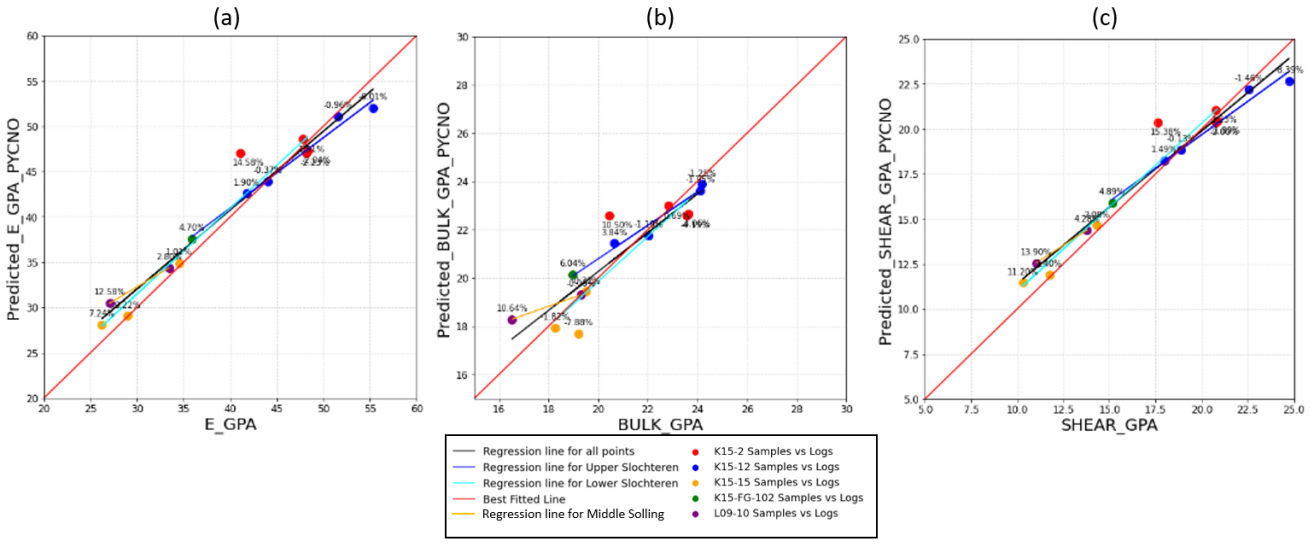

Figure 5.15: Predicted Elastic Moduli vs measured Elastic Moduli [MPa], coloured by porosity. (a) Dynamic Young's modulus [GPa], (b) Bulk Modulus [GPa], (c) Shear Modulus [GPa]

These lab-based relations help us understand the dependency of elastic properties and derive a first pass of empirical relations to estimate them at various depths using log data. Understanding how moduli evolve with stress and porosity is essential in geomechanical modelling.

5.1.3 Dynamic vs Static Young's Modulus

The dynamic versus static modulus relationship provides critical information on elastic stiffness and seismic velocities that are key for subsurface characterization and geomechanical modelling. The dynamic modulus is measured using dynamic recordings of high-frequency seismic waves, while the static modulus is measured from the static relationship between stress and strain during laboratory compression tests. Comparing the two moduli provides information on the material's sensitivity to strain rate and frequency. The ratio of dynamic to static modulus gives the velocity dispersion. For example, lower ratios imply higher dispersion and potentially more microcrack/clay influence. Also, comparisons between these two parameters can assist in differentiating pore pressure effects from pure rock mechanical property changes (Tran et al., 2002). However, quantification of the pore pressure effect is beyond the scope of this thesis due to the limitations of the machine. This section will showcase the relationship between the two moduli to provide an initial correlation directly extracted from the experiments conducted on our dataset.

In Figure 5.16 below, we can see in plot (b) the results of both the dynamic and the elastic modulus where the values generally of the static Young's modulus are lower than the dynamic modulus. More importantly, looking at their relationship in plot (a), we can see that our samples show a positive relation between the static and dynamic Young's modulus where the data correlate well with each other as their standard error is not more than 0.07 and the correlation coefficient is around 0.8 in the results of both confining pressure cycles - the 30 MPa and 50 MPa shown in red and blue consecutively.

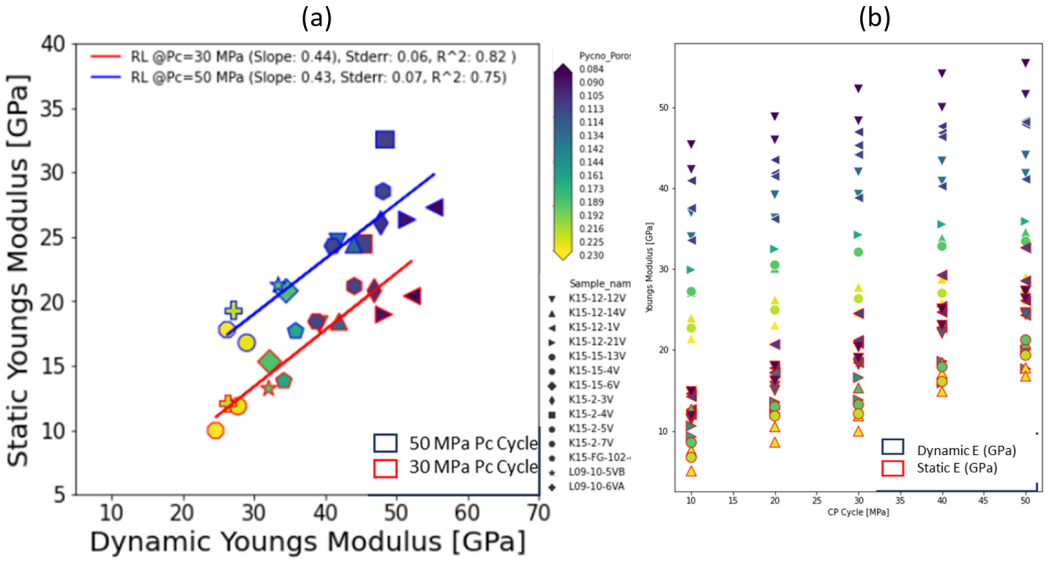

Figure 5.16: (a) Static Young's modulus vs Dynamic Young's modulus, (b) Young's Modulus vs Confining Pressure (static in red, and dynamic in blue)

From the data, we can extract these two relations from the 30 and 50 MPa confining pressure cycles shown in the order below in 5.8 and 5.9.

$$E_{stat} = 0.44E_{dyn} + 0.16 \tag{5.8}$$

$$E_{stat} = 0.43E_{dyn} + 6.13 \tag{5.9}$$

It should be noted that a distinction is made between these 'dynamic' parameters and 'static' parameters that are determined through loading and rock samples in a lab. This needs to be kept in mind for Young's modulus in particular; the dynamic values are usually larger than the static values (Eissa and Kazi, 1988). When dynamic parameters are calculated, the rock material is assumed to behave linearly in the elastic regime, to be homogenous and isotropic. These assumptions often cause the difference between dynamic and static values (McCann and Entwisle, 1992).

A number of relationships between static and dynamic Young's modulus exist in the literature, as seen below in equations 5.10 and 5.11. McCann and Entwisle (1992) used a linear trend to fit their data in equation 5.10, and their approach was based on Eissa and Kazi (1988), who devised equation 5.11 as seen below.

$$E_{stat} = 0.64E_{dyn} - 0.32 \tag{5.10}$$

$$E_{stat} = 0.74E_{dyn} - 0.82 \tag{5.11}$$

The empirical relations will now be compared to the relations developed from the lab measurements, as shown previously in both equations 5.8 and 5.9 for the 30 MPa Pc cycle and the 50 MPa Pc cycle consecutively.

All these relations were plotted against our data, as seen in Figure B.6 below. The plots show that the relations do not match the data very well, especially in the lower porosity zones and higher moduli values which could be due to potential difference in lithology between the equations from the literature and our local geology. Therefore, further samples are advised to be added to the analysis and deeper literature research to find more presentable correlations to our data in terms of lithology and test setup.

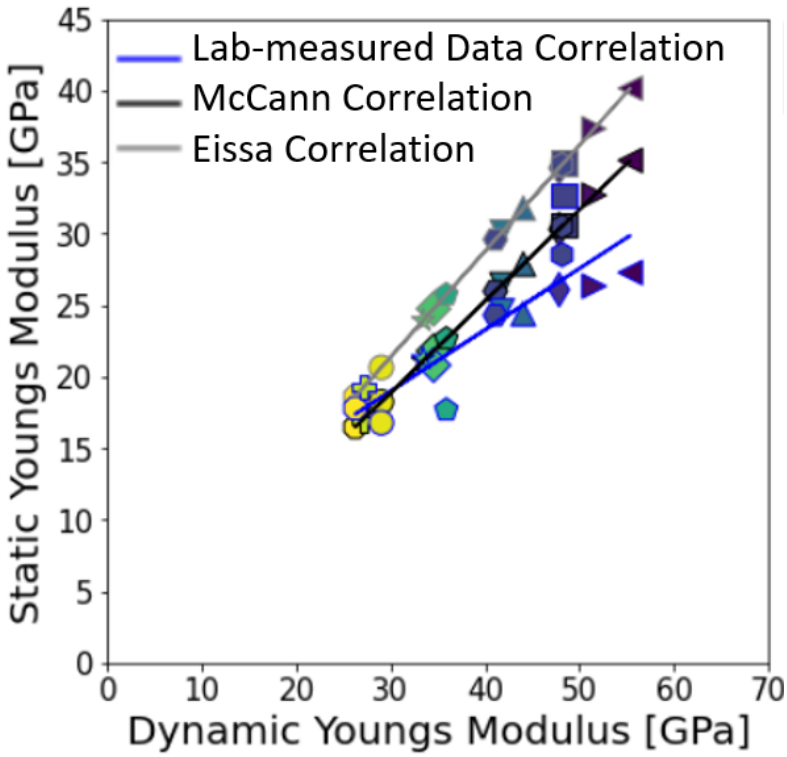

Figure 5.17: Emprical Relations for Static-Dynamic Young's moduli cross plots coloured by porosity

Accordingly, these observations infer that it is possible to predict Es based on Ed at different confining stresses. This is an important improvement for the geomechanical modelling of hydrocarbon and geothermal reservoirs because static parameters are more realistic input parameters. However, the number of samples could be insufficient to use the relation developed in this thesis project as it needs to be built on with more samples in order to solidify the outcomes.

5.2 Log Data

It is crucial to have a good understanding of the geomechanical behaviour of reservoir rocks to ensure effective carbon dioxide (CO2) injection and storage. Geomechanical tests on core samples provide essential parameter properties but have limited coverage. Well logs, on the other hand, allow for continuous evaluation along the wellbore. Linking core lab data to logs allows geomechanical properties to be estimated through the reservoir (Shi et al., 2013), where the confidence of such links highly correlates with the amount of data involved in the studies. This correlation makes it possible to create predictive models that relate logs to lab-based rock properties, which is incredibly useful. For example, Chang et al. (2006) used sonic travel time and density logs to estimate static Young's modulus away from cored sections. Careful calibration between limited lab measurements and log data enables a better prediction of the geomechanical properties, improving reservoir characterization, injection strategy, and monitoring programs.

Before diving into showcasing the results from the logs, there is a simple workflow that has been established and followed, as seen in the flowchart in Figure 5.18 to carefully analyze the correlations' feasibility at this stage with the current amount of data and decrease the uncertainty in the initial geomechanical parameters' prediction especially that the project wells do not have S-wave velocity logs which limit the elastic moduli calculations from measurements only.

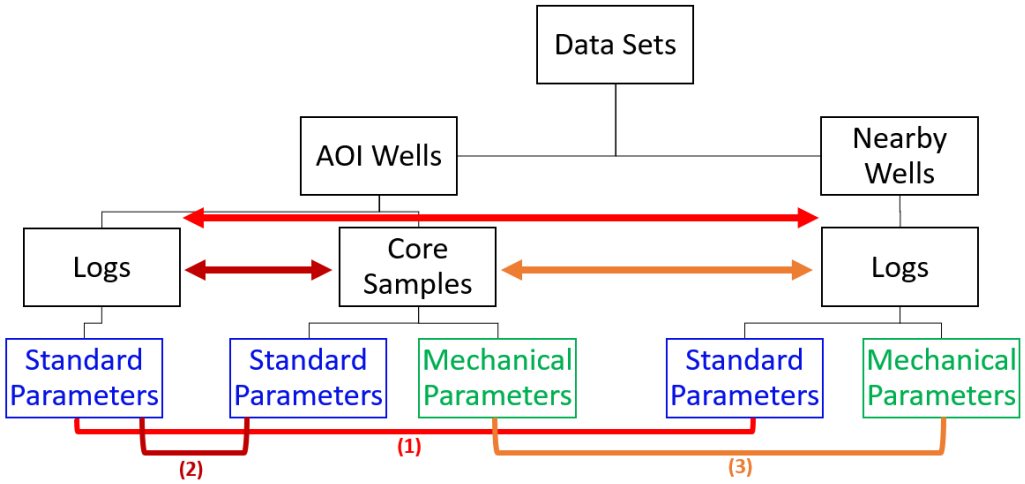

Figure 5.18: Nearby and Area-of-interest (AOI) wells logs, and samples data analysis flowchart

The flowchart seen in Figure 5.18 will start with analyzing the nearby and the AOI wells in terms of their standard logs (P-wave velocity, gamma ray, neutron porosity, bulk density and deep resistivity) separately and then comparing the two results to investigate their correlations in terms of rock parameters as highlighted in red in the workflow. After that, the standard parameters from the AOI logs and lab measurements are also analyzed to investigate the relationship between the two datasets of the same wells, highlighted as the second step in maroon in the flowchart. The third step, as highlighted in orange in the chart, carries the analysis of the geomechanical logs from the nearby wells with the sample's geomechanical data from the AOI wells, which will analyze how much of a correlation there is between them. By the end of the third step of this workflow, all three types of data sets (AOI wells logs, AOI well lab measurements and Nearby wells logs) have been compared and linked to establish an initial evaluation of the data feasibility to proceed with the S-wave velocity estimations and geomechanical log predictions in our AOI wells.
As previously mentioned in the Data Set section, none of the area-of-interest (AOI) wells have S-wave velocity data, which limits the prediction of elastic moduli in those wells. Therefore, the analysis includes nearby wells, focusing on the target formations to predict the S-wave velocity. All nearby wells involved in the study cover only the Slochteren Formation and not the Solling Formation. As a result, the log analysis will mainly focus on the results from the Slochteren Formation wells (K-15 wells) rather than the Solling Formation well (L09-10), where the prediction uncertainty associated with L09-10 well will be high.

Throughout this section, the first few steps will lead us to evaluate how confident we can be of the data, hence the velocity relation from these wells, to predict the AOI wells' S-wave velocity. Then the relation extracted from the nearby wells will be compared to the S-wave prediction results from standard empirical relations. Once all of these steps are done, we will calculate geomechanical parameters logs and correlate them to the lab data.

5.2.1 Nearby Wells and AOI Wells Crossplots - Standard Logs

5.2.1.1 Nearby Wells Crossplots - Standard Logs

I mentioned we have three wells from neighbouring blocks above and below the K15 block for the nearby wells, as seen in figure 3.4 in the Data Set section. Only one well (K12-17) out of the three has all standard logs, but the remaining two have only gamma-ray logs on top of the S-sonic and P-sonic logs.
Figure 5.19 below has several cross plots of the K12-17 well; these were chosen among other cross plots because they show the clearest relations between the parameters we can compare to the AOI wells for our analysis. In the first sub-figure (a), the Vp is plotted against the Neutron porosity log coloured by bulk density, revealing compaction trends and lithology. We can see that higher velocities occur at lower porosities and higher bulk densities. Plot (b) displays the P-wave velocity versus bulk density and is coloured by porosity, providing information on consolidation and stiffness as it also shows a clear positive correlation between the two parameters. Increasing density, hence increasing consolidation, is evident by having higher velocities at higher densities where the rate of increase is dependent on porosity (Mavko et al., 2020). Plot (c) shows the relationship between neutron porosity,

bulk density, and gamma-ray, allowing lithology discrimination based on characteristic porosity-density combinations. In this plot, the trend is clearly negative as the porosity increases and the density decreases, but it is a bit scattered, especially towards higher densities. It appears that the gamma-ray readings are relatively consistent, as the majority of the data points fall within the range of 0 to 30 gAPI. The last plot (d) gives a closer look at the relationship between gamma-ray and density in these sandstone reservoirs, where most of the range of density values all have the same cluster of low gamma-ray values, which indicates clean sand that is filled with probable hydrocarbons indicated by the very low resistivity values. A small portion of the data with higher gamma ray values is concentrated in the higher density values with some higher resistivity values that could indicate more clay content or shale existence within the reservoir.

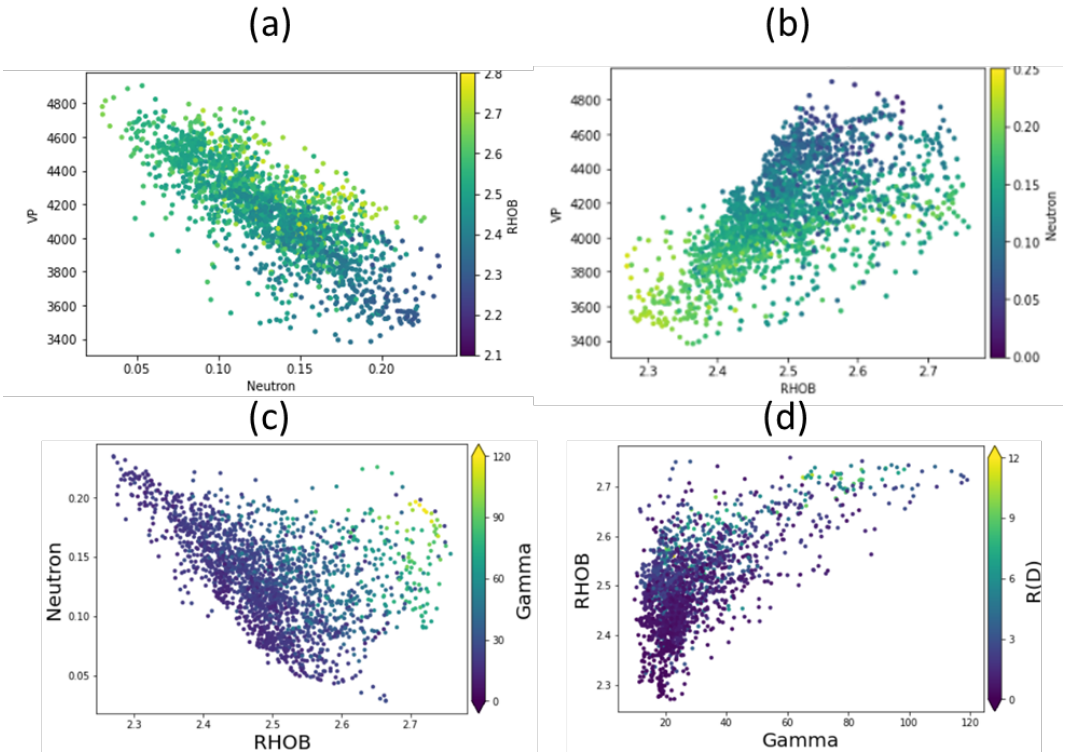

Figure 5.19: Slochteren formation logs of the nearby Well logs: K12-17. (a) P-wave velocity [m/s] vs neutron porosity, coloured by bulk density [g/cm3], (b) P-wave velocity [m/s] vs bulk density, coloured by neutron porosity, (c) neutron density vs bulk density, coloured by gamma-ray [gAPI], (d) bulk density vs gamma ray, coloured by resistivity [ohmm]

5.2.1.2 Area-of-interest (AOI) Wells Crossplots - Standard Logs

The second part nearby-AOI wells correlations is looking at the AOI wells standard logs. This is because I would like to look at the parameters of our wells and their relationship to each other and their value ranges in order to see whether the nearby wells could all be representative of the AOI wells or one of them or none.
Figure 5.20 below shows the same plots discussed in the nearby wells in Figure 5.19 for a consistent comparison. In Figure 5.20, both sub-figures (a) and (b) display the cross plots of the upper Slochteren member wells K15-FG-102 and K15-12, respectively. On the other hand, the bottom row of sub-figures (c) and (d) display the lower Slochteren member wells K15-15A and K15-2 cross plots, respectively.
Looking at the first plot of each sub-figure, which displays P-wave velocity (Vp) vs neutron porosity and is coloured by the bulk density, we can see that all of them follow the same negative correlation with a similar range of Vp, but when it comes to neutron porosity, we can see that the ranges of porosity values are larger in the lower Slochteren wells than the upper Slochteren wells; however, both members fall within the porosity range in the nearby well. As for the second set of plots, Vp is plotted against bulk density and coloured by neutron porosity, where they are all displaying a positive correlation between the two parameters, which also displays a similar correlation to the one found in K12-17 with a similar range of data. The third set of cross plots is the Neutron vs bulk density, and these plots display a negative correlation between the two parameters for all the wells, which is similar to the

result in the K12-17. However, the gamma-ray ranges show that K12-17 have slightly cleaner sand than our AOI wells. The last set of plots is bulk density vs Gamma-ray and is coloured by deep resistivity (No available deep resistivity logs in K15-12, therefore, data is coloured by neutron density). All data sets show similar trends where most of the data have consistently low values of gamma-ray values across the whole bulk density range, indicating a weak correlation between gamma-ray and density parameters in these target zones. Also, in terms of the deep resistivity values, all logs comply with very low values with a similar range found in K12-17 except K15-FG-102, where it has a slightly higher average of resistivity values.

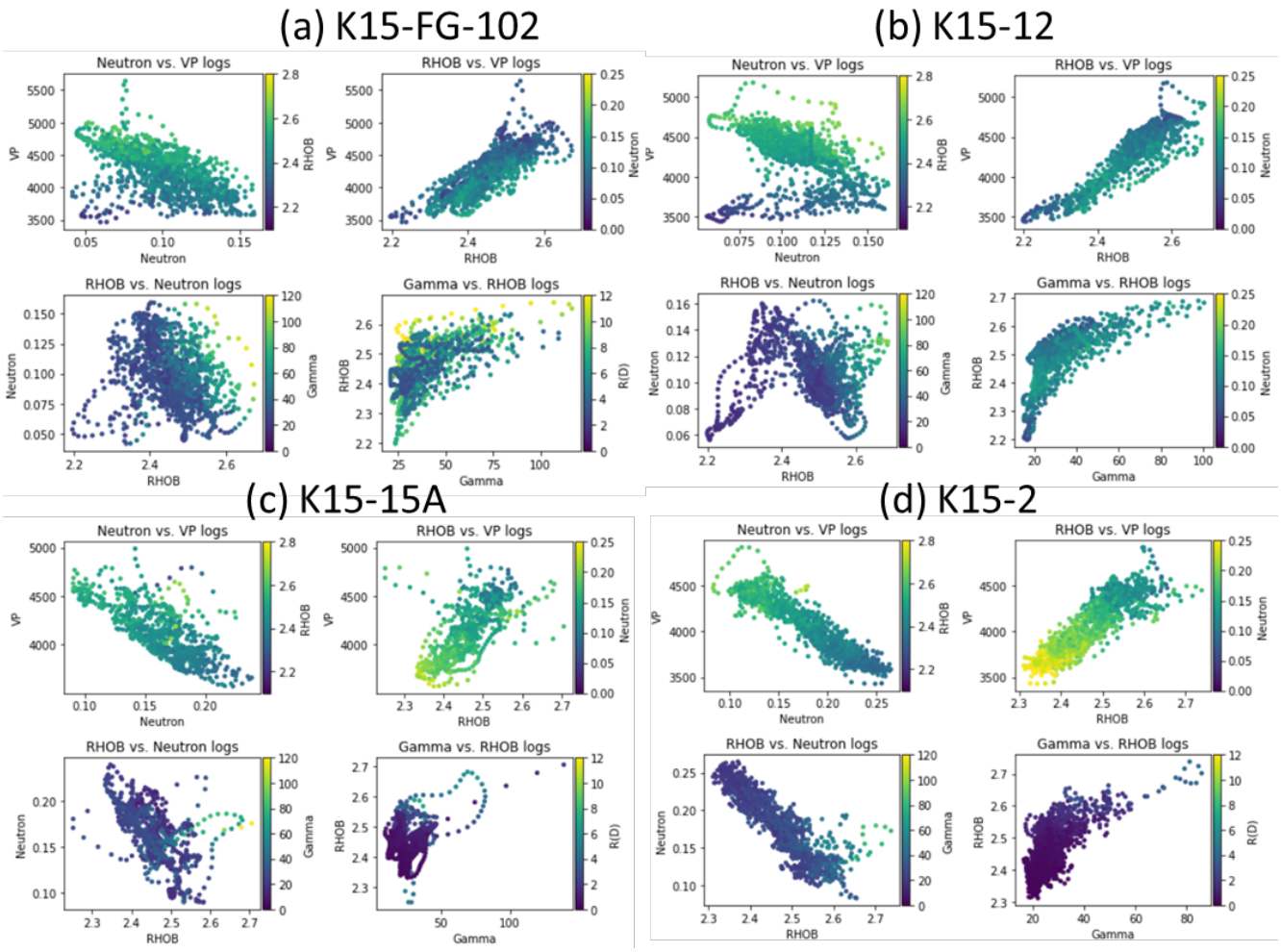

Figure 5.20: Slochteren formation logs of the AOI well logs. (a) K15-FG-102 (Upper Slochteren member) (b) K15-12 (Upper Slochteren member), (c) K15-15A (Lower Slochteren member), (d) K15-12 (Lower Slochteren member). Each subfigure displays these plots (1) P-wave velocity [m/s] vs neutron porosity, coloured by bulk density [g/cm3], (2) P-wave velocity [m/s] vs bulk density, coloured by neutron porosity, (3) neutron density vs bulk density, coloured by gamma-ray [gAPI], (4) bulk density vs gamma ray, coloured by resistivity [ohmm]

Appendix B shows a detailed histogram of all the data distribution and ranges to show the similarities and differences between the log data of all the wells, both AOI wells and nearby wells. The data that has been analyzed in the histograms are P-wave velocity, Gamma Ray, Deep resistivity, bulk density, neutron density and measured depth. By now, the data for the first stage of the log analysis is done by comparing the trends (trendlines for all wells in Appendix D and the range of data values (histograms in Appendix B). From the observations, the well L09-10 targeting the Solling formation has less in common with the logs from the Slochteren formation when it comes to P-wave velocity distribution and ranges that are slightly lower in L09-10, as seen in Figure B.1 in Appendix B, which could be due to the fact that the reservoir is shallower and the bulk density is lower than all the other formations. In L09-10, neutron porosity and bulk density distribution do not match the Slochteren formation wells either, as the porosity has much lower values overall, as well as the density. However, in terms of parameters' relations to one another, it has similar trends as observed in all other wells. On the positive side, all wells in

the AOI from both Slochteren members have similar data distribution and ranges except for the resistivity of the K15-FG-102 wells, it the distribution of the values tends to be higher than others.

Now when comparing the data from the AOI to the nearby wells, it is observed that only K12-17 checks all the boxes, as all the parameters are within the same range of all the AOI wells across those parameters. While the other two wells had sparse parameters, so the comparison was limited to only P-wave velocity and gamma-ray, and both had slightly higher velocity values distribution, but for the gamma-ray, K18-7 had much larger values than all other wells in the Slochteren formation as seen in Appendix B.

5.2.2 AOI Wells Logs and Samples Data Crossplots - Standard Parameters

The upcoming data analysis will concentrate on the AOI wells logs and their core samples. The sample results from 30 and 50 MPa confining pressure cycles are the data used to be compared to the log data for a better reservoir representation. Figure 5.21 below displays standard logs with lab measurements. All sub-figures demonstrate P-wave velocity versus porosity and are coloured by bulk density for each well. The figures display the log data in a cluster of points, while lab measurements are the symbols. The porosity values in the logs are from neutron porosity, while the samples' porosities are from the Pycnometer. Both sample data points and log data points are coloured by their corresponding Bulk density log values and lab-measured values.

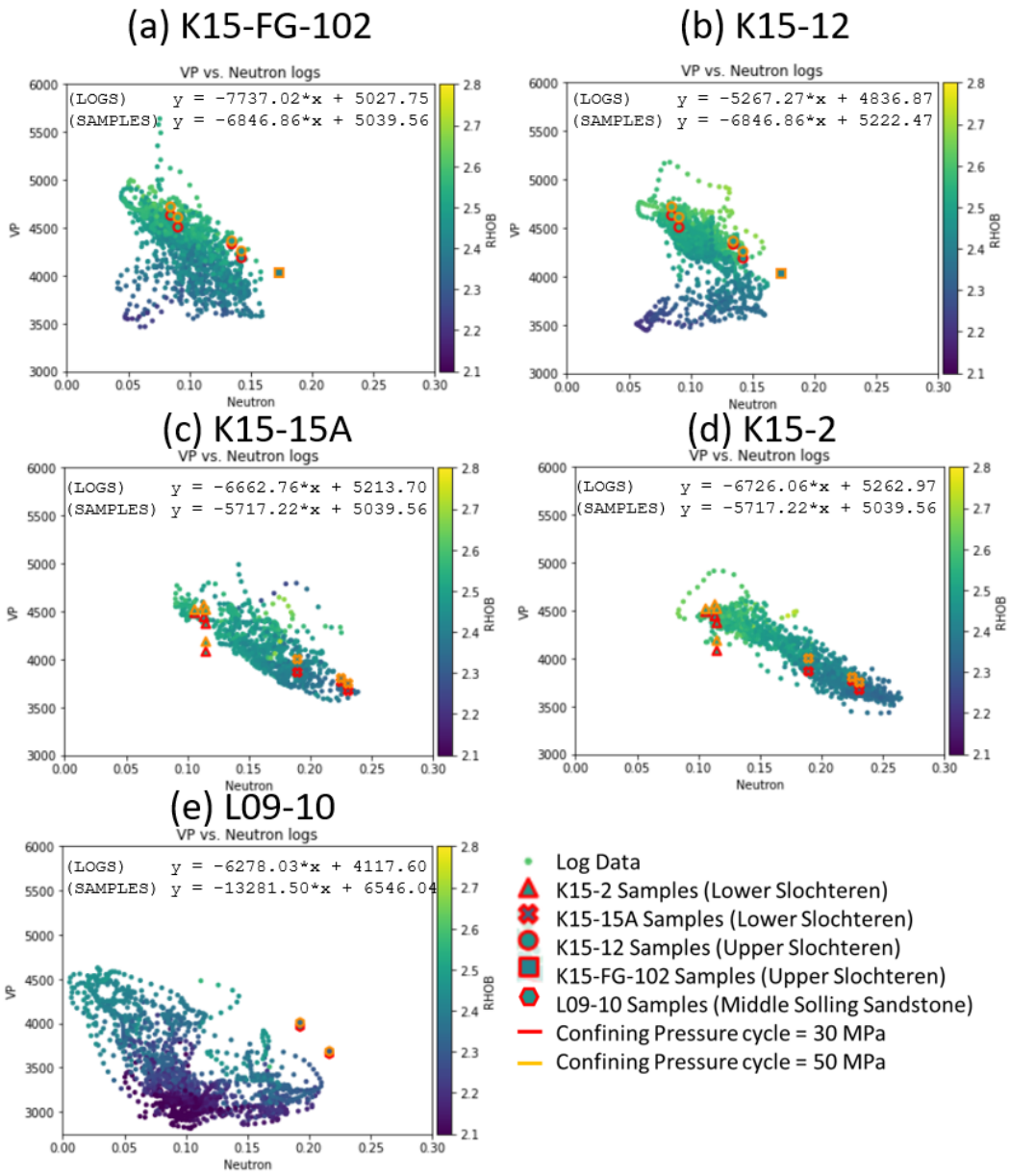

Figure 5.21: Well Logs of AOI with lab test results from samples of the same formation of P-wave velocity [m/s] vs porosity crossplots, coloured by density [g/cm3]. All plots show the equation of the trend-line of both logs and core samples. (a) K15-FG-102 (Upper Slochteren member) (b) K15-12 (Upper Slochteren member), (c) K15-15A (Lower Slochteren member), (d) K15-12 (Lower Slochteren member)

In Figure 5.21 we can see that the measured lab porosity and the measured P-wave velocity of the samples are mostly within the range except the values in L09-10 well as the samples were highly porous that do not represent the majority of the neutron porosity logs. In terms of density values (colour of the data points), we can see that the sample data points are within the range of values from the log data.
The measured data of our samples' porosity, density and P-wave velocity were plotted along the well log data retrieved from NLOG of the same wells and similarities were observed. However, here I would like to quantify the relationship between them as Figure 5.22 below crossplots these parameters in order to determine their correlation coefficient and percentage difference value of each sample. The uncertainty analysis was done over the samples overall and each reservoir; The Upper Slochteren member, the Lower Slochteren member and the Middle Solling Sandstone member. The ideal situation is that all the regression lines of data match the best-fit line (red in all the subfigures), where both values from the logs and the lab measurements are the same.

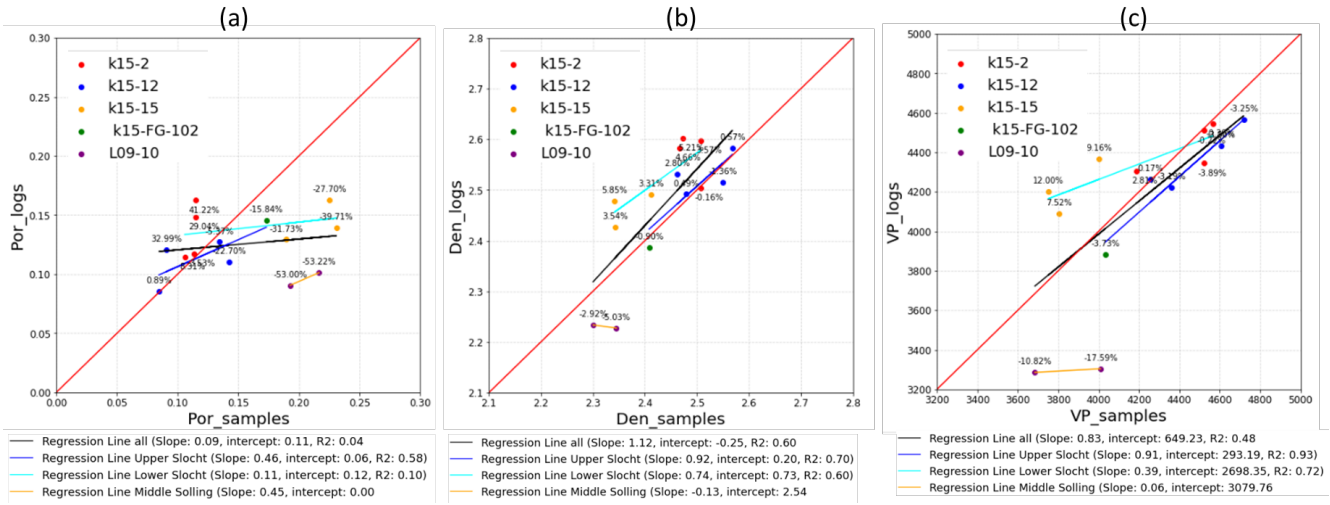

Figure 5.22: Data comparison between log data and lab measurements for all AOI wells at the same measured depth. (a) Neutron Porosity log values vs. Pycnometer porosity [-], (b) Bulk Density log values vs Samples density [g/cm3], (c) P-wave velocity log values vs Samples P-wave velocity [m/s]

Looking at the porosity data in subfigure (a), we can see low values of the correlation coefficient between the two datasets (neutron porosity for the logs and pycnometer porosity from the lab measurements). This alarms the potential built-up effect on the predicted elastic parameter values indirectly due to lithology; as we have discussed earlier, there is a strong, clear correlation between the different Elastic moduli and the porosity. On the bright side, in subfigures (b) and (c) for density and P-wave velocity, respectively, the correlation coefficient is mostly higher than 0.6, and even higher than 0.7 for the Upper Slochteren wells, which indicates a better relatively good correlation between the two datasets, logs and lab measurements.

5.2.3 Nearby Wells Logs and Samples Data Crossplots - Geomechanical Parameters

Earlier, from the nearby wells' log data analysis, it was observed that the lithology of K12-17 represents the Slochteren formation in the AOI wells in terms of data trends and data distribution. The AOI wells and core data showed that the lab-measured values also have the same range and data distribution as their corresponding well logs. Therefore, now we know that the lab measurements from P-wave velocity, porosity and density fall within the same range as the nearby well K12-17, which lets us proceed with the third step of the workflow in 5.18 that is calculating the geomechanical parameters from the nearby well and displaying these geomechanical logs against the geomechanical data calculated from the lab experiments.
In Figure 5.23 below, four different sub-figures display different geomechanical properties.

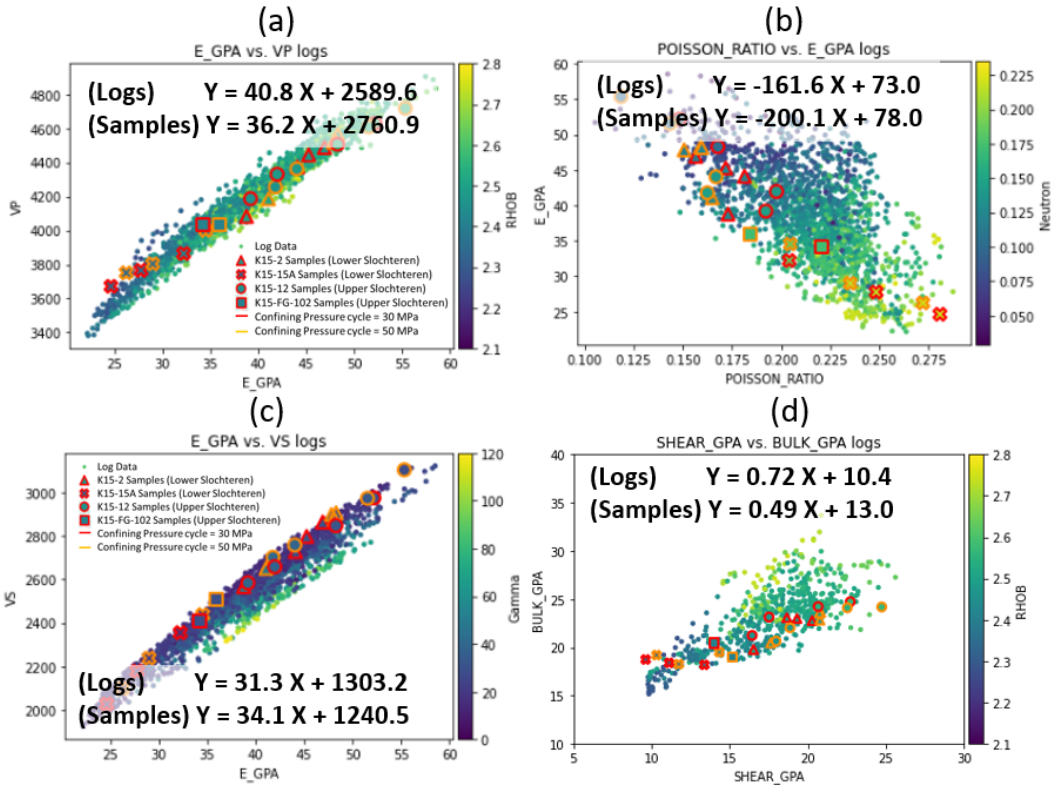

Figure 5.23: Geomechanical data cross plots of the Slochteren formation of K12-17 with geomechanical data from the lab samples. All plots show the equation of the trend-line of both logs and core samples. (a) P-wave velocity [m/s] vs Dynamic Young's modulus [GPa], coloured by density. (b) Dynamic Young's modulus [GPa] vs Poisson Ratio [-], coloured by porosity values. (c) S-wave velocity [m/s] vs Dynamic Young's modulus [GPa], coloured by Gamma-ray. (d) Bulk modulus [GPa] vs Shear modulus [GPa], coloured by density

Looking at all the sub-figures in figure 5.23, we can see that the data points from the samples and the logs have compatible trendlines especially for subfigures 5.18 (a) and (b) showing how well the dynamic young's modulus correlates with velocities while maintaining similar trends. The subfigures 5.18 (b) and (c), especially (c), we can observe some discrepancies, which could be due to the fact that parameters like Poisson Ratio and Bulk modulus are more affected by differences in factors like porosity seen in Figure 5.22. In terms of the data ranges, the sample data points fall within the same range of log values, which gives us one step further in validating the correlation between these two data points and the geomechanical logs to be calculated for our AOI logs.

5.2.4 S-wave Velocity Prediction for AOI Wells

Academics and industry pursue S-wave prediction because S-waves reveal key rock attributes like elasticity, Poisson's ratio, and shear stiffness that P-waves do not (Dutta et al., 2007). This makes S-velocities critical for geomechanical modelling and reservoir monitoring.
In this section, two methods of prediction will be tested; using relations calculated from Vp and Vs values from nearby wells (K12-17) and using standard empirical and theoretical relations from literature as they use correlations between S-wave and P-wave velocities established through lab tests on core samples and petrophysical analysis for a large set of data. Both approaches enable initial S-wave evaluation for geomechanical properties when direct measurements are unavailable (Dutta et al., 2007; Prasad & Kuzmina, 2021). However, S-prediction from the wells could have advantages over empirical and theoretical relations in honouring well geology and delivering quantitative uncertainty. This methodology relies on having sufficient well control that properly reflects the geology of the area and the variations of the lithology of the target formation. On the other hand, empirical relations are faster but suffer from much higher uncertainty without the integration of geological knowledge.

5.2.4.1 Nearby Wells S-wave Velocity Estimation

The previous analysis of the nearby well data has shown that the logs of the nearby well K12-17 have the most representative data sets when comparing lithology. This section will discuss the Vp and Vs calculated relations from it for the Slochteren formation data.

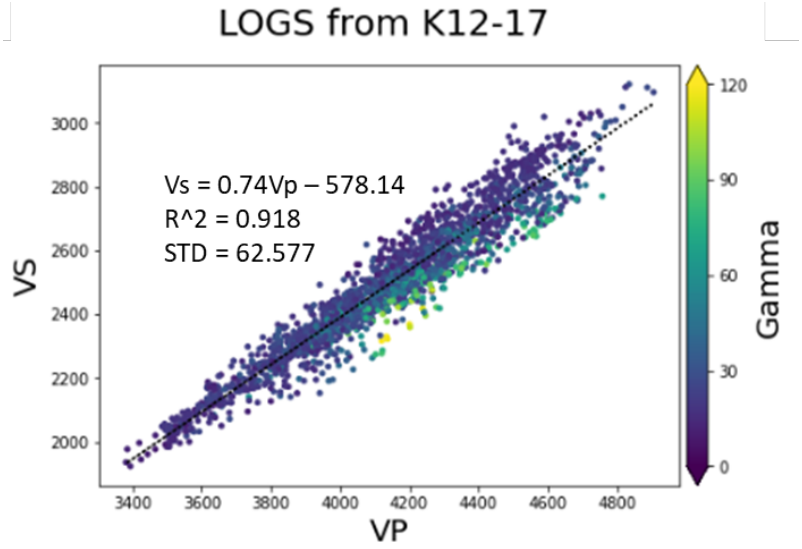

Figure 5.24: P-wave velocity vs P-wave velocity [m/s] plot, coloured by gamma-ray value with a linear regression line in black and the equation of the line, the standard deviation and the R-2 value

Figure 5.24 above displays a crossplot between the S-wave and P-wave velocities. As a first pass for data analysis and simplification purposes, we extracted a linear relation between the two parameters from the figure, as seen here in equation 5.12, where the units are in [m/s].

$$V_S = 0.74V_P - 578.14 \tag{5.12}$$

This equation has a high R-squared value of 0.918 with a standard deviation value of 62.577.

5.2.4.2 Empirical Relations S-wave Velocity Estimation

Empirical correlations provide a straightforward way to estimate seismic velocities from well logs without shear sonic data. These equations establish mathematical relationships between velocities and commonly measured properties like porosity and density. Many researchers have derived Vp-Vs correlations from laboratory measurements on core plugs or theoretical relations based on a large dataset of well-log data with specific lithologies. Castagna et al. (1985) published a linear relationship between P-wave and S-wave velocities established from tests on various consolidated sandstones, including Berea and Wilcox. Krief et al. (1990) developed a theoretical relation of different lithologies from an extensive dataset of well logs, including sandstones, water-bearing and gas bearing and consolidated and unconsolidated sands. Brocher (2005) proposed a polynomial Vp-Vs equation derived from diverse sedimentary rocks covering various lithologies and porosities. Han et al. (1986) determined a correlation specifically for consolidated sandstones across a range of porosities. While they are easy to apply, a limitation is that empirical and theoretical relations from the literature give average velocity trends lacking resolution and are not geology-specific. However, they enable initial analysis when direct S-sonic data is unavailable and provide quick first-pass velocity estimation through simple log calculations.
The above relations are selected because they were extracted from similar lithologies as the sandstone reservoirs here in Slochteren and Solling sandstone members. First is the Castanga empirical equation, which is stated below in equation 5.13 with velocities in [km/s] as their unit.

$$V_S = 0.862V_P - 1.172 \tag{5.13}$$

The Brocher equation is also used in this phase of the study. This relation was derived from a collection of Vp and Vs measurements in various sedimentary rocks. It is intended to apply to a wide range of lithologies. Brocher

states this relation can be used for Vp values ranging from 1.5 to 8 km/s where our data is within that range. He analyzed data from multiple sources, including sedimentary rocks like sandstone, shale, limestone and dolomite across various porosities. Brocher equation (5.14) is shown below, where Vp and Vs are in [km/s].

$$V_S = 0.7858 - 1.2344V_P + 0.7949V_P^2 - 0.1238V_P^3 + 0.0064V_P^4 \tag{5.14}$$

The third equation included in the study is the Krief (1990) theoretical relation that determined the relationship between the square of velocities of a large dataset of sandstone logs. Here is the equation (equation 5.15) where the velocities are in [km/s]:

$$V_S^2 = 0.452V_P^2 - 1.74 \tag{5.15}$$

The last equation used was the Han empirical equation. Han et al. analyzed compressional and shear wave velocity data from sandstone cores with porosities ranging from 2% to 25%. The samples were from various locations of sandstone. They found shear wave velocity depended primarily on porosity, with some additional dependence on clay content. The equation above provides the correlation of Vs with Vp that they determined based on the consolidated sandstone datasets. Here is Han equation 5.16 below where velocities are in [km/s].

$$V_S = 0.794 * V_P - 0.787 \tag{5.16}$$

To view the results of the relations from the literature, we plotted the Vs versus Vp crossplots for all nearby wells that have the measurements of both and displayed all the empirical relations on each plot as a form of quality check to see which of the equations represents the lithology of the wells seen in Figure 5.25. Well K12-17 in sub-figure (a) is the closest of the three nearby wells to the wells in the AOI for the Slochteren formation. So, from comparing the empirical relations against its data in Figure 5.25, we can see that the most representative equations and the closest to our data are Brocher and Krief. However, the equation of the line of the two other wells in the Slochteren formation have relatively different values than K12-17; therefore, the empirical equations did not predict the Vs from Vp in these two wells as well as K12-17. It is important to note that these two wells have different Vs-Vp relations than K12-17 due to the difference in lithology, especially in K18-7. This leads us to focus mainly on the results of the alignment between empirical relations and K17-12 and K18-8 wells.

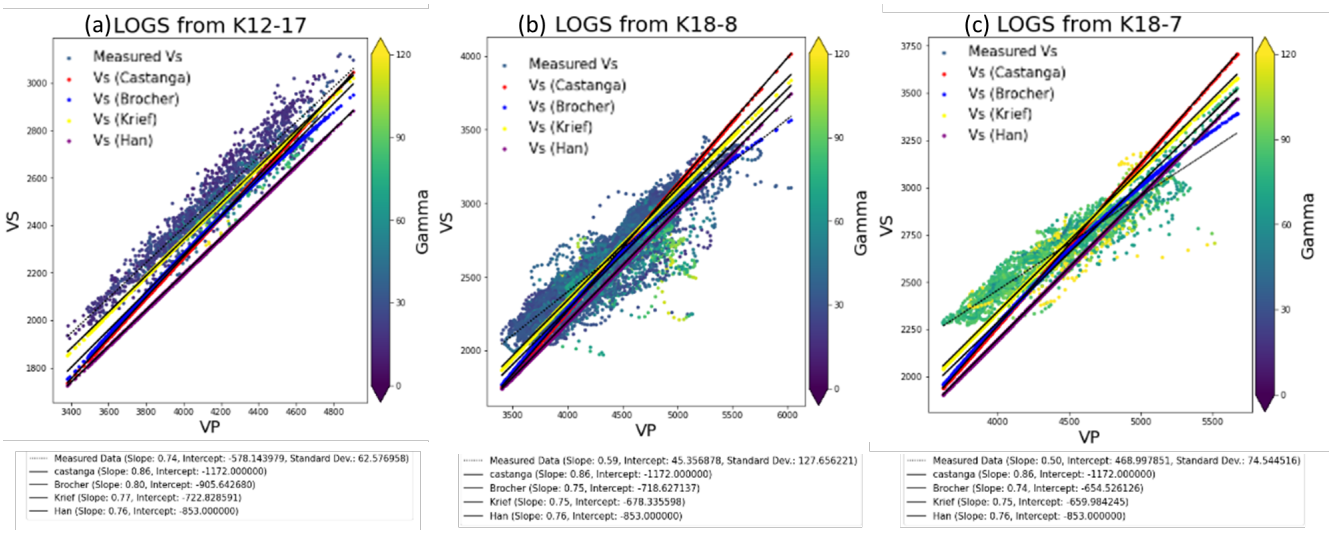

Figure 5.25: P-wave velocity vs P-wave velocity [m/s] plots, coloured by gamma-ray value with a linear regression line in black and the equation of the line, and results of the other four empirical equations and theoretical relations from the literature of the nearby wells. (a) K12-17, (b) K18-8, (c) K18-7

Many other versions of empirical relations on shear-wave velocity estimation for different areas and lithologies exist. These empirical formulas are generally not accurate enough to meet the preciseness requirement for shear-wave prediction. Therefore, the locally extracted shear-wave estimation can better describe the complex formation structure. That being said, in order to proceed with the elastic moduli prediction, three of the S-wave velocity estimation equations will be used, the nearby well K12-17 relation, Krief relation and Brocher relation and all will be compared to the S-wave velocity prediction from our Vs-Vp relation from our lab measurement.

5.2.4.3 S-wave velocity uncertainty analysis

It has been established that not all three nearby wells are good representatives of the lithology of the target reservoirs. There have been three limitations in these comparisons; all nearby wells have data on the Slochteren Formation, but none of them covers the Solling Formation. The second limitation is that only one of the three wells has all logs available, which was K12-17 well, which limited the lithology description and parameters analysis to observe the well/s properly. One last limitation was the insufficient number of wells that were used to create the velocity relation from the nearby wells, which was limited to only one well. However, the K12-17 well lithology was a very good representation of the lithology of all four Slochteren formations well, but unfortunately, it was not a good match for the L09-10 that covers the Solling formation.
The other method of estimation was using relations from the literature, as discussed earlier, where four different relations were derived empirically or theoretically from sandstone rocks used in the project, Castanga, Brocher, Krief and Han. In the analysis from figure 5.25 on which empirical relation among the four to proceed within this project, Krief and Brocher ended up being the top two which gave the closest relation between P-wave velocity and S-wave velocity to the real measurements from the logs of all nearby wells; K12-17, K18-8 and K18-7.
Figure 5.26 below shows cross plots of the predicted S-wave velocity from all methods versus the measured S-wave velocity in all nearby wells where the best-fitted line of the data sets in black as a reference for all wells. In terms of comparing the correlation coefficient in all the wells for the empirical relations, we can see that all the relations have a high value where all of the values are above 0.8; however, when adding the slopes to the comparison comparing, we can see that overall, the predicted values from the K12-17 relation have the best estimation. Although K12-17 has the highest correlation coefficient overall, there is a tight competition between the correlation coefficient values between all the relations. Therefore, the comparison included the equation of the line, which also confirms the earlier findings that the top two empirical relations for the best predictions were Brocher and Krief.

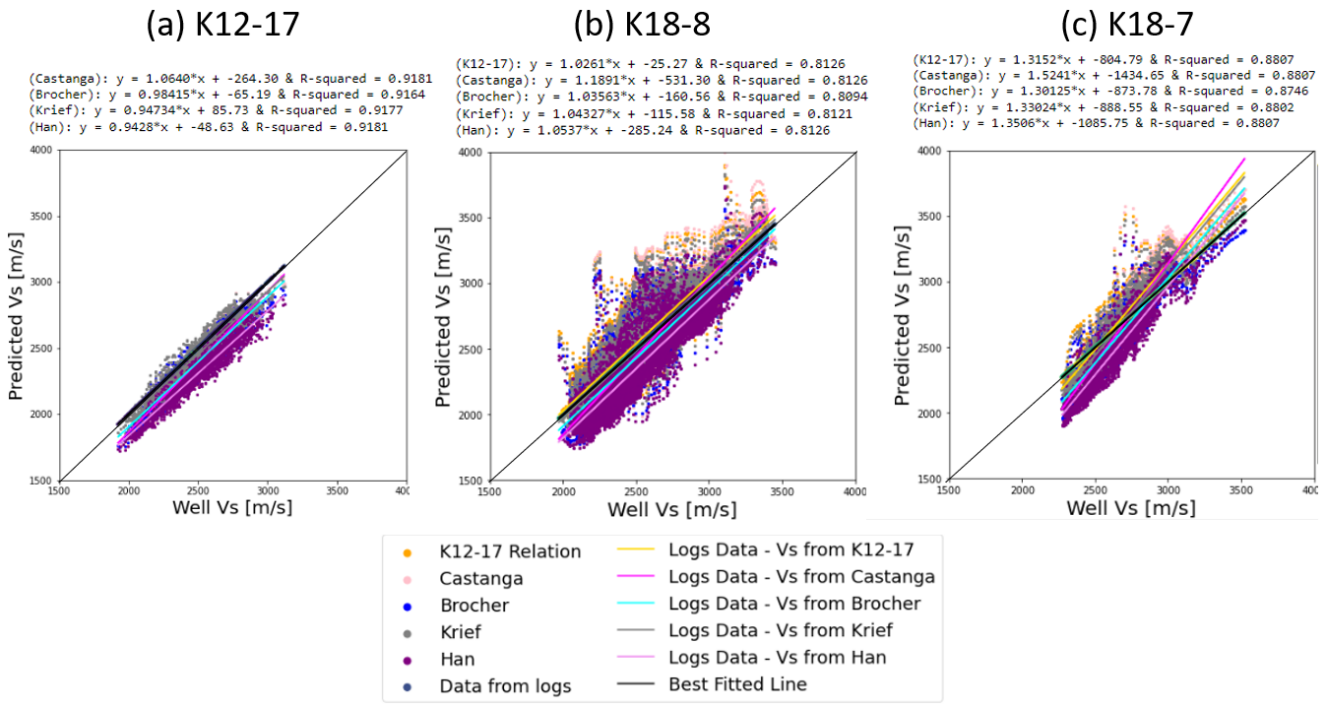

Figure 5.26: Predicted S-wave Velocity vs Measured S-wave Velocity for nearby wells of the Slochteren formation.

These equations are used as a first pass in the initial stages, but as the studies further develop and more field and samples data are involved, always go for the local and preferably more than one well to estimate the location while keeping in mind that the lithology is representative in order to avoid any huge mismatches in the predictions. There is very high uncertainty in using these relations to estimate the S-wave velocity for the wells due to the lack of S-wave velocity data. In order to get the best results, we need to have a sufficient number of offset wells of the same target zone representing the lithology that we are doing in order to get the most accurate geomechanical analysis, hence building a model with less uncertainty.

5.3 Predicted Elastic Moduli logs for AOI Wells

This last section of the results will display the well logs of multiple geomechanical parameters resulting from the estimated S-wave velocity from the nearby well (K12-17) and Brocher and Krief relations. The geomechanical parameter values of the measured samples are also depicted on the predicted well logs to visualize whether the logs follow similar values as the parameters measured from the lab samples.

In Figure 5.27 below, the best matches between the lab measurements and the log predictions are observed in Dynamic Young's modulus results, where most of the lab measurements are on the log data and follow their trends as well, especially the predicted log from the nearby well (K12-17). It is mostly observed in the well with most samples K15-12 found in subfigure 5.27 (a), where we can observe that the data sample values decrease and increase along the variations observed in the log signature. Looking into the second parameter, the Bulk Modulus, we can also see that the data points are within the range values from the logs; however, the lower Slochteren logs (K15-2 and K15-15) have fewer matches than the Upper Slochteren well logs. The last parameter to analyze its results is the Poisson Ration, where generally compared to the good matches in values in the other two parameters, this parameter has the least correlation to the log prediction.

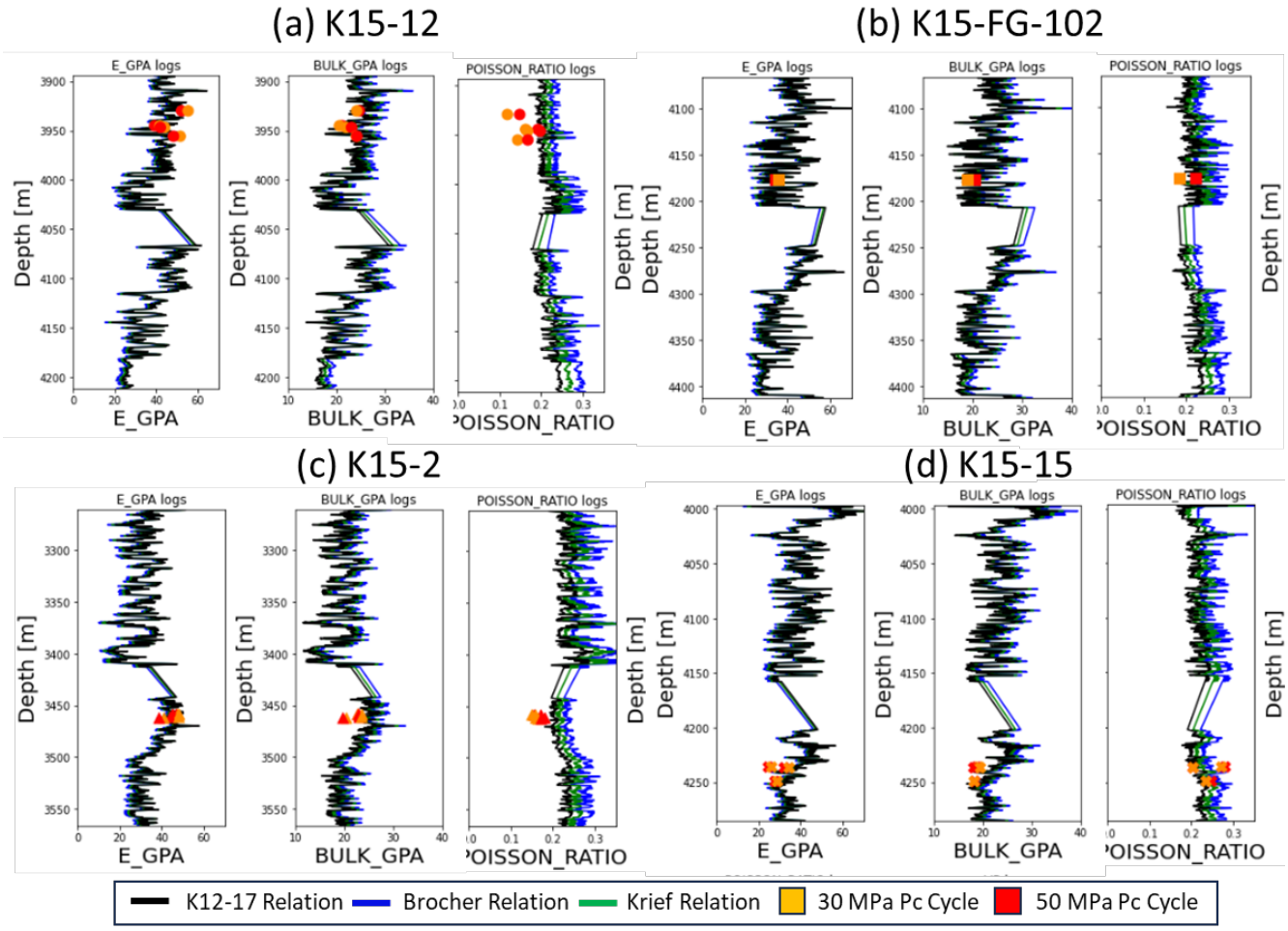

Figure 5.27: Measured Depth vs Predicted (Dynamic Young's Modulus, Bulk Modulus and Poisson Ratio) for the Slochteren formation displayed with the calculated values of the cored samples of each well of 30 MPa Pc cycle (orange) and 50 MPa Pc cycle (red). (a) K15-12, (b) K15-FG-102, (c) K15-2, (d) K15-15A

A more comprehensive understanding can be done by expanding the comparison between predicted mechanical logs and sample data. This is done by the juxtaposition of the relations derived directly from the lab measurement seen in equation 5.4 with the relation inferred from the nearby well (K12-17) seen in equation 5.12.

Figure 5.28 below shows the predicted logs from the two relations; lab-derived in blue and log-derived in black for all Slochteren wells. It appears that the predictions show that there is an agreement between two methods for Dynamic Young's modulus (Ed) and Bulk modulus (K) which suggests that the two datasets are validating each

other and increasing confidence in the two relations. The similar values imply that the physics controlling the elastic behaviour is consistent between the lab samples and the subsurface. However, the discrepancy seen in the third predicted log, the Poisson Ratio, should be noted where the lab-derived predicted log has lower values than the log-derived. These differences between the results of the elastic moduli could indicate Poisson Ratio is more sensitive to the differences in factors like porosity and density between lab and logs.

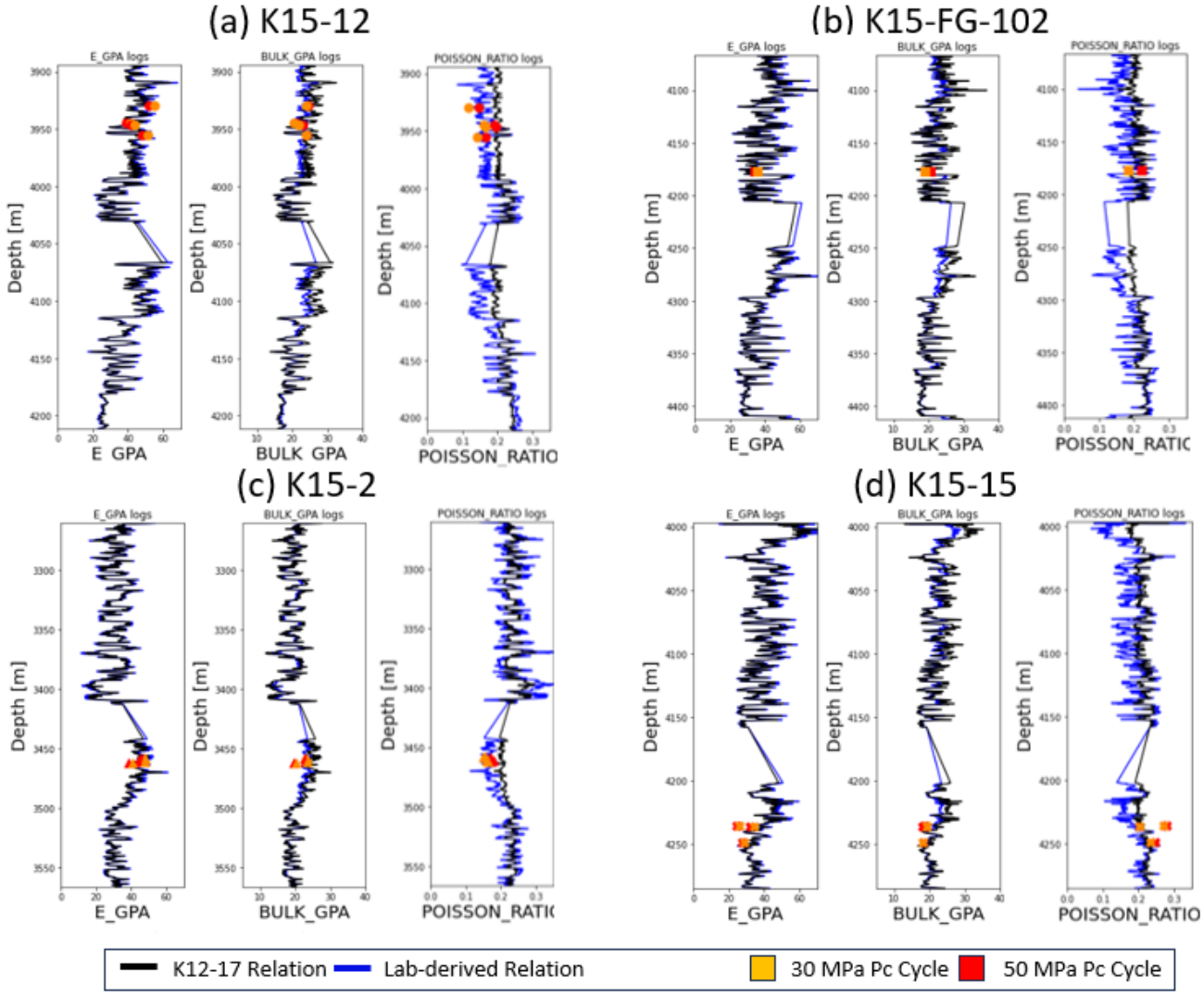

Figure 5.28: Measured Depth vs Predicted (Dynamic Young's Modulus, Bulk Modulus and Poisson Ratio) for the Slochteren formation displayed with the calculated values of the cored samples of each well of 30 MPa Pc cycle (orange) and 50 MPa Pc cycle (red). (a) K15-12, (b) K15-FG-102, (c) K15-2, (d) K15-15A

Predicted Elastic Moduli Uncertainty Analysis

Comparing the two dynamic sets helps validate and calibrate log-based predictions to core data measured under controlled conditions. This can remove systematic biases in log predictions.
Previously, the alignments between the predictions and the lab measurement data points were established, but to quality check the data on a small scale, I will be quantifying the match between predicted log-based dynamic moduli and lab-derived dynamic moduli as seen in Figure 5.29 below. This sheds light on the underlying physics' effect on field-scale versus lab-scale rock properties. This guides the proper interpretation of log-based elastic moduli estimates for seismic and reservoir modelling.

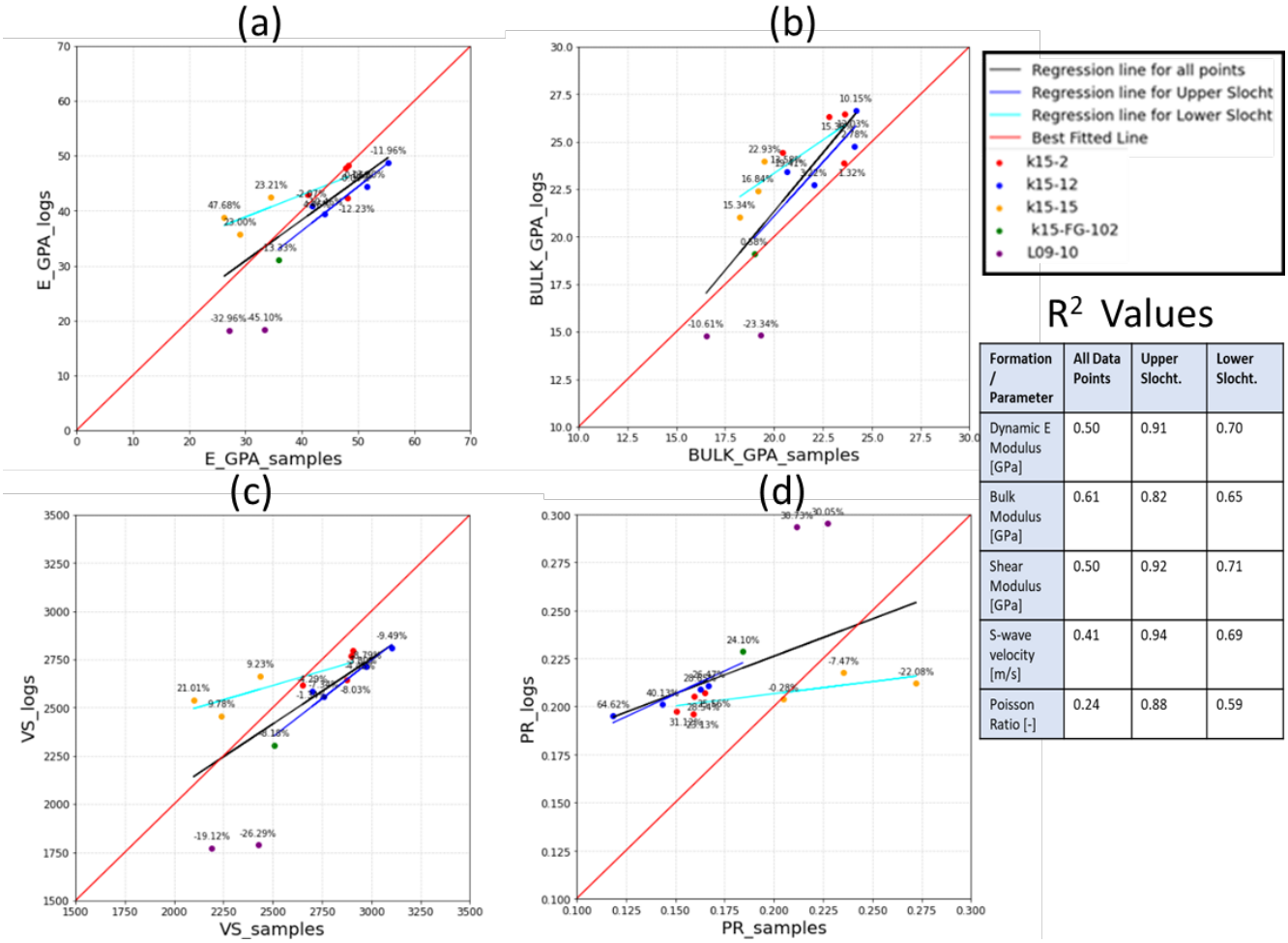

R^2 Values

Formation / Parameter	All Data Points	Upper Slocht.	Lower Slocht.
Dynamic E Modulus [GPa]	0.50	0.91	0.70
Bulk Modulus [GPa]	0.61	0.82	0.65
Shear Modulus [GPa]	0.50	0.92	0.71
S-wave velocity [m/s]	0.41	0.94	0.69
Poisson Ratio [-]	0.24	0.88	0.59

Figure 5.29: Predicted Elastic Parameters (using K12-17 velocity correlation) vs Lab-derived measurements displaying the linear regression line for all data points, the Upper Slochteren data points only and the Lower Slochteren data points only with the correlation coefficient and the percentage difference of each data point. (a) Dynamic Young's Modulus [GPa], (b) Bulk Modulus [GPA], S-wave Velocity [m/s], Poisson Ratio [m/s]

The correlation coefficient has relatively low values when analyzing the data points as a whole, especially for the Poisson Ratio. This could be directly related to the low lithology correlation observed earlier between the Slochteren formation and the Solling formation samples and log data which was reflected in the prediction results of L09-10. However, when looking at the data points from the upper and lower members of the Slochteren formation, we can see that the correlation coefficient jumps high to around 0.9 for the Upper Slochteren member data points and around 0.7 for the lower Slochteren. In Appendix E, Figure E.2 displays a blind test of K12-17 that has a measured S-wave velocity. The Figure shows multiple predicted elastic moduli logs resulting from the lab-derived relation, alongside the measured logs of the K12-17 well. That comparison boosts confidence because of the alignment of the predicted logs and the high correlation coefficient from the crossplots of the predicted Dynamic Young's modulus versus the measured data.

Overall, the confidence in predicting the elastic moduli of the Slochteren formations is much higher than using these relations to predict them for the Solling formation. However, the confidence is very low for Poisson ratio prediction as the percentage difference of the data points seen in subfigure (d) is high for most of the data points, in addition to the low correlation coefficient.

6 Discussion and Engineering Implications

The experimental results and analysis provide valuable insights into the geomechanical behaviour and acoustic properties of both Slochteren and Solling sandstone formations. While my study was limited to 17 core samples from five wells and their corresponding well logs, the data still offer useful parameter values, parameter correlations, and extracted empirical relations to form an important basis for understanding the complexities of the formations and guide further geomechanical characterization of the site.

The thesis has analyzed four main categories: lab measurements, lab-derived relations, log-derived relations, and elastic parameter predictions. Multiple methods were employed - laboratory core tests provided direct static and dynamic moduli measurements on samples, and well logs enabled dynamic moduli prediction through empirical correlations extracted from the lab, nearby wells, and published literature. These predictions were analysed via cross-plots that helped evaluate the agreement level and uncertainties between these techniques.

From the lab measurements, a central finding was the variability exhibited in elastic moduli and wave velocities that are linked to differences in mainly porosity and density between the samples. This agrees with the established relationships between higher stiffness and higher density/lower porosity by Mavako et al. (2020), which indicates that the moduli reflect porosity and compaction trends. At the same time, visible differences in lithology and depositional facies existed between the samples in the sample description table (table 3.1), but elastic moduli did not correlate with the facies when analyzing Figures 5.9 and 5.12. Table 6.1 below summarizes the lab-derived elastic moduli value ranges of both dynamic and static, from mainly the 30 and 50 MPa confining pressure cycles. The colours of the table indicate the porosity categories; low, medium and high for a range of 8-23%. This highlights that these changes in porosities directly affect the measured velocities and elastic moduli. As an example, when looking at the values from the 50 MPa confining pressure cycles, the porosity variability causes a large range of Static Young's modulus values (17-33 GPa), Dynamic Young's modulus (26-55 GPa), Poisson Ratio (0.27-0.12), and all other elastic moduli seen in table 6.1. These moduli ranges provide expected values for these reservoirs, where they align with the range reported by Han (1986), as the static Young's moduli range was 20-35 GPa and Poisson's rations of 0.15-0.33 for consolidated sandstones at 40 MPa confining pressure. Also, the range of Bulk modulus in our data is 16 to 25 GPa, similar to the expected range under pressure of 35 MPa in Liu et al. (2021) 19-30 GPa and Han (1986) 14-25 GPa at 40 MPa confining pressure. These literature comparisons were extensively analyzed in 5.1.2.2. This agreement with literature studies helps validate the measurements. These variations in dependencies between lithology and elastic moduli highlight the inherent heterogeneity within these reservoir formations that must be incorporated into geomechanical models, recognizing that they reflect the real-world complexity of the geology of the subsurface.

		Lithology Data		Mechanical Data							
Formation/ Member	Sample Name	Pycnometer Porosity	Density [g/cm3]	Static E [GPa]	Vp [m/s]	Vs [m/s]	Vp/Vs	Dynamic E [GPa]	Bulk Modulus [GPa]	Poisson Ratio	Shear Modulus [GPa]
Upper Slochteren	K15-12-1V	0.08	2.57	20 - 27	4629 - 4718	2975 - 3104	1.56 - 1.52	52 - 55	25 - 24	0.15 - 0.12	23 - 25
	K15-12-21V	0.09	2.55	19 - 26	4506 - 4608	2847 - 2973	1.58 - 1.55	48 - 52	24 - 24	0.17 - 0.14	21 - 23
	K15-12-14V	0.13	2.48	18 - 24	4330 - 4362	2658 - 2759	1.63 - 1.58	42 - 44	23 - 22	0.20 - 0.17	18 - 19
	K15-12-12V	0.14	2.46	18 - 25	4187 - 4256	2584 - 2702	1.62 - 1.58	39 - 42	21 - 21	0.19 - 0.16	16 - 18
	K15-FG-102-4V	0.17	2.41	14 - 18	4030 - 4033	2412 - 2508	1.67 - 1.61	34 - 36	20 - 19	0.22 - 0.18	14 - 15
Lower Slochteren	K15-2-3V	0.11	2.47	21 - 26	4488 - 4520	2864 - 2899	1.57 - 1.56	47 - 48	23 - 23	0.16 - 0.15	20 - 21
	K15-2-4V	0.11	2.47	24 - 33	4444 - 4565	2798 - 2906	1.59 - 1.57	45 - 48	23 - 24	0.17 - 0.16	19 - 21
	K15-2-5V	0.12	2.51	21 - 29	4373 - 4520	2728 - 2877	1.60 - 1.57	44 - 48	23 - 24	0.18 - 0.16	19 - 21
	K15-2-7V	0.12	2.51	18 - 24	4082 - 4186	2567 - 2651	1.59 - 1.58	39 - 41	20 - 20	0.17 - 0.16	17 - 18
	K15-15-6V	0.19	2.41	15 - 21	3864 - 4001	2355 - 2438	1.64 - 1.64	32 - 35	18 - 19	0.20 - 0.20	13 - 14
	K15-15-13V	0.23	2.34	12 - 17	3765 - 3804	2178 - 2238	1.73 - 1.70	28 - 29	18 - 18	0.25 - 0.24	11 - 12
	K15-15-4V	0.23	2.34	10 - 18	3671 - 3751	2027 - 2098	1.81 - 1.79	25 - 26	19 - 19	0.28 - 0.27	10 - 10
Middle Solling	L09-10-5VB	0.19	2.35	13 - 21	3962 - 4009	2364 - 2425	1.68 - 1.65	32 - 33	19 - 19	0.22 - 0.21	13 - 14
	L09-10-6VA	0.22	2.30	12 - 19	3655 - 3685	2153 - 2189	1.70 - 1.68	26 - 27	17 - 17	0.23 - 0.23	11 - 11

Low Porosity
Medium Porosity
High Porosity

Figure 6.1: Summary of the lab measurements ranging from 30 to 50 MPa confining pressure cycles, which is the range that represents the target reservoirs

The lab measurements established several correlations between elastic properties, porosity and sonic velocities that can be utilized to estimate geomechanical parameters away from the cored intervals using logs. The first correlation

established was to estimate elastic moduli (Dynamic Young's modulus, bulk modulus and shear modulus) with respect to confining pressure and porosity in equation 5.5 for the dynamic Young's modulus, equation 5.6 for the Bulk modulus, and equation 5.7 for the Shear modulus. The strong correlation between the predicted values and the measured values in these equations (R2>0.8) increases the confidence in the applicability of this relation for modelling as the first pass. The moduli variations with confining pressure also follow expected trends as microcracks close under stress (Sharma and Tutuncu, 2016). Also, the non-linear velocity-pressure relation, steep initially but gradual at higher pressures, matches the observations by Asef et al. (2013), which is linked to the microcracks closure affecting the velocity changes. That being said, further calibration to more samples and using a better-fit model like a polynomial can refine this relation and enhance the quality of the prediction.
Another key relation extracted from the lab measurement is the relationship of Static and Dynamic Young's modulus in equations 5.8 and 5.9 for the 30, 50 MPa cycles that provide initial predictive capability from estimating static moduli from log-derived dynamic young's moduli. These predictive equations had high correlations (R2>0.8); however, the results did not fully align with established equations from the literature, and the relationship obtained from our data had lower ratios than McCann and Eissa's equations (discussed in Figure B.6). This could indicate that our samples had more microcracks influence state by McCann and Entwisle paper which suggests greater sensitivity to strain rate and loading frequency. This divergence from my experimental correlation suggests more samples are needed to refine this reservoir-specific relationship.

one more important result is the ability to predict shear wave velocity in cases where direct S-wave measurements are unavailable, which limits the elastic parameters log prediction. The methods I employed included extracting an empirical equation with respect to primary wave velocity from the acoustic lab measurements in equation 5.4. Another method was extracting Vs-Vp correlations from offset wells that have Vs measurements, as seen in the equation 5.12. The last method was applying standard empirical formulas (Castanga, Brocher, Krief and Han) to estimate the initial S-wave velocity and analyzed in section 5.2.4. This methodological workflow is created and followed to enable preliminary geomechanical analysis. The uncertainty without a direct log measurement of the S-wave data is acknowledged, but this approach offers a workflow for obtaining a first-pass S-wave velocity evaluation to ensure the feasibility of the current data and methods used to calculate the S-wave velocity, hence a decrease in the uncertainty in the resulting elastic moduli prediction seen in figures 5.27 and 5.28.

The results and analysis show that laboratory data delivered core-scale ground truth but can suffer stress relief effects. Log predictions estimate in-situ values but rely on indirect correlations. Literature ranges provide regional context but lack local specificity. However, the analysis done validated dynamic moduli predictions from log versus lab data. The similarities between the different datasets with relatively high correlation coefficients imply consistent physics between the lab and subsurface especially for Young's modulus, Bulk modulus and shear modulus. However, there were some differences in predicted properties like Poisson Ratio as seen in Figures 5.27, 5.28 and 5.29, that indicate factors like porosity discrepancies analysed in 5.22 affect this parameter more significantly for some moduli. Therefore, as an additional layer of data validation, we can assess the relationships between core-scale, well-scale, and basin-scale moduli estimations by overlaying results from all three sources for the same formations. This multifaceted view reduces uncertainties and biases associated with moduli predictions.

As a final layer of data validation, the measured and predicted elastic parameters from the samples and the logs will be plotted against a collected of basin-scale elastic parameter measurements retrieved from TNO. The basin-scale data are from acoustic log data gathered from the wells located all over the Netherlands by TNO, including the various elastic moduli of different formations. For the purpose of this study, the data points were focused on only sandstone data from two stratigraphic groups, the Upper Rotliegend and the Upper Germanic groups. It is important to note that these data are mostly from onshore wells and correspond to the West Netherlands basin. Figure 6.2 below displays the three sets of data; TNO as the biggest scale, Log data as the middle scale and the data sample representing the small scale.

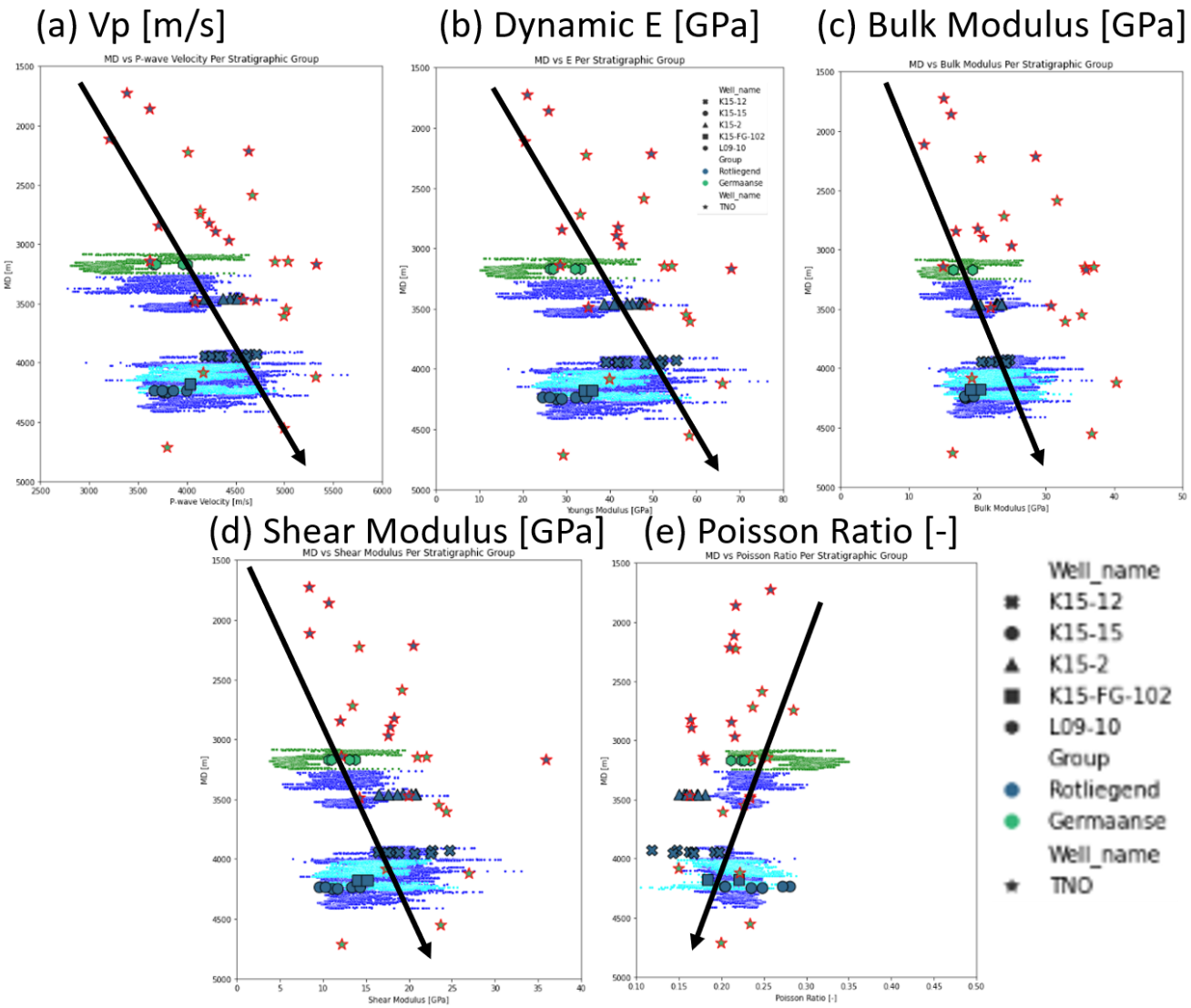

Figure 6.2: Measured Depth [m] vs various elastic parameters of the sandstone reservoirs in Upper Rotliegend (blue) and Upper Germanic (green) groups for all datasets. TNO Data are in red stars, Lab-derived data are the symbols framed in black, and the dots are predicted from logs (using velocity relation from K12-17)

The trends observed from the TNO data of all the elastic parameters are consistent with both predicted logs and the lab-derived data. However, a few scattered data points fall outside the expected range at certain depths. This could be due to the fact that the TNO data are mostly from onshore well logs, or they could be different sandstone members within the formations/groups or due to the wide range of heterogeneity in the upper Rotligened sands and the Upper Germanic sands that could be not entirely covered by our log data or samples data. In analyzing the lithology differences and modulus values per well, we compared our lab-measured data and log-predicted values to ensure they align with the trends found in the Netherlands subsurface and fall within a similar value range at the target depth interval. However, our analysis was broad due to the lack of rock properties data, such as porosity and density, in the TNO dataset, which made it challenging to examine the elastic moduli in greater detail. While my integrated study explored a limited dataset, lab measurements and moduli prediction results agree with the general patterns from the literature and basin data but show context-specific details highlighting the need for localized data. This is valuable for laying the foundation for building more comprehensive and representative geomechanical models needed for safe, sustainable CO2 storage in the Dutch North Sea reservoirs. Expanding the core sampling and testing that I initiated will further refine the characterized trends and the correlations obtained to lower the prediction uncertainties and provide the detailed inputs required for injection design and monitoring.

For the SHARP project, this work is important to provide key inputs on the geomechanical behaviour heterogene-

ity of the Slochteren and Solling formations that are being evaluated for offshore CO2 storage. The variability observed in these formations from the lab measurements, measured logs, and predicted logs, particularly in wave velocities and elastic moduli, highlights the complexity of the subsurface geology. The extracted correlations offer initial predictive capabilities relating petrophysical properties to geomechanical parameters, which enables property estimations between wells using log data. While the findings are limited, this workflow creates a template for expanding lab measurements and log analysis to reduce uncertainties. Also, it emphasizes the importance of building highly detailed geomechanical models for a well-rounded case study done for this project.

Characterizing geomechanical properties and reflecting their variability in geological models is essential in CO2 storage projects to optimize injectivity, avoid fault activation, monitor the CO2 plume and ensure caprock integrity. The obtained static and static and dynamic moduli ranges, wave velocities, parameter correlations, and their sensitivity to factors such as porosity all help in the decision-making process to find suitable injection sites. These data ranges and correlations are used to estimate the spatial variations in properties away from the core data and ultimately build a geomechanical model. For example, the Poisson's ratio value assists in indicating potential borehole breakouts; the Shear modulus relates to formation stability. Overall, these measurements and initial predictions obtained contribute to advancing the geomechanical understanding needed for secure and effective carbon storage.

7 Conclusion and Recommendations

There is an increasing interest in the geomechanical characterization of the offshore Dutch subsurface for carbon dioxide storage site assessments. This thesis aimed to characterize the geomechanical behaviour of sandstone reservoirs in the Dutch North Sea through experimental and well-log analysis. The main research question in the study is whether the geomechanical properties are affected by the heterogeneity of the subsurface or not. From the experimental results, it was apparent that the static and dynamic properties are clearly impacted by the heterogeneity of the rock properties, especially in terms of porosity and density. This means that the heterogeneity observed highlights that localized measurements and building a model that honours these variabilities is required to capture the complexity influencing the elastic behaviour across the reservoir.

1. The triaxial compression tests with acoustic measurements results exhibited significant variability in static, dynamic elastic moduli and wave velocities between the samples that are linked to differences in two main rock parameters; porosity and density. Velocities, Static and dynamic Young's moduli, shear and bulk moduli decrease with the increase of porosity and increase with the increase of density. While the Poisson's ratio and the velocity ratio (Vp/Vs) increase with the increase of porosity and the decrease of density.

2. There is a clear correlation between the increase in velocities with the increase in confining pressure, where it is steep in low pressures and gets gradual in higher pressure values. This same correlation is clearly visible in the Young's and Shear moduli, but the correlation is not very clear in the Bulk modulus. Lastly, it is the opposite for Poisson's and velocity ratios as both parameters have a clear trend of decreasing with the increase of confining pressure.

3. Relations extracted from lab data showed moduli dependency on porosity and confining pressure. Therefore an empirical equation combining these two factors from lab data was extracted to simulate the variation of stress with depth with a link to porosity.

4. A relation between dynamic and static Young's moduli was established with a high correlation coefficient value. Comparisons to the literature show the slope in our data is lower, indicating the potential sensitivity linked to microcracks.

The second purpose of this thesis is to compare lab-measured data and lab-derived elastic moduli to log-derived elastic moduli in order to evaluate the feasibility of data prediction. A workflow was created and implemented to predict the elastic moduli logs for the purpose of lowering the uncertainties associated with the absence of direct measurements of Shear velocity in our wells. The results showed that using this workflow decreased the predictions' uncertainties, and the correlations used are feasible as a first pass in the initial geomechanical data analysis of the target wells and formations.

1. The Shear wave velocity predictions compared three types of Vp-Vs relation; from the lab measurements, nearby wells and standard empirical relations. The nearby well correlations gave the best match to core lab results.

2. The predicted elastic moduli logs generally agreed with core data lab results validating the physics, but there have been some discrepancies in properties like Poisson's ratio observed. This could be due to the discrepancies between Neutron porosity logs and Pycnometer porosity measurements, as some properties are more sensitive to these than others.

3. The predictions for the Slochteren formation were better than the Solling formation, which relates to the limitations of data availability of the Solling formation in lab experiments and log data which caused a biased in the results towards the Slochteren formation since the lithology of both formations is different.

While valuable insights were gained, the study was limited by the small number of core samples tested from a few wells. To build on this work and reduce uncertainties, I recommend the following steps:

1. In terms of the lab experiments conducted at TU Delft. Ensure that the experiments are conducted with the same test setup and sample dimensions to obtain comparable data and reduce uncertainty.

2. Perform tests that go beyond the elastic zone; plastic zone and failure to obtain as much information as possible to analyse beyond the elastic behaviour of the rocks for a more comprehensive geomechanical analysis.

3. Expand the number of samples and the core sampling of more wells to cover a wider area and diversity of lithologies, depositional facies and porosities. This will better capture the inherent heterogeneity of the reservoirs. Also, testing more samples will refine the correlations found between elastic moduli, acoustic velocities, confining pressure and petrophysical properties like porosity and density.

4. Measure the permeability of the samples because it provides valuable insight into their properties and the path taken by the injected fluid.

5. For the purpose of expanding the study, increase the number of logs from nearby well to be incorporated in the S-wave velocity prediction for a refined correlation. Also, ensure that these nearby wells have logs beyond P-sonic and S-sonic for a better lithology analysis where correlation with other parameters like porosity and density can refine the equations extracted to predict the S-wave velocity.

6. Incorporate shear wave sonic logging in future wells drilled in the target formations. The current findings can work as a first pass for initial analysis, and direct S-wave velocity measurements are critical for calculating more accurate geomechanical properties that reflect the local lithology. More S-wave data will reduce the uncertainty in estimated logs using correlations.

8 Bibliography

Abbink, Oscar, J. Colloman, James Riding, P. Williams, and A. Wolfard. 2001. Biostratigraphy of Jurassic-Cretaceous boundary strata in the Terschelling Basin, The Netherlands. Proceedings of The Yorkshire Geological Society - PROC YORKS GEOL SOC 53: 275-302. doi:10.1144/pygs.53.4.275.

Archer, S, and V Rasouli. 2012. A log based analysis to estimate mechanical properties. Journal of Petroleum and Mineral Resources 21:163–170.

Asef, Mohammad, and Ali Reza Najibi. 2013. The effect of confining pressure on elastic wave velocities and dynamic to static Young's modulus ratio. Geophysics 78: 135-D142. doi:10.1190/geo2012-0279.1.

Brocher, T.M. 2005. Empirical relations between elastic wavespeeds and density in the Earth's crust. Bulletin of the Seismological Society of America 95 (6): 2081-2092.

Brinson, H, and C Brinson. 2008. Stress and strain analysis measurement polymer engineering science and viscoelasticity: an introduction. Springer, New York.

Castagna, J.P., M.L. Batzle, and R.L. Eastwood. 1985. Relationships between compressional-wave and shear-wave velocities in clastic silicate rocks. Geophysics 50 (4): 571-581.

Chang, Chandong & Zoback, Mark & Khaksar, Abbas. (2006). Empirical relations between rock strength and physical properties in sedimentary rocks. Journal of Petroleum Science and Engineering. 51. 223-237. 10.1016/j.petrol.2006.01.003.

Christensen, N.I., and W.D. Mooney. 1995. Seismic velocity structure and composition of the continental crust: A global view. Journal of Geophysical Research 100 (B6): 9761–9788.

Dutta, N.C., R. Knapp, G. Brown, and D. Zhang. 2007. Efficient techniques for S-wave velocity prediction. In SEG Technical Program Expanded Abstracts, 2693-2697. Society of Exploration Geophysicists.

Eissa, E.A., and A. Kazi. 1988. Relation between static and dynamic Young's moduli of rocks. International Journal of Rock Mechanics and Mining Sciences & Geomechanics Abstracts 25 (6): 479-482. doi:10.1016/0148-9062(88)90987-4.

Færseth, R.B. 1996. Interaction of Permo-Triassic and Jurassic extensional fault-blocks during the development of the northern North Sea. Journal of the Geological Society 153 (6): 931-944.

Gaupp, R., and J.A. Okkerman. 2012. Diagenesis And Reservoir Quality Of Rotliegend Sandstones In The Northern Netherlands—A Review. SEPM (Society for Sedimentary Geology). doi:10.2110/sepmsp.076.193.

Geluk, M.C. 2007. Permian. Geology of the Netherlands, 61-83.

Glennie, K.W., and J.R. Underhill. 2009. Origin, development and evolution of structural styles. In United Kingdom Oil and Gas Fields, Vol. 20, edited by J.G. Gluyas and H.M. Hichens, Geological Society.

Global CCS Institute. 2019. Global Status of CCS Report 2019. https://www.globalccsinstitute.com/resources/publications-reports-research/global-status-of-ccs-report-2019/

Han, D., A. Nur, and D. Morgan. 1986. Effects of porosity and clay content on wave velocities in sandstones. Geophysics 51 (11): 2093-2107.

Hunfeld, L.B., J.P.T. Foeken, and B.M.M. Van Kempen. 2021. Geomechanical parameters derived from compressional and shear sonic logs for main geothermal targets in The Netherlands. Tech. rep. www.nlog.nl.

IEA. 2021. Carbon capture, utilization and storage. https://www.iea.org/reports/ccus-in-clean-energy-transitions/carbon-capture-utilisation-and-storage.

IPCC. 2014. Climate change 2014: mitigation of climate change. Cambridge University Press.

Jizba, D.L. 1992. Mechanical and acoustical properties of sandstones and shales. PhD diss., Stanford University.

Krief, M., J. Garat, J. Stellingwerff, and J. Ventre. 1990. A petrophysical interpretation using the velocities of P and S waves (full waveform sonic). The Log Analyst 31 (06).

Lauwerier, W. 2021. Resource evaluation of the Dutch offshore Rotliegend play. Master's thesis, Utrecht University.

Mavko, G., T. Mukerji, and J. Dvorkin. 2020. The rock physics handbook. Cambridge University Press.

McCann, D.M., and D.C. Entwisle. 1992. Determination of Young's modulus of the rock mass from geophysical well logs.

Morris, J.P. et al. 2011. A systematic method for estimating probable maximum loss from CO2 storage sites. International Journal of Greenhouse Gas Control 5 (4): 879-887.

Nielsen, S.B. et al. 2005. The evolution of western Scandinavian topography: a review of Neogene uplift versus the ICE (isostasy–climate–erosion) hypothesis. Journal of Geodynamics 39 (3): 265-275.

Prasad, M., and K. Kuzmina. 2021. Machine learning for S-wave velocity prediction. The Leading Edge 40 (8): 558-564.

Ritchie, H., and M. Roser. 2020. Co2 and greenhouse gas emissions. https://ourworldindata.org/co2-and-other-greenhouse-gas-emissions.

Rutqvist, J. et al. 2010. Coupled reservoir-geomechanical analysis of CO2 injection at In Salah, Algeria. Energy Procedia 4: 3227-3234.

Sharma, A., and A.N. Tutuncu. 2016. Grain contact models for attenuating seismic wave velocity in granular rocks. Journal of Geophysical Research: Solid Earth 121 (12): 8706–8729.

Shi, J., C. Sinayuc, S. Durucan, and A. Korre. 2013. Assessment of carbon dioxide plume behaviour within the storage reservoir and the lower caprock around the KB-502 injection well at In Salah. International Journal of Greenhouse Gas Control 16: S85-S93.

Skurtveit, Elin, and Lars Grande. 2022. SHARP Storage.

Stress history and reservoir pressure for improved quantification of CO2 storage containment risks (SHARP Storage), project proposal.

TNO-AGE, Appendix B: summary data sheet. n.d. https://www.nlog.nl/en/geomechanical-data.

Tran, David, Settari, Antonin, and Long Nghiem. "New Iterative Coupling between a Reservoir Simulator and a Geomechanics Module." Paper presented at the SPE/ISRM Rock Mechanics Conference, Irving, Texas, October 2002. doi: https://doi-org.tudelft.idm.oclc.org/10.2118/78192-MS

Van der Kooij, C.I. 2016. Triassic reservoir development in the northern Dutch offshore. Internship report.

Verdon, J.P. et al. 2013. Monitoring of carbon dioxide storage using interferometric synthetic aperture radar: A case study from the Krechba field, Algeria. Journal of Geophysical Research: Solid Earth 118 (9): 4795-4810.

Wang, L., E. Rybacki, A. Bonnelye, et al. 2021. Experimental Investigation on Static and Dynamic Bulk Moduli of Dry and Fluid-Saturated Porous Sandstones. Rock Mechanics and Rock Engineering 54: 129–148.

Ziegler, P.A. 1992. North Sea rift system. Tectonophysics 208 (1-3): 55-75.

Zoback, M.D., and S.M. Gorelick. 2012. Earthquake triggering and large-scale geologic storage of carbon dioxide. Proceedings of the National Academy of Sciences 109 (26): 10164-10168.

9 List of figures and tables

List of Figures

List of Tables

Appendices

A Dynamic and Elastic Data values

					50 MPa Pc Cycle						
Sample_name	Pycnometer Porosity	Density [g/cm3]	Gamma Ray [gAPI]	Static E [GPa]	Vp [m/s]	Vs [m/s]	Vp/Vs	Dynamic E [Gpa]	Bulk Modulus [GPa]	Poisson Ratio	Shear Modulus [GPa]
K15-12-1V	0.085	2.568	28.45	20.39	4718.32	3103.95	1.52	55.36	24.19	0.12	24.75
K15-12-21V	0.091	2.550	32.35	18.96	4608.48	2973.20	1.55	51.55	24.10	0.14	22.54
K15-2-3V	0.106	2.474	28.24	20.81	4519.97	2898.72	1.56	47.83	22.82	0.15	20.79
K15-2-4V	0.113	2.467	31.64	24.50	4564.56	2906.20	1.57	48.31	23.62	0.16	20.84
K15-2-5V	0.115	2.508	29.94	21.17	4520.37	2876.79	1.57	48.14	23.58	0.16	20.76
K15-2-7V	0.115	2.508	48.49	18.43	4186.08	2651.22	1.58	41.08	20.45	0.16	17.63
K15-12-14V	0.135	2.480	38.27	18.42	4362.33	2758.54	1.58	44.04	22.03	0.17	18.87
K15-12-12V	0.142	2.462	39.97	18.20	4256.25	2701.86	1.58	41.79	20.64	0.16	17.97
K15-FG-102-4V	0.173	2.408	29.05	13.81	4032.93	2507.99	1.61	35.88	18.98	0.18	15.15
K15-15-6V	0.190	2.412	18.53	15.30	4000.87	2437.82	1.64	34.54	19.50	0.20	14.33
L09-10-5VB	0.193	2.345	33.93	13.22	4009.42	2425.22	1.65	33.42	19.31	0.21	13.79
L09-10-6VA	0.217	2.300	34.62	12.11	3684.71	2189.49	1.68	27.07	16.53	0.23	11.03
K15-15-13V	0.225	2.344	20.53	11.86	3803.63	2238.02	1.70	29.00	18.26	0.24	11.74
K15-15-4V	0.231	2.341	21.22	9.97	3750.65	2098.29	1.79	26.23	19.19	0.27	10.31
					30 MPa Pc Cycle						
Sample_name	Pycnometer Porosity	Density [g/cm3]	Gamma Ray [gAPI]	Static E [GPa]	Vp [m/s]	Vs [m/s]	Vp/Vs	Dynamic E [Gpa]	Bulk Modulus [GPa]	Poisson Ratio	Shear Modulus [GPa]
K15-12-1V	0.085	2.568	28.45	20.39	4629.41	2974.96	1.56	52.20	24.74	0.15	22.73
K15-12-21V	0.091	2.550	32.35	18.96	4506.43	2847.24	1.58	48.28	24.22	0.17	20.67
K15-2-3V	0.106	2.474	28.24	20.81	4487.62	2863.62	1.57	46.92	22.77	0.16	20.28
K15-2-4V	0.113	2.467	31.64	24.50	4444.47	2797.76	1.59	45.27	22.99	0.17	19.31
K15-2-5V	0.115	2.508	29.94	21.17	4373.03	2728.21	1.60	44.11	23.07	0.18	18.67
K15-2-7V	0.115	2.508	48.49	18.43	4082.40	2567.05	1.59	38.78	19.77	0.17	16.53
K15-12-14V	0.135	2.480	38.27	18.42	4330.23	2658.17	1.63	41.97	23.14	0.20	17.52
K15-12-12V	0.142	2.462	39.97	18.20	4186.58	2584.20	1.62	39.20	21.23	0.19	16.44
K15-FG-102-4V	0.173	2.408	29.05	13.81	4030.34	2412.25	1.67	34.22	20.44	0.22	14.01
K15-15-6V	0.190	2.412	18.53	15.30	3864.05	2355.20	1.64	32.23	18.18	0.20	13.38
L09-10-5VB	0.193	2.345	33.93	13.22	3962.38	2364.23	1.68	32.08	19.34	0.22	13.11
L09-10-6VA	0.217	2.300	34.62	12.11	3654.89	2153.08	1.70	26.33	16.51	0.23	10.66
K15-15-13V	0.225	2.344	20.53	11.86	3765.11	2178.45	1.73	27.77	18.39	0.25	11.12
K15-15-4V	0.231	2.341	21.22	9.97	3671.49	2026.80	1.81	24.64	18.74	0.28	9.62

Figure A.1: Mechanical and Acoustic Data results from 30,50 MPa Cycles

B Histogarms of rock parameters from log data

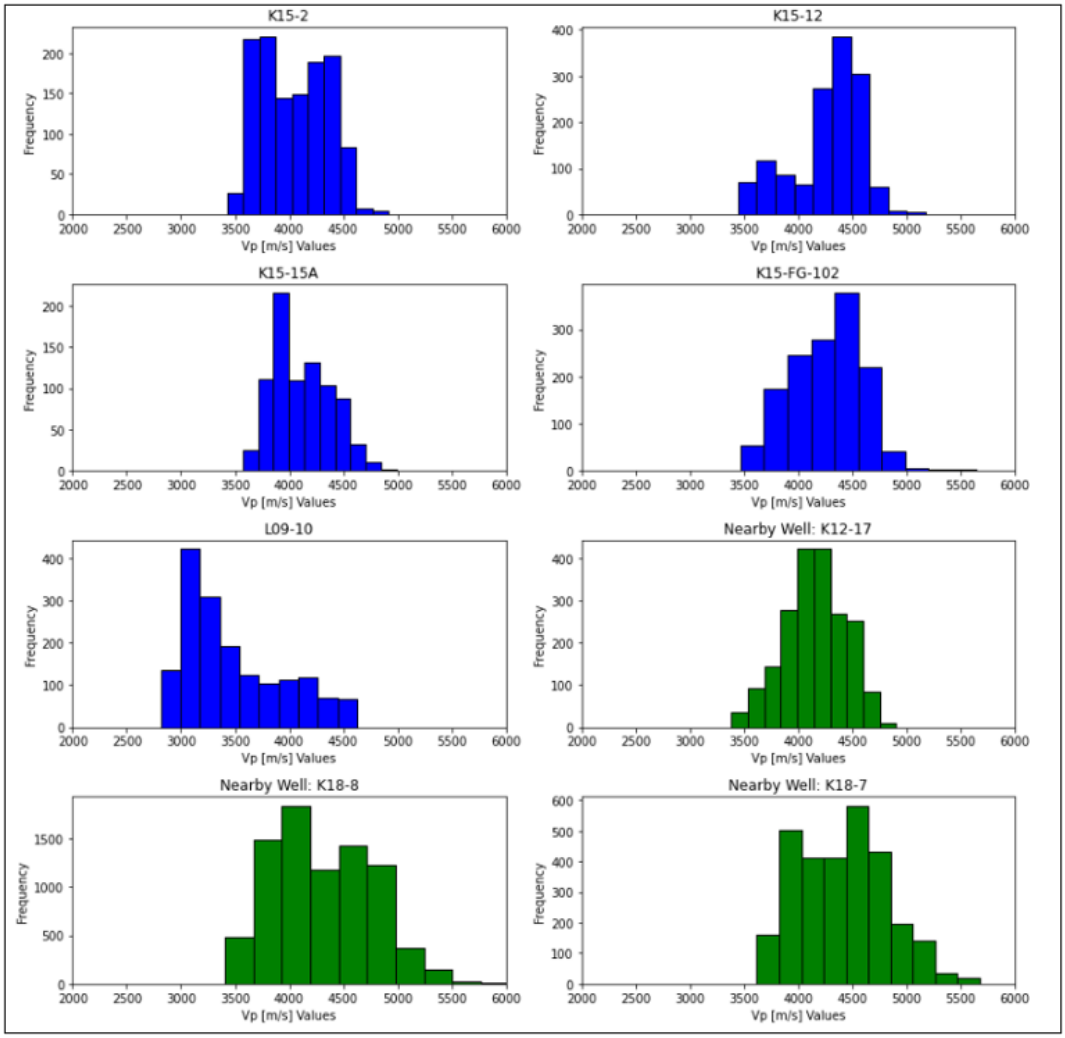

Figure B.1: Vp [m/s]

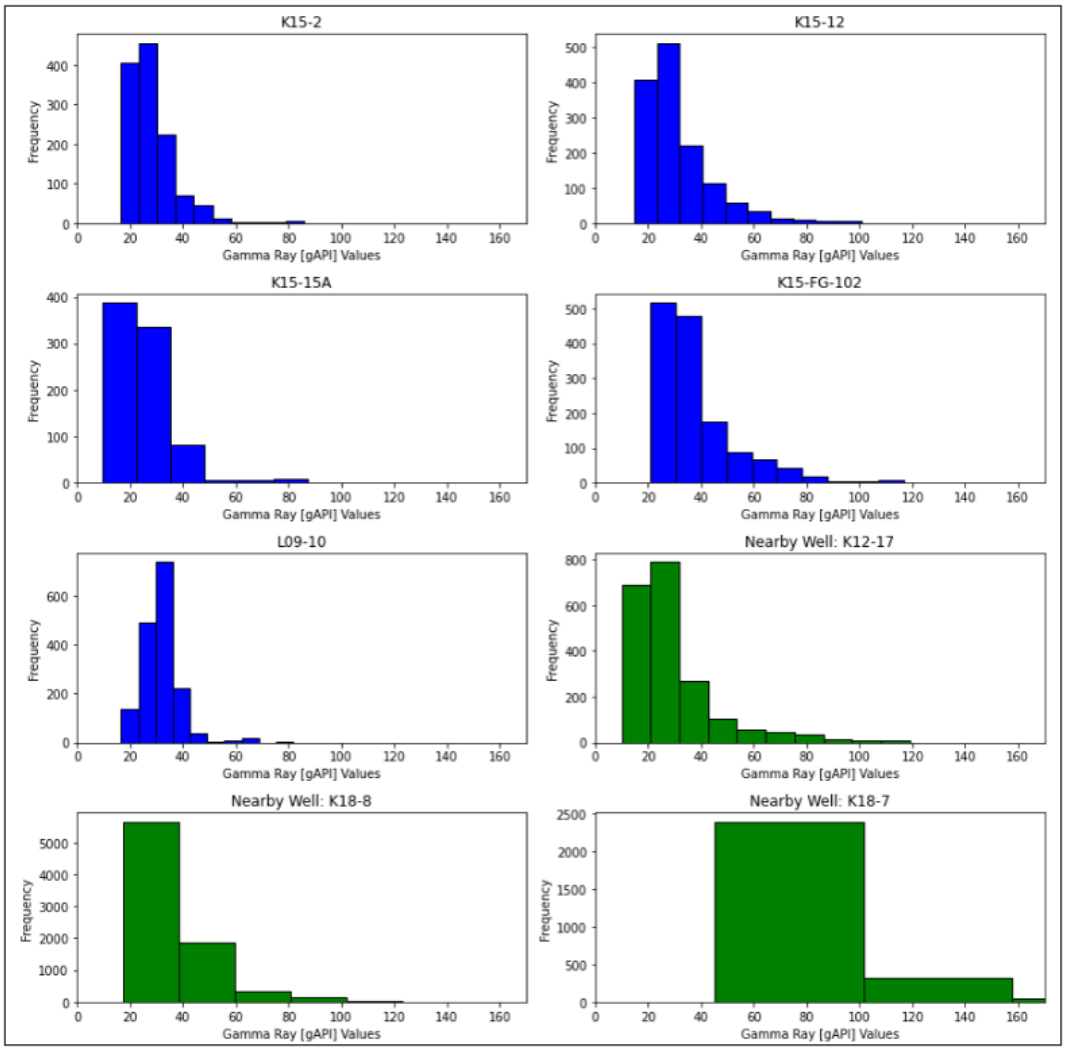

Figure B.2: GR [gAPI]

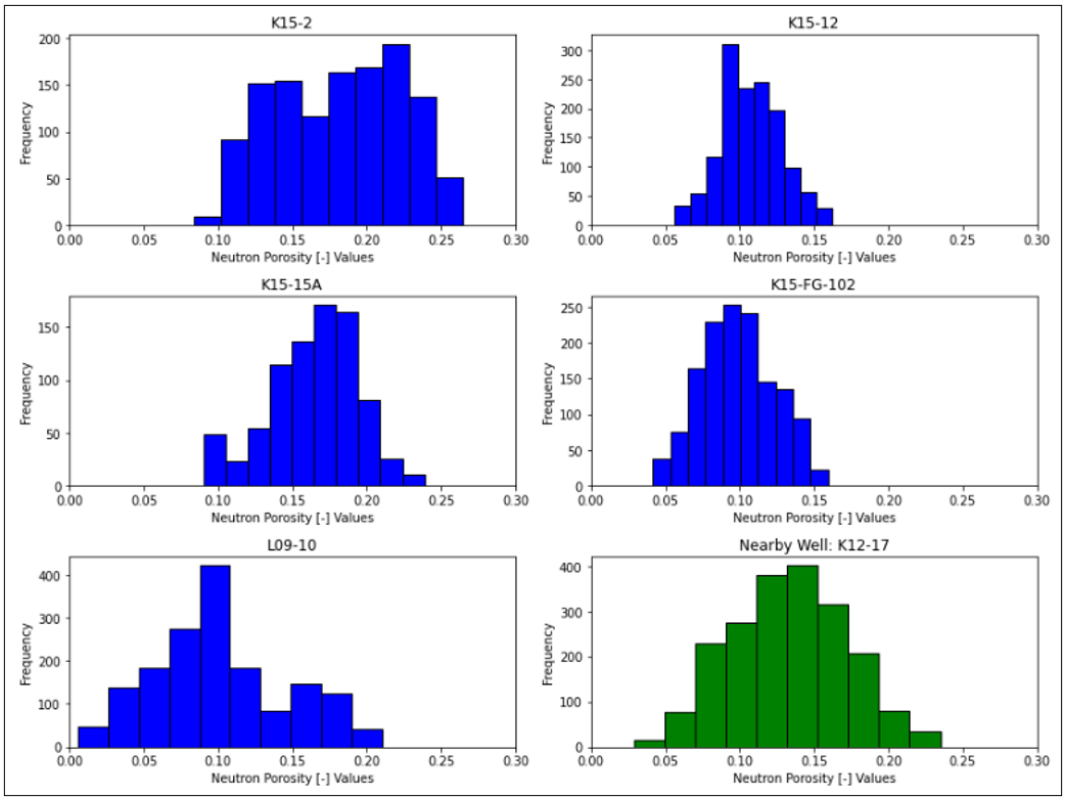

Figure B.3: Neutron Porosity [-]

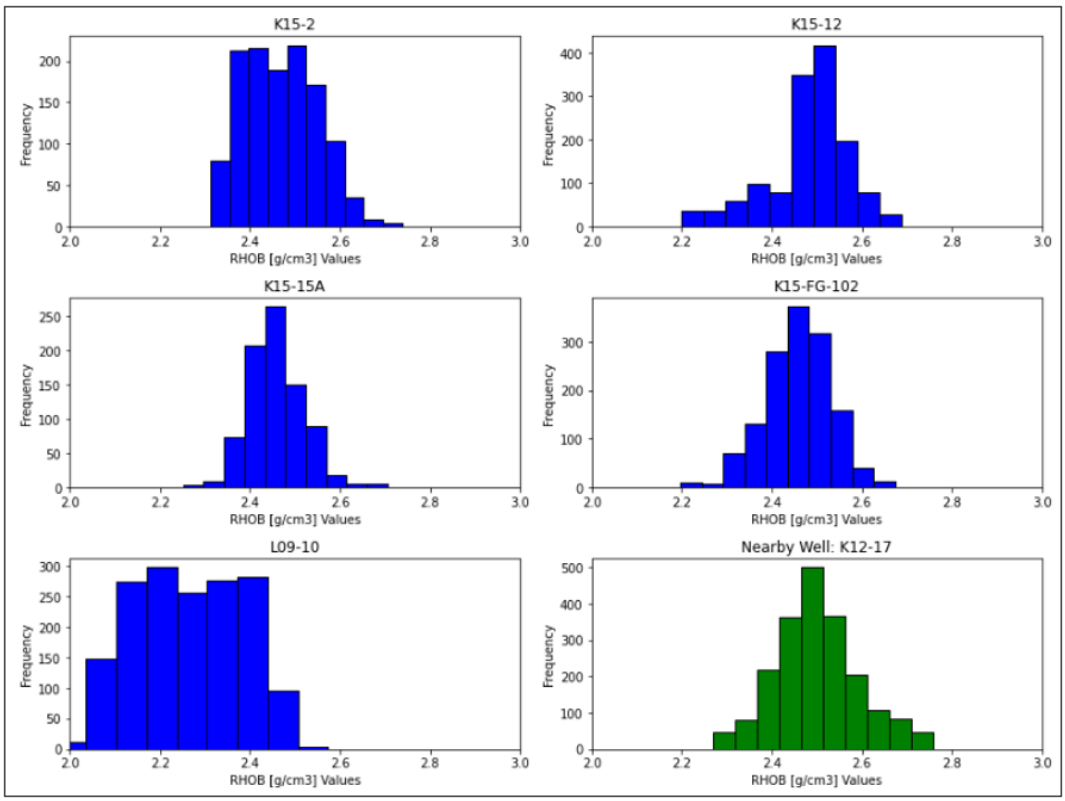

Figure B.4: RHOB [g/cm3]

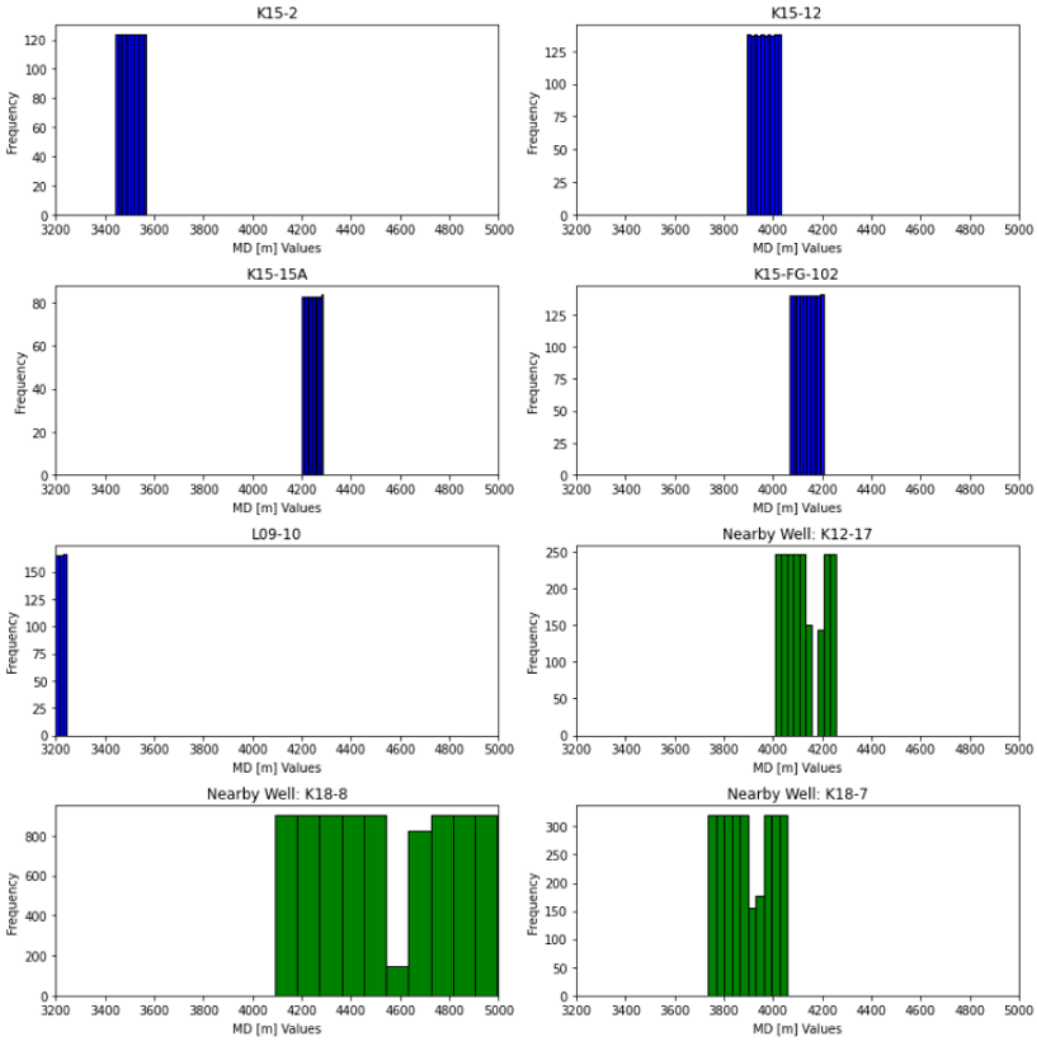

Figure B.5: Measured Depth [m]

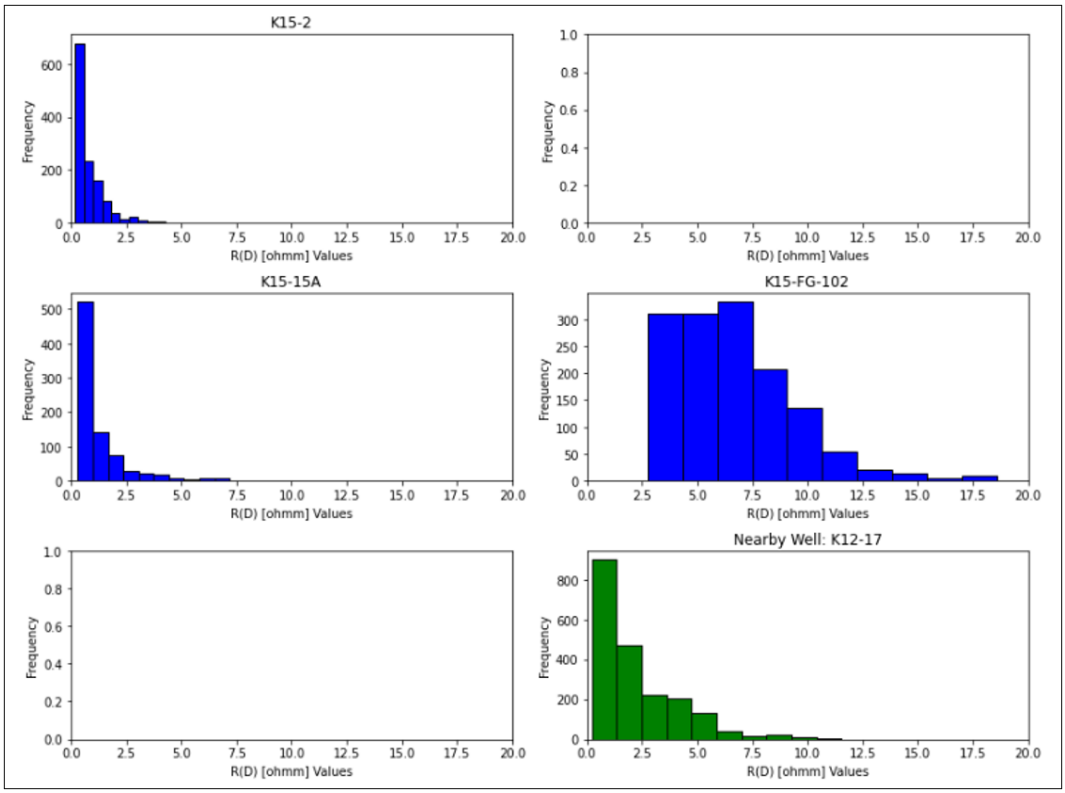

Figure B.6: Deep Resistivity [ohmm]

C Gamma Ray and Resistivity logs vs. P-wave velocity logs

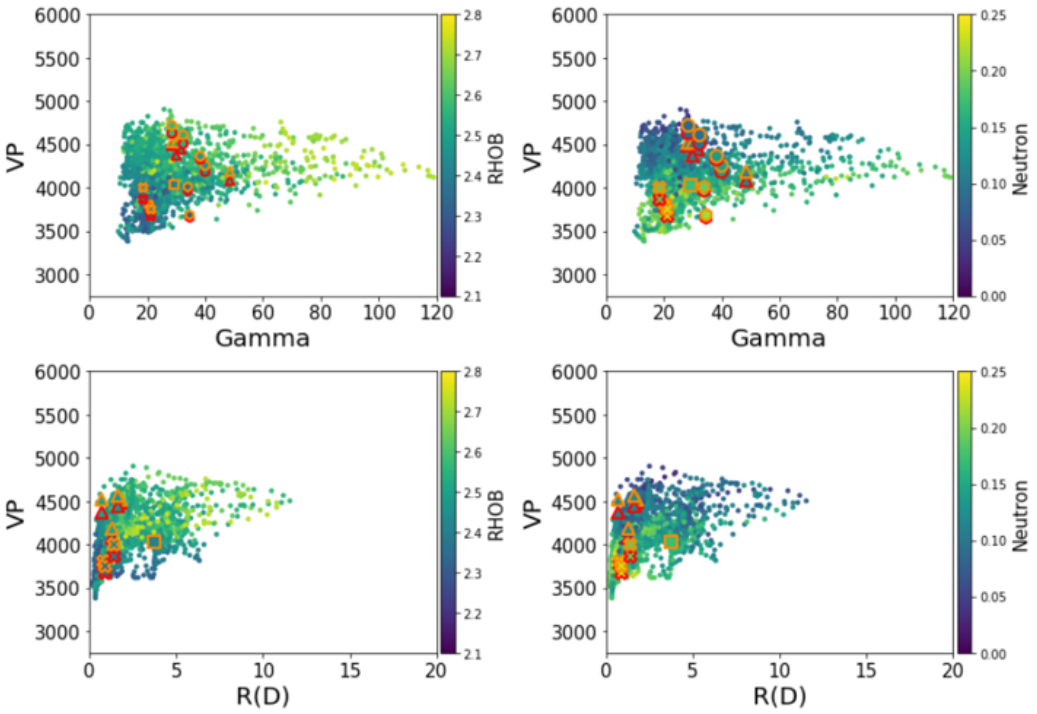

Figure C.1: Logs of Gamma-ray and resistivity against P-wave velocity, showing unclear trend between the rock parameters

D Standard Logs of Nearby Wells and Project Wells (AOI) with Trendlines

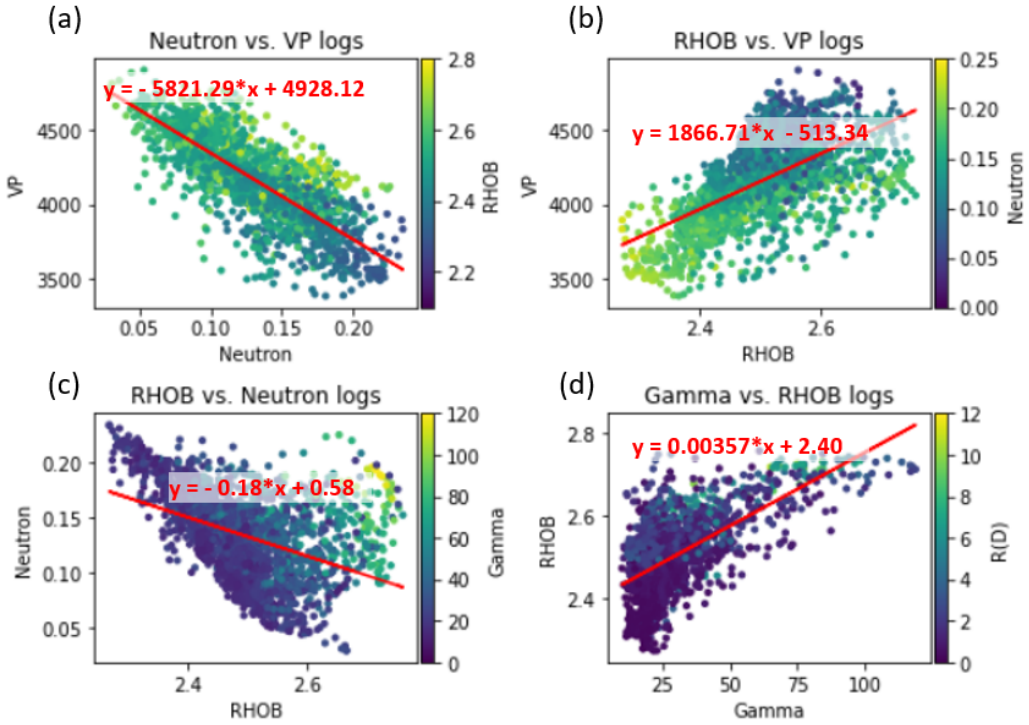

Figure D.1: Nearby wells standard logs with trendline

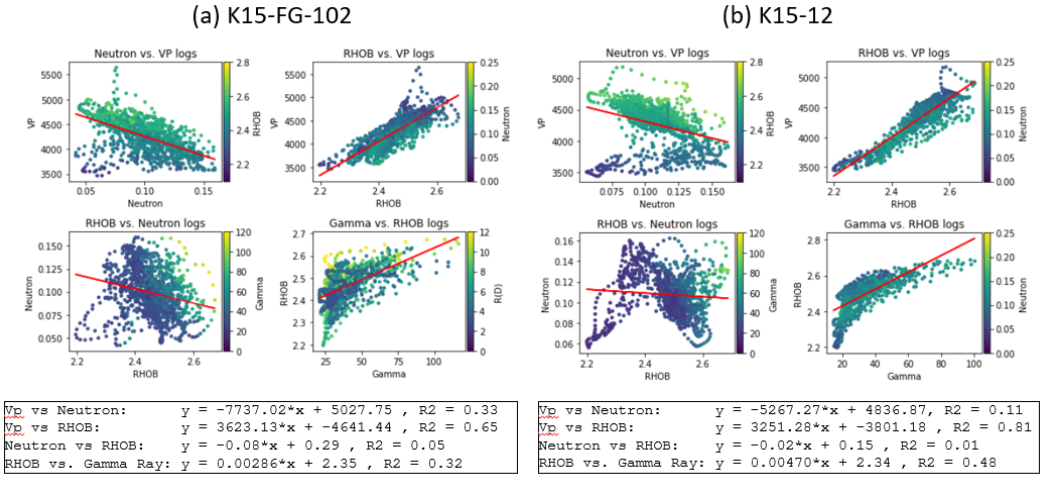

Figure D.2: AOI wells standard logs with trendline (part 1/3)

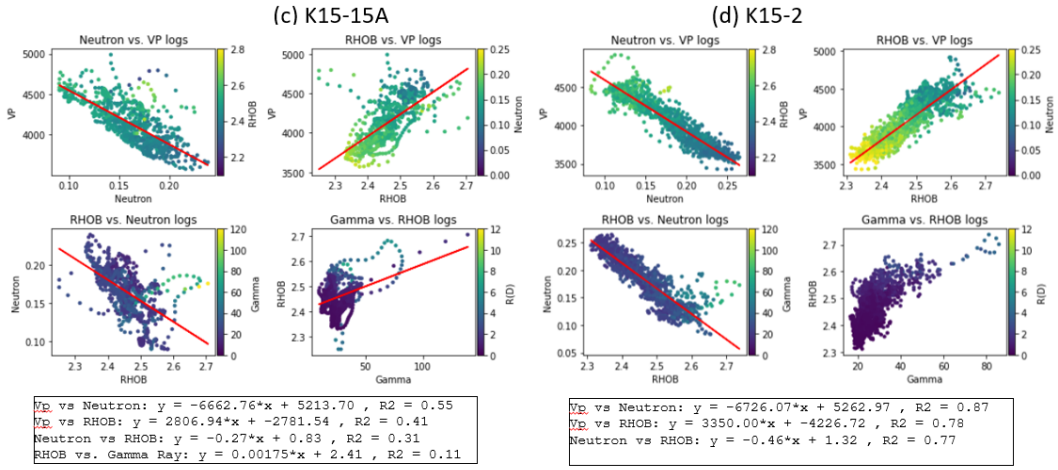

Figure D.3: AOI wells standard logs with trendline (part 2/3)

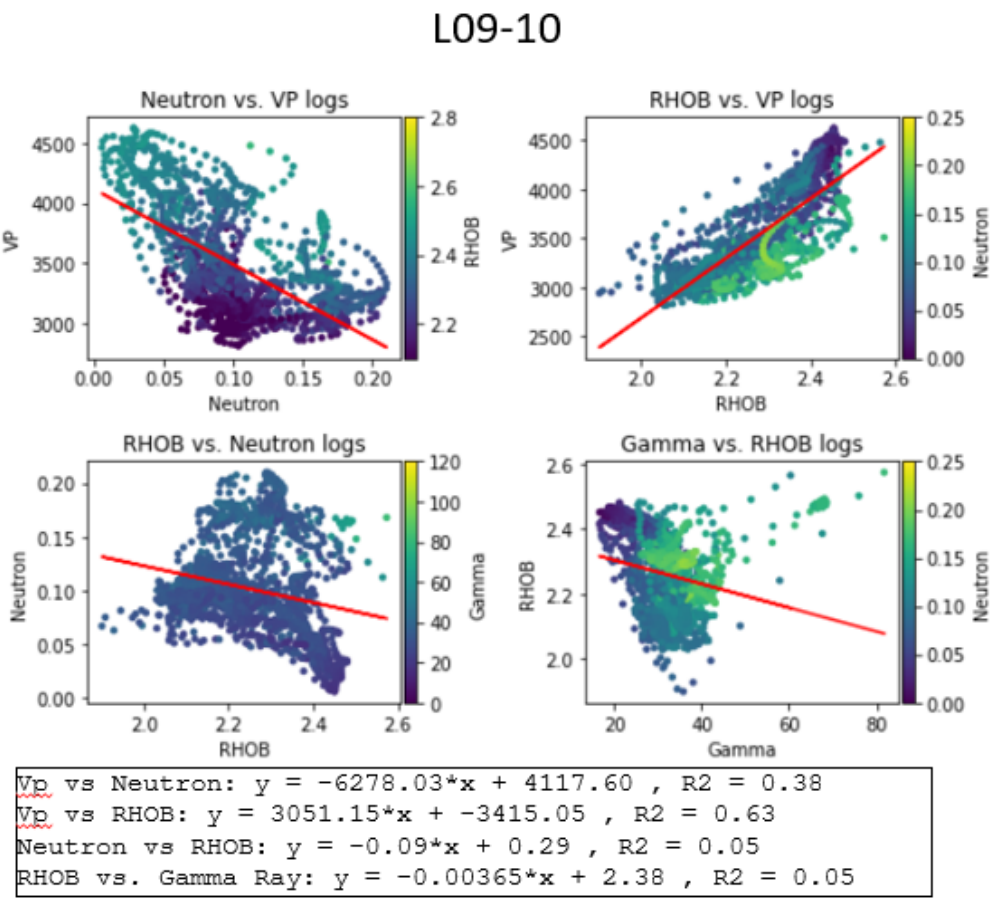

Figure D.4: AOI wells standard logs with trendline (part 3/3)

E Elastic Moduli Log Predictions

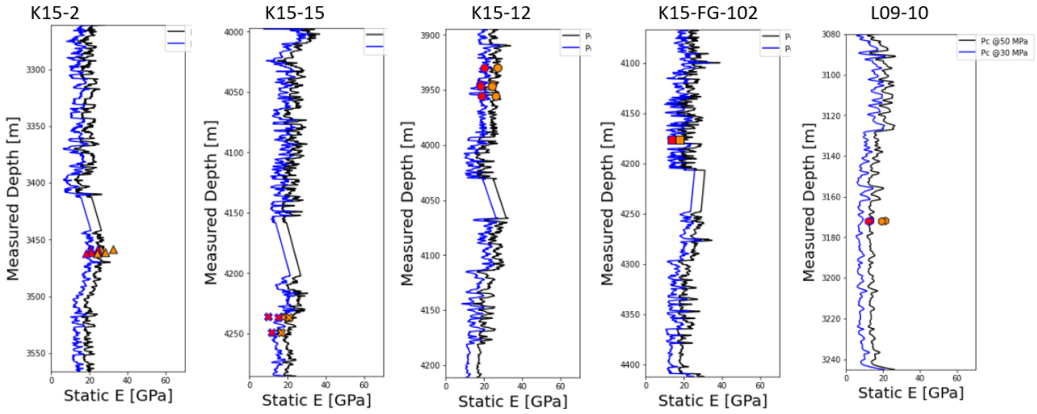

Figure E.1: Predicted Log of Static Young's modulus of 30 and 50 [MPa] Pc cycles

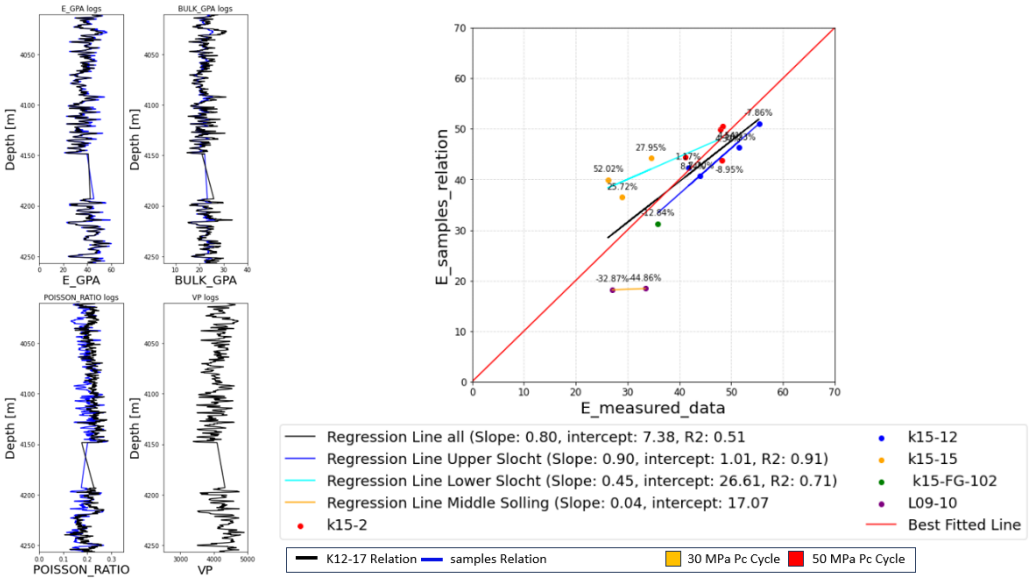

Figure E.2: Predicted Log elastic moduli using K12-17 as a blind test